LED-TO-LED COMMUNICATION: A BIDIRECTIONAL LOW-COMPLEXITY SYSTEM BASED ON RGB LEDS AS RECEIVER

MARIAM M. A. GALAL

PhD

2020

LED-TO-LED COMMUNICATION: A BIDIRECTIONAL LOW-COMPLEXITY SYSTEM BASED ON RGB LEDS AS RECEIVER

MARIAM M. A. GALAL

A thesis submitted in partial fulfilment of the requirements of the University of Northumbria Newcastle for the degree of

Doctor of Philosophy

Research undertaken in the Faculty of Engineering and Environment

September 2020

Abstract

This thesis studies, designs and characterises a low-complexity bidirectional LED-to-LED communication system employing only off-the-shelf tricolour light emitting diodes (LEDs) as transmitters and receivers with the aim of providing the required connectivity for contemporary small Internet-of-things (IoT) devices. In today's interconnected world of Internet of Things devices, it is imperative to have low-complexity and small size communication modules to enable seamless communication between such small devices over short distances and with low data rates without exhausting the already over-crowded radio frequency spectrum. While a regular visible light communication (VLC) system containing an LED and a photodiode is a viable option, it provides only one-directional communication. To enable an uplink, a repetition of the downlink is usually provided, doubling the cost, complexity and space of the original circuits. Hence, an LED-to-LED solution maximises the benefit of VLC and imitates the idea of having one antenna for transmitting and receiving, known in radio frequency (RF) technologies.

In order to design an LED-to-LED system, the LED is characterised as transmitter and receiver both qualitatively and empirically. The results confirmed the feasibility of the LED as a wavelength-selective and directional photodetector with a field of view of 18° and low responsivity of 0.2 mA/W under zero bias. Interestingly, the experiments also reveal that the LED could even detect light when slightly forward biased. Based on the identified characteristics of the LED, a current-mirror-based LED driver, a transimpedance amplifier and an analogue switch are designed and separately evaluated to mitigate the low responsivity of the LED as photodetector. The VLC channel is also characterised and the interference due to the most common contemporary ambient light sources is evaluated. The interference of each light source is mathematically modelled based on the empirical results. The overall LED-to-LED link is practically implemented and optimised to reach data rates up to 200 kbps at distances up to 7 cm with the help of an optimised matched filter at the detection phase. The analogue switch completes the system by providing the option of a bidirectional half-duplex channel while avoiding flickering. At a switching frequency of up to 300 Hz, the LED-to-LED system could deliver error-free data transmission at speeds up to 100 kbps in a back-to-back configuration.

The findings of this thesis indicate that a bidirectional low-complexity VLC system depending only on RGB LED for transmission and photodetection is not only feasible, but also a very viable option for short-range, low-speed communication between small IoT devices with high potential of commercial deployment.

Acknowledgement

I would like to first acknowledge the Arab Academy of Science, Technology and Maritime Transport – Alexandria, Egypt for partially funding the work presented in this thesis. I would also like to acknowledge Barco Control Rooms GmbH – Karlsruhe, Germany for providing me a one-year internship as research and development engineer in their innovation centre and giving me access to their laboratory and materials to continue the required practical experiments for this study upon moving to Germany.

I would like to thank my supervisors, Dr. Wai Pang Ng, Dr. Richard Binns and Prof. Ahmed Abd El Aziz, who have advised and supported me throughout this study. Your insightful feedback and advice brought my work to a higher level and taught me a lot. This work was only possible thanks to your supervision efforts.

I would like to thank my colleagues at the Arab Academy, with whom I shared many memories and who supported me emotionally and professionally during this work. Special thanks for Prof. Heba Shaban and Eng. Sara Ibrahim for always being there for me and supporting me throughout this work. I would also like to thank my colleagues at Barco Control Rooms GmbH for introducing me to the world of research in industry and for their encouragement and support. A special thanks goes to Marcos Otero Gensheimer, my team leader at Barco, for trusting me with leading a development and innovation project and giving me the opportunity to apply my acquired knowledge in this study onto a real-life consumer project.

The practical work in this project has been undertaken in three different countries, on two continents and in four different laboratories (including a portable setup at home). Almost all the implemented circuits and electronic equipment used in this thesis have passed at least one international border snuggled tightly in luggage. Looking back at this journey, I do not know how I would have reached this point without the unlimited support, love, patience, help and encouragement from my husband Hazem and our daughter Laila, who was mere weeks old when I started the PhD program. Thank you, Laila, for keeping up with mummy's busy schedule all your life. I am sure your hands-on knowledge about LEDs and electronic components that you acquired by watching me work would come in handy. Today your countdown has finally come to an end and I hope I made you proud!

No words would be enough to express my gratitude and thanks to my parents for their infinite love and support to me all their lives and for sacrificing everything for my wellbeing and success. Thank you, mum and dad!

Dedication

To my daughter Laila…

May my achievements inspire you to dream big, set high goals and trust in yourself to achieve them. If I could do it, you can too!

Declaration

I declare that the work contained in this thesis has not been submitted for any other award and that it is all my own work. I also confirm that this work fully acknowledges opinions, ideas and contributions from the work of others.

I declare that the word count of this thesis is 37055 words, excluding cover pages, table of contents, list of figures and abbreviations, abstract and references.

Name: Mariam Mohamed Ahmed Galal

Date: September 2020

Table of contents

List of Figures

List of Tables

Glossary of Abbreviations

AC	Alternating current
APD	Avalanche photodiode
AWGN	Additive white Gaussian noise
BER	Bit error rate
BJT	Bipolar junction transistor
BOM	Bill of materials
CB	Conduction band
DC	Direct current
eV	Electron Volt
EU	European Union
FFT	Fast Fourier transform
FWHM	Full width half maximum
GaAs	Gallium-Arsenide
GBW	Gain-bandwidth product
Gbps	Gigabits per second
Ge	Germanium
IC	Integrated circuit
IM-DD	Intensity modulation / direct detection
IoT	Internet of Things
IR	Infrared
kbps	Kilobits per second
LED	Light emitting diode
Li-Fi	Light fidelity

LS	Living surfaces
Mbps	Megabits per second
NG	Noise gain
NRZ	Non-return to zero
OFDM	Orthogonal frequency division multiplexing
OOK	On-off-keying
OWC	Optical wireless communications
PDF	Probability density function
PRBS	Pseudo-random binary sequence
PSD	Power spectral density
RF	Radio frequency
Rx	Receiver
Si	Silicon
SNR	Signal to noise ratio
THz	Terahertz
TIA	Transimpedance amplifier
Tx	Transmitter
VB	Valence band
Vcc	Supply voltage
VLC	Visible light communication
Wi-Fi	Wireless fidelity

Glossary of Symbols

A	Physical area of photodetector
$A_e(\Psi)$	Effective area of photodetector
BW_{3dB}	3-dB bandwidth
BW_{BPF}	Bandwidth of optical bandpass filter
c	Velocity of light
C	Capacitance
C_F	Feedback capacitor
d	Distance between transmitter and receiver
e	Electron charge
E	Energy
E_g	Bandgap, energy gap
E_{photon}	Photon energy
E_s	Energy of bit signal
E_v	Valence band energy
$\mathrm{erfc}(.)$	Complementary error function
f	Frequency
$f_{\cdot}(t)$	Function varying in time
$f_{c_{LPF}}$	Low-pass filter cut-off frequency
f_{switch}	Switching frequency
f_z	Frequency of zero
F_n	Noise figure
$g(\Psi)$	Optical concentrator gain

g_m	Transconductance
h	Plank's constant
$H(f)$	Filter transfer function
$h(t)$	Filter / channel impulse response
H_{LOS}	Line-of-sight gain of VLC channel
$I(\Phi)$	Radiation intensity at any point in the room
$I(0)$	Maximum luminous intensity
I_B	Current flowing through transistor base
I_C	Current flowing through transistor collector
I_M	Photocurrent generated by APD
I_{mirror}	Mirror current
$\langle i_{\mathrm{ph}} \rangle$	Average photocurrent
I_{ph}	Photocurrent
I_{ref}	Reference current
I_S	Reverse saturation current of the transistor
I_{sun}	Irradiance of the sun
k	Boltzmann's constant
l	Length of semiconductor sample
M	Current amplification factor of APD
m_l	Lambertian emission order
n	Number of transmitted bits per switching time
N_a	Concentration of acceptor dopant atoms
n_{con}	Internal refractive index of concentrator
N_d	Concentration of donor dopant atoms
n_e	Concentration of free electrons in conduction band

N_e	Number of generated electrons in a photodiode
$\langle N_e \rangle$	Average number of generated electrons in the photodiode
n_h	Concentration of holes in valence band
n_i	Carrier concentration of intrinsic semiconductors
N_p	AWGN power
N_{ph}	Number of incident photons
$n(t)$	AWGN noise signal
P_B	DC background optical power
$P_{B\_\mathrm{shot\_noise}}$	Shot noise power due to background optical power
P_{detected}	Detected power by the photodetector
$P_{\mathrm{interf}}(t)$	Time varying interference optical power
$P_{\mathrm{interf\_high}}(t)$	High frequency component of interference optical power
$P_{\mathrm{interf\_low}}(t)$	Low frequency component of interference optical power
$P_{\mathrm{interf\_shot\_noise}}(t)$	Time varying shot noise power due to interference
$P_{\mathrm{noise}}(t)$	Overall noise power due to interference source
P_o	Optical power
P_{received}	Received power at the receiver
P_t	Transmitted optical power
$\mathrm{PRBS20}$	Pseudo-random bit sequence of length 2^{20}-1 bits
Q	Quality factor
r	Reflection coefficient
$R(\lambda)$	Wavelength-dependent responsivity
r_B	Bit rate
R_F	Feedback resistor
R_{load}	Load resistance

R_{ref}	Reference resistance
S_p	Signal power
$s(t)$	Time varying signal
t	Time
T	Absolute temperature in K
$T_s(\Psi)$	Optical filter gain
$t_{10\%}$	time at 10% of maximum voltage value
$t_{90\%}$	time at 90% of maximum voltage value
T_b	Bit duration
t_f	Fall time
t_{off}	Switching-off time
t_{on}	Switching-on time
t_r	Rise time
T_{switch}	Switching time
V_0	Built-in voltage of a *p*-*n* junction
V_{bias}	Bias voltage
V_C	Capacitor voltage
V_{EB}	Emitter-base voltage
$V_{EC_{\mathrm{sat}}}$	Emitter-collector voltage at saturation
V_F	Forward bias voltage
V_R	Reverse bias voltage
V_S	Source voltage
V_{th}	Threshold voltage
$W(\lambda)$	spectral radiant emittance of the sun
x	Horizontal position

$y(t)$	Output of the communication system
β	Current amplification factor of BJT transistor
ε	Dielectric constant
η	Quantum efficiency
λ	Wavelength
λ_c	Cut-off wavelength
μ	Mean of the signal
μ_0	Mean voltage of logic ‘0’ rail
μ_1	Mean voltage of logic ‘1’ rail
μ_h	Mobility of holes
μ_e	Mobility of free electrons
σ	Conductivity of an intrinsic semiconductor material
σ_0	standard deviation of logic ‘0’ rail
σ_1	standard deviation of logic ‘1’ rail
σ^2	Noise variance
σ^2_{Shot}	Variance of shot noise
$\sigma^2_{\mathrm{Thermal}}$	Variance of thermal noise
Φ	Angle between the normal axis of the transmitter surface and the irradiance
$\Phi_{1/2}$	Semi-angle at 50% illuminance of the LED
Ψ	Angle between the normal axis of the receiver surface and the received beam of light
Ψ_{con}	Field of view of concentrator

Chapter 1

Introduction

1.1. Background: Connectivity in IoT devices

From smart toothbrushes that measure how long you brush your teeth to smart fridges that notify you when the groceries are running low and gardening gadgets that remind you to water the plants, smart inter-connected devices are a reality in the contemporary society. What was only considered science fiction a few years ago is now part of the retail market and the every-day life [1]. The concept of internet of things (IoT) - first introduced by the British technology pioneer Kevin Ashton -implies that computers are not anymore the only devices that are connected to the internet, nor are they limited to the inputs provided by humans. Instead, computers now have “eyes and ears” thanks to small low-complexity and low-cost smart sensing devices that communicate to provide information about the changes in the environment [2], [3].

IoT refers to networks of objects that are used in everyday life which have the hardware as well as the software capabilities for data exchange. The main function of IoT devices lies in “sharing, gathering and forwarding information adaptively in accordance with the obtainable data” [4]. Accordingly, IoT devices are the perfect fit for employment in smart environments such as healthcare monitoring, security as well as personal and home area networks [3].

During the past decade, the IoT has grown at such a tremendous speed. Although the technology was first heard of in 2002, it is estimated that there are currently over 30 billion IoT devices sold on the market [5], [6]. It is foreseen that the investment in the field will reach more than $60 trillion over the next 15 years [7] and the IoT market will reach $267 billion [8] and 212 billion entities worldwide by the end of 2020 [9].

But while the potential of IoT devices in the market is huge, its progress faces a great challenge in finding the right technology for communication between the ever-increasing number of devices. Given the huge amount of data generated and exchanged by those devices, a great impact on the network in terms of overcrowding, latency and transmission bandwidth scarcity is anticipated. Hence, a reliable yet low-complexity and inexpensive communication technique is necessary for data exchange. A green communication technique is required that is not only secure, but also operates on low power to be easily integrated in small devices [2], [10], [11].

Most IoT applications require only sending a few bits at a time such as flags or integer numbers representing environment sensing information [12]. Moreover, the data transmission between many IoT devices takes place relatively infrequently, such as every few seconds or even minutes [13]. A continuous stream of data is therefore not necessary. Hence, a low-data rate and short-range communication technology is sufficient for such applications [14].

Very few communication technologies comply with those requirements for low-data rate communication between IoT devices. Wireless Fidelity (Wi-Fi), Bluetooth and cellular communication are the most famous amongst them, especially for the higher data rate applications that require non-line-of-sight and a wide coverage range [15]. However, in the low-data-rate and low-complexity applications these technologies are an overkill. In addition, they fail to provide an eavesdropping-proof environment for communicating between those devices without complex encoding algorithms. Also, Wi-Fi and cellular communication require high power for sending and receiving as well as complex encoding and decoding, which is against the nature of most IoT sensing devices [16].

Cellular communication specifically is mainly designed for higher data rates applications such as voice calls, streaming videos or sharing large images and browsing the internet. It therefore targets applications that require high range of coverage and employs the licensed spectrum of radio frequency (RF). Because it requires expensive licensing and complex hardware, it is considered too expensive and power savvy for typical IoT sensing devices [16].

The main challenge for the communication between IoT devices however is how to fit in the extremely congested and highly regulated RF spectrum. The spectrum for wireless communication has nowadays become a scarce finite shared resource, that cannot cope with this ever-increasing demand [16].

The limited bandwidth of the RF along with the high demand poses a real problem especially in indoor environments with high user density scenarios such as sports events, airports and in emergency cases. Researchers found that 70% of all communications take place in indoor scenarios like homes and offices [4], [17], [18], which is mostly where contemporary IoT devices operate. In those situations, the RF spectrum becomes too congested that it cannot provide all users with the needed connectivity. The UK frequency allocations chart shown in Figure 1-1 shows how crowded the RF spectrum is. The addition of millions or even billions of IoT devices just aggravates the so-called “spectrum crunch” problem and emphasises the need for an alternative solution [19]. Especially with that high demand for connectivity and the exponentially growing number of connected devices, the need for an alternative to the traditional radio frequency is pushing the scientists towards researching other techniques to solve the ‘spectrum crunch’ problem [19].

One of the solutions to the spectrum overcrowding is the use of smaller and overlapping cells for communication, such as nano-cells and femto-cells in addition to the already existing microcells [16]. These smaller cell sizes allow for frequency spectrum reuse and provide a spatial division multiplexing of the communication channel. However, this is not possible due to the wide communication range of many RF communications such as Wi-Fi and cellular. Applying frequency reuse on such a scale will add complexity because it would require handling the interference between the single cells and complex managing of spectral resources [20]. This gap in appropriate communication technologies for simple IoT devices paved the way for the use of visible light communication.

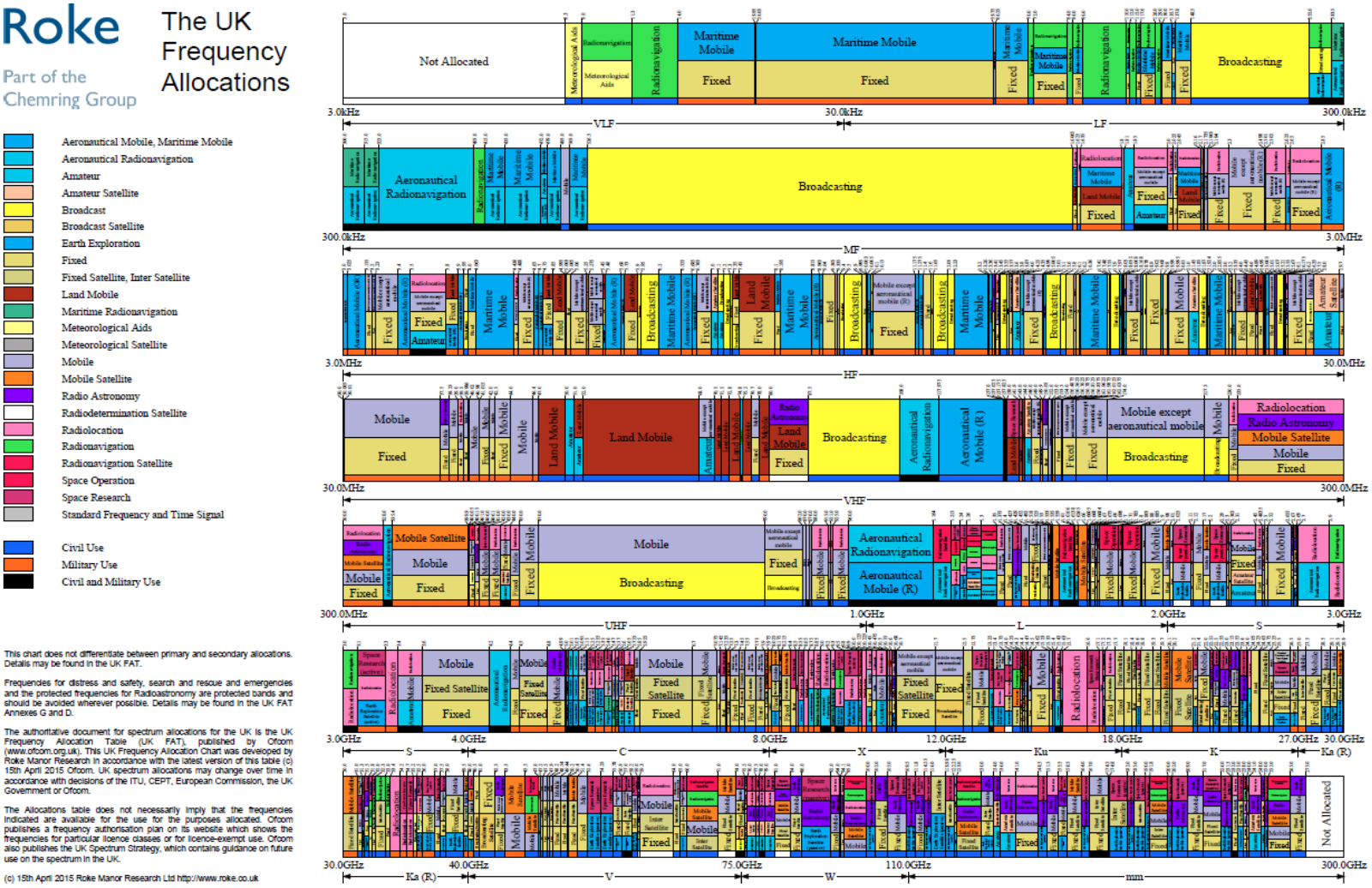

Figure 1-1: UK frequency allocation chart [REF: https://www.roke.co.uk/media/roke-hub accessed: 10/6/2020]

1.2. Visible Light Communication for IoT

In this gap of technological advancement in the field of wireless communications for IoT devices, optical wireless communication (OWC) and especially visible light communication (VLC) found a fertile ground for growth and flourishing [1].

Optical wireless communication is a type of telecommunications that relies on light for information exchange, whether in the infrared (IR) range or the visible light range. Visible light communication is a sub-category of optical wireless communication that relies on visible light in the wavelength range from 380 nm to 720 nm for data transfer [21]. It occupies the range between 400 THz and 800 THz in the electromagnetic spectrum as shown in Figure 1-2.

VLC has many advantages over regular RF telecommunications technology, especially for IoT applications [1]. First, it is capable of overcoming the restrictions of the regular RF spectrum because it has a huge, unexploited and unlicensed spectrum, in the terahertz (THz) region. It causes no interference with other wireless communications technologies and is therefore safe to use in RF

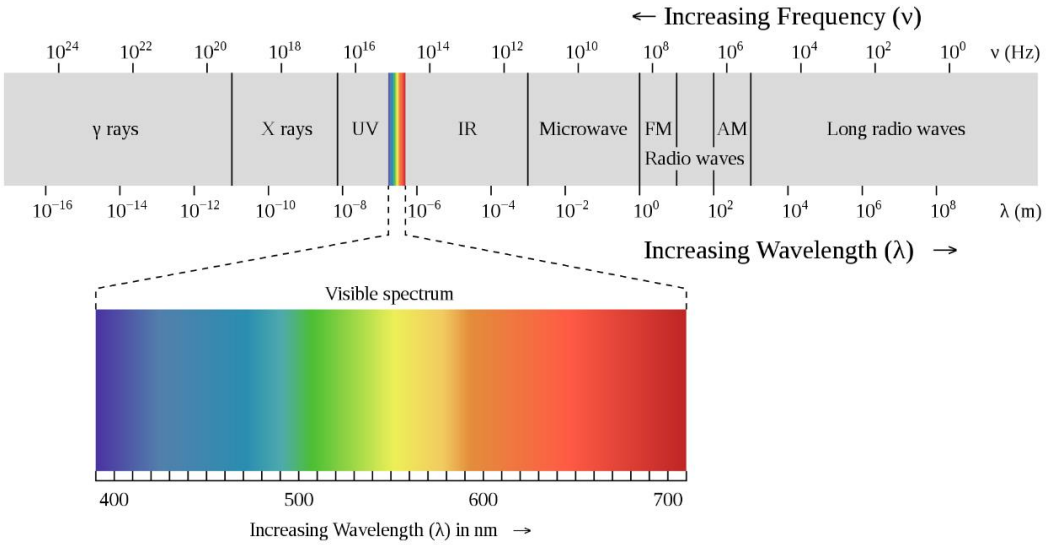

Figure 1-2: Visible light communication spectrum in electromagnetic spectrum

sensitive environments such as hospitals, control rooms and airplanes. Unlike the remainder of the THz region which has safety limitations on life tissue and is therefore not suitable for terrestrial communication, VLC is a safe technology that poses no health hazard for humans and pets if the eye safety standards are respected [22].

Besides, it has a very small cell size due to its confinement by the walls of a single room. This confinement aggregates the inherent security against eavesdropping. Moreover, VLC is also easy and cost-efficient to deploy and is therefore attractive in industrial and business applications [23]. VLC is regarded as a green and energy-efficient technology because it employs light already utilised for illumination and piggybacks the information on it. In addition, it employs mainly light emitting diodes (LED) as transmitters, which are the core of contemporary low-power lightning solutions [24], [25].

The dual LED functionality, namely being able to illuminate as well as act as transmitter for wireless communication, makes the field of VLC especially attractive for both scientific research and the industry as an alternative or complementing technology to RF for IoT connectivity [26].

Although VLC has many advantages, it also has its own set of challenges that prevent it from completely replacing other communication technologies. The indoor VLC channel susceptibility to noise and interference from other ambient light sources and sunlight prevents the long-distance coverage of VLC and impacts its reliability [27]. In addition, VLC lacks an identical uplink channel (to the downlink) and mostly depends on RF technologies or an IR channel for the uplink. In order to design an entire full-duplex VLC system, two parallel channels need to be implemented: one for the downlink and another for the uplink. This not

only doubles the cost, energy consumption and complexity of the VLC system, but is also an obvious disadvantage compared to other RF communication technologies that rely on a single antenna for transmitting and receiving [23]. A bidirectional VLC system encourages harnessing the full capabilities of VLC as an augmenting technology for indoor wireless communication.

1.3. Research Motivation

Inspired by the idea of employing the same device (antenna) for transmitting and receiving signals, LED-to-LED communication grew as a branch of the VLC tree [23]. LED-to-LED communication employs the LEDs on the ends of the communication channel as both transmitters and receivers of visible light signals. It makes use of the physical properties of the semiconductor material *p-n* junction inside an LED that is capable of emitting as well as detecting light upon changing the applied bias voltage: in forward bias, the *p-n* junction releases electrons from the conduction to the valence band, releasing thereby energy in the form of photons. When reverse biased, the photons falling on the exposed *p-n* junction provide electrons from the valence band with energy, causing them to move to the conduction band and create a small photocurrent to flow from the LED, similar in type but lower in magnitude to the photocurrent induced by a regular semiconductor PIN photodiode [28].

Employing an LED both as transmitter as well as photodetector in the VLC channel not only reduces the complexity, cost and power consumption of the system, but also majorly increases the value of the single LED. An LED has thereby a triple functionality: illumination, data transmission and data reception.

The idea of using an LED as light detecting device first originated from Dietz's paper, in which the author employs the LED as an ambient light sensor [29]. In his paper, Dietz measures the change in the LED's internal capacitance at the end of the light measurement interval. Dietz notices that the capacitance drops proportionally to the amount of received light. The system proposed by the author depends only on a low-cost microcontroller whose pins switch between receiving and capacitance charging modes.

In their study, Schmid *et al.* depend on the same principle for developing a VLC system, in which the LED can have the double function as transmitter and receiver for communication. Due to the limited data rate of just 1 kilobits per second (kbps) and the low sensitivity of the LED compared to a regular PIN photodetector, the recommendation of the paper is to use such an LED-to-LED system in very low-complexity and low-data rate applications, where the distance between the communicating devices is kept at maximum of a few centimetres. An example of such a system is communication between IoT devices such as toy-to-toy communication and toy-to-textile communication [30].

Kowalczyk *et al.* proposed an LED-to-LED communication system, which depends not on the light dependency of the internal capacitance of the *p-n* junction, but on its ability to produce photocurrent upon receiving visible light. Although this photocurrent is very small in magnitude, it suffices for successful light detection in combination with a high-gain transimpedance amplifier circuit, similar to the way a PIN-photodiode-induced photocurrent is amplified. Using off-the-shelf red and amber LEDs as well as post-equalisation techniques, the authors designed a one-way LED-to-LED communication link that is able to reach a data rate of 100 megabits per second (Mbps) [31]. Chun *et al.* proposed a similar system, which reaches data rates as high as 110 Mbps using LEDs only

as transmitters and receivers over a 5 cm distance [32]. However, the complexity of their proposed system is high due to the use of complex modulation techniques (OFDM) and an array of focusing lenses and optical components to filter and concentrate the light on the active area of the LED. Besides, a high-end and expensive high brightness red LED is employed in their experiment, which is not suitable for the use in indoor illumination or low-complexity applications.

All the employed LEDs in the published studies of LED-to-LED communication are single-colour LEDs that are not suitable for emitting white light. This is mainly due to the fact that LEDs can only detect wavelengths that are lower than or equal to the peak wavelength they are emitting [33]. The energy of a photon corresponds to the bandgap energy of the semiconductor material that is emitting it and is inversely proportional to its wavelength. A semiconductor-based photodetector can detect photons of equal or higher energy than its own bandgap energy. Hence, a red/amber LED which transmits at the upper wavelength limit of the visible light spectrum (at 650 nm) can receive light in the green (550 nm) and blue (450 nm) range, but a blue LED is not capable of receiving visible light at all. Besides, the most commonly used white LEDs have a phosphorus coating on their semiconductor die to turn the generated blue light into white light. This coating prevents light from the outside to enter the semiconductor die, rendering the blue-phosphorous LEDs incapable of detecting light [33].

The very low data rate approach for LED-to-LED communication employed by Schmid *et al.* as well as the higher-speed and high-complexity approach employed by Chun *et al.* and Kowalyzc *et al.* both fail to provide a solution for low-complexity, low-speed and low-data-throughput communication. While the first approach reaches only a data rate of 1 kbps that is sufficient only for transmitting flags between toys, the latter approach offers a high-speed

connection possibility but makes sacrifices in terms of high complexity and cost. Besides, most of the published literature offers only a one-directional link, not a bidirectional system. An LED-to-LED solution that allows bidirectional data exchange between IoT devices at intermediate speeds above the 1 kbps threshold is to our knowledge missing from the current published research.

To fill in this gap in research, this thesis proposes a bidirectional half-duplex LED-to-LED solution that depends on off-the-shelf white RGB LEDs instead of single-coloured LEDs. RGB LEDs are white light emitters that are also capable of receiving visible light signals. To optimise the detection circuit for the LED photodetector, one of the main contributions of this thesis is to study the properties of the RGB LED both as transmitter and photodetector. The knowledge of the LED bandwidth as transmitter and detector and its responsivity at varying wavelengths and the biasing voltages is acquired from the empirical results of experiments that are proposed and designed in this thesis. Based on the knowledge gained about these properties, a transimpedance-amplifier-based circuit is designed to maximise the performance of the LED as photodetector. A current-mirror-based transmitter is employed as LED driver to provide the optimum driving current. An optimised matched filter is proposed at the output stage to augment the system and push its error-free transmission distance further. An analogue switch is lastly characterised and proposed as a solution for switching between transmission and detection mode, providing thereby a fully functioning half-duplex bidirectional LED-to-LED communication system.

1.4. Aims and Objectives

The main aim of this thesis is to design and implement a bidirectional half-duplex low-complexity LED-to-LED communication system based on off-the-shelf white RGB LEDs that can be integrated as the communication module in IoT devices. The system should provide low-speed connectivity between devices over a short line-of-sight (LOS) channel without increasing the system hardware or processing complexity. The objectives of this study are therefore:

1. To design and implement an LED driver circuit that provides the required current to modulate the RGB LEDs.
2. To design, implement and analyse the receiver circuit to optimise light detection by the LED photodetector.
3. To propose, design and characterise a suitable low-complexity technique for switching between transmission and detection mode in order to achieve a half-duplex bidirectional LED-to-LED communication system.
4. To analyse and model the noise and interference due to the contemporary ambient light sources of the VLC channel.
5. To analyse and characterise the behaviour and properties of an off-the-shelf RGB LED both as transmitter and as photodetector.
6. To propose a suitable post-processing low-complexity technique that optimises the system performance.

1.5. Original Contribution to Knowledge

The main contributions of this thesis are outlined as follows:

- Off-the-shelf RGB LEDs are employed as PN photodetectors. Their properties are investigated and empirically measured. It is proven that the red sub-LED is most suitable as photodetector while the green sub-LED is optimum for transmission. The red sub-LED has a receiving bandwidth up to 4.9 MHz and responsivity to green light of 0.2 mA/W. The experimental results also prove that the red sub-LED is capable of detecting light even when under 2 V of forward bias. Those findings are published in [34].
- A low-complexity LED-to-LED communication link is designed and implemented. The maximum achieved data rate is 200 kbps at a transmission distance of 1 cm [35]. The system is optimised using a matched filter to increase the error-free transmission distance to 4 cm at 200 kbps data rate, exceeding the performance of a PIN photodetector in the same setup.
- A bidirectional half-duplex LED-to-LED communication system is designed, implemented and experimentally characterised. To mitigate the shortcomings of the analogue switching circuit, a smart low-complexity algorithm is designed to regulate the timing of transmission and detection. The overall error-free data rate is 110 kbps with a switching frequency of 100 Hz in a back-to-back configuration.
- The interference of the contemporary ambient light sources and their effect on the visible light communication is experimentally measured and extensively analysed. As a result, the mathematical model of that interference is derived and published in [27].

The tree diagram Figure 1-3 shows the types of indoor optical wireless communications and highlights the path that this thesis focuses on with solid connection arrows. The green nodes in the diagram highlight the areas where this thesis offers an original contribution to knowledge.

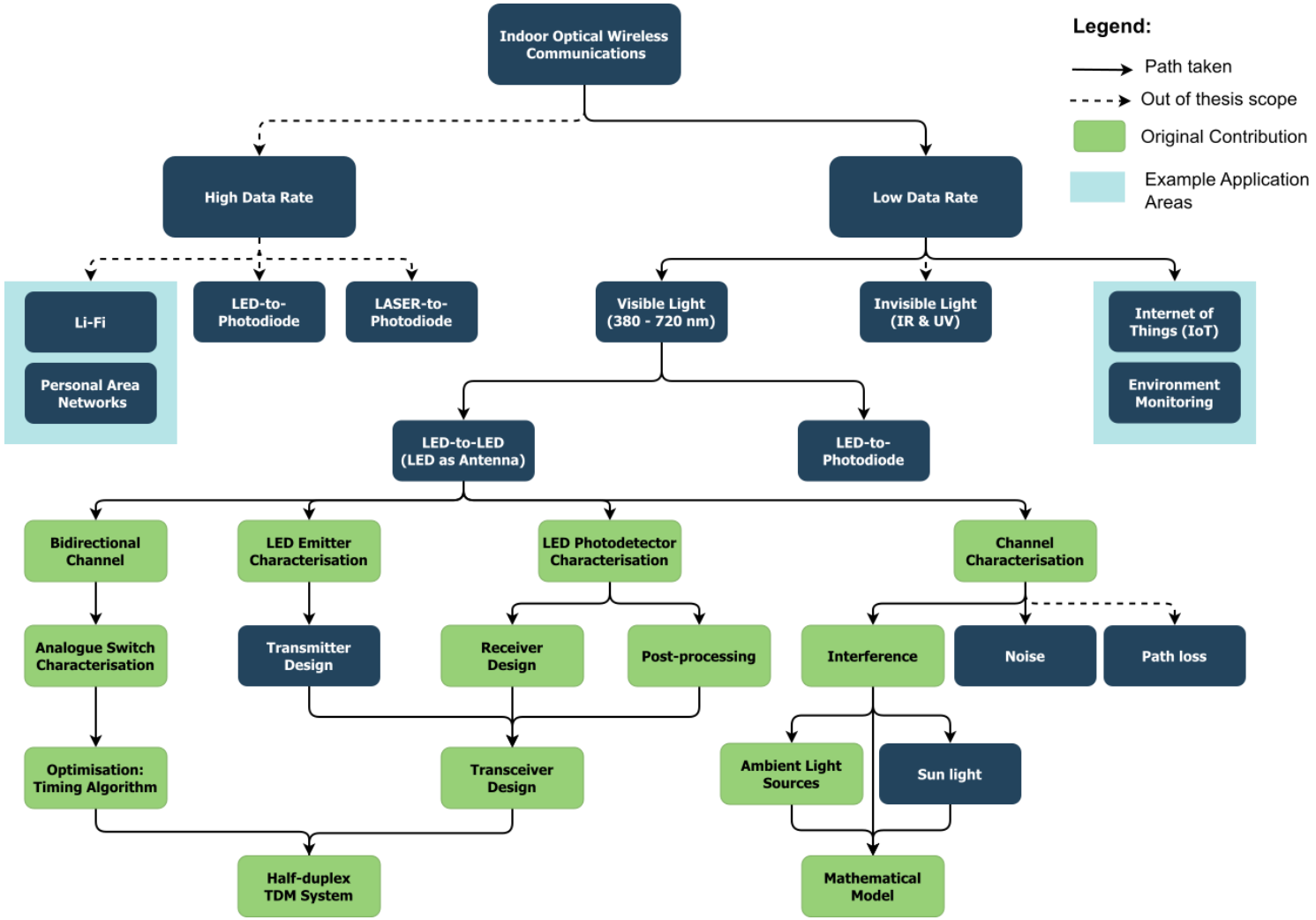

Figure 1-3: Tree Diagram of indoor optical wireless communications highlighting the path taken in this thesis with solid arrows and the thesis contribution area in green

1.6. List of Publications

- “Experimental Characterisation of RGB LED Transceiver in Low-complexity LED-to-LED Link”, in *SENSORS journal*, MDPI, October 2020
- “Characterisation of RGB LEDs as Emitter and Photodetector for LED-to-LED Communication,” in *2020 12th IEEE/IET International Symposium on Communication Systems, Networks and Digital Signal Processing-(CSNDSP)*, 2020.
- “Characterisation and Interference Model of Contemporary Artificial Light Sources Noise on a VLC channel,” in *2018 11th International Symposium on Communication Systems, Networks & Digital Signal Processing (CSNDSP)*, 2018, pp. 1–6.
- “LED-to-LED Communication for Li-Fi”, Poster in PGR Conference at Northumbria University, 2017.

1.7. Thesis Organisation

The thesis is divided into 8 chapters. Chapter 2 concentrates on a detailed literature review on visible light communication and LED-to-LED communication, respectively. Chapter 3 analyses the properties and performance characteristics of the RGB LED both as transmitter as well as photodetector. Chapter 4 introduces the modules for the proposed LED-to-LED system, which include the LED driver, the transimpedance-amplifier-based receiver and the analogue switching circuit. Each module is separately characterised, and the overall electronic back-to-back system is evaluated without the effect of the channel or the optical components. Chapter 5 characterises the LED-to-LED communication channel, introduces the sources of noise and interference that are perceived by the photodetector and derives an interference mathematical model for the contemporary ambient light sources. In chapter 6, the proposed LED-to-LED link is implemented, experimentally characterised and optimised for the LED characteristics. A matched filter technique is employed to optimise the performance of the proposed LED-to-LED communication link. Finally, in chapter 7, the complete half-duplex LED-to-LED communication system is designed and experimentally characterised. The effect of the switching between the transmission and photodetection modes is evaluated and minimised using a timing algorithm. Chapter 8 then concludes the thesis and discusses the future work.

Chapter 2

Visible Light Communication Enabling the Internet of Things

2.1. Introduction

The requirement for connectivity is increasing every day with the ever-growing number of IoT devices. RF technologies are leading the way in IoT connectivity, however they put a lot of pressure on the already overcrowded RF spectrum. That is why researchers are focusing on alternative communication technologies for such devices. During the last decade, VLC has matured as a complementary and supplementary technology for RF. It allows the use of readily available LEDs to provide a low-cost, low-energy and low-complexity yet reliable solution for connecting typical small IoT devices. In this chapter, the advancement of VLC as a connectivity solution for IoT is introduced and its main properties are characterised.

2.2. Visible Light Communication Introduction

Visible Light communication is a type of optical wireless communications that depends on LEDs and LASERs for data transmission using the visible spectrum between 380 nm and 720 nm. Since the human eye can detect flickering only at frequencies less than 100 Hz, it is possible to transfer data over fast switching of the already available LEDs used for illumination or status indication without affecting the visibility or illumination quality for humans [36]. It has been proven that by employing dc-balanced signalling for VLC, the quality of light is maintained in spite of data transmission over the same light sources [37].

2.2.1. Brief History and Advancement of VLC

In fact, VLC is a very old communication technology that has been used in the form of smoke signals, fire beacons and mirroring of sunlight by many cultures. It is reported that the ancient Greeks were the first to use those visual signals for ship-to-ship communication while the ancient Chinese tribes used smoke signals for informing their tribes of danger or for calling for help in times of war [38]. In 1792 the first optical telegraph network was built by the French engineer Claude Chappe. This network was used by the French military for almost 60 years as a main communication channel. Chappe's semaphore tower design consisted of a tower on top of which is a large crossbar with pivoting arms, large enough to be seen with the naked eye from miles away. Depending on the position of those arms, up to 196 different combinations were possible, allowing the encoding of thousands of messages, phrases and symbols [39].

Although those types of visual communication rely on visible symbols to convey information, none of them modulate the visible light to act as carrier for the information. It is reported that the first attempt on real free space visible light communication was by Alexander Graham Bell, who invented the photophone in 1880 [40]. In his experiment, Bell modulated the sun light with his own voice by employing vibrating mirrors on the transmitter side. The light signal was then received by a parabolic receiver equipped with a selenium cell [40].

The leap in the advancements of optical wireless communications, however, began in the year 1979 when Gfeller and Bapst reported the first indoor optical wireless communication system based on IR light of wavelength 950 nm, which promised a data rate of 1 Mbps and coverage of an entire office room [41].

The first attempt to employ white LEDs for transmission in addition to their main illumination function appeared in 2003 when Tanaka *et al*. proposed an on-off-keying (OOK) based system with maximum data rate of 400 Mbps [42]. Since then, an avalanche of research papers has been published in the field of visible light communication, reporting data rates in the gigabit per second (Gbps) range and employing a multitude of modulation, multiple access, detection and optical focusing techniques to improve the system performance. In 2011, the term ‘Light Fidelity’ (Li-Fi) was first introduced by Harald Haas in his TED talk, which refers to a wireless networking technology based on visible light communication that is capable of competing with the wireless-fidelity (Wi-Fi) [24].

VLC has been on the rise ever since. Especially with the high demand for connectivity and the exponentially increasing number of connected devices, the need for an alternative to the traditional radio frequency (RF) communication is pushing the scientists towards researching other non-conventional techniques to alleviate the 'spectrum crunch' problem [43]. The potential of VLC in augmenting and replacing RF technologies in indoor wireless communications caught the attention of many research institutions worldwide. High-data-rates VLC systems were especially attractive for researchers. In 2009, Le Minh, O'Brien and Faulkner reported a 100 Mbps VLC system that employs only an analogue equaliser and simple non-return-to-zero (NRZ) on-off-keying (OOK) modulation [44]. Moreover, orthogonal frequency division multiplexing (OFDM) was used by Vucic *et al*. to achieve a VLC system capable of data rates up to 200 Mbps over a 70 cm distance [45]. In 2012, the 1-Gbps-mark was hit for the first time by a VLC system with a single LED using OFDM [46].

The research interest in VLC led to the formation of the VLC consortium, in which more than 20 countries and many enterprises and manufacturers have participated [43]. This interest was again highlighted in the European OMEGA project, which focuses on the study of gigabit home access networks [47]. In 2012, the IEEE 802.15.7 standardised visible light communication with data rates up to 96 Mbps and promised techniques for LED dimming without causing noticeable flickering [48]. During the past decade, VLC technology has matured rapidly, demonstrating not only reliability and energy efficiency, but also vast data rates up to several hundred Gbps [49]. The IEEE 802.11bb task group was established in May 2018, with the aim of amending the Medium Access Control (MAC) and Physical Layer (PHY) of IEEE 802.11 with Light Communications [50].

Currently, the practical research in the field of VLC is divided into two categories: The first category pushes the limits of bandwidth and speed of the VLC system to replace and complement high-end RF technologies employed for data streaming, internet and telephony communication. A typical example for solutions in this category is offered by PureLifi, a company providing ready-to-deploy Li-Fi systems in homes, offices and healthcare centres [51]. While this category of VLC research is very important in putting VLC in the high rank it deserves amongst the RF technologies, it is extremely expensive to implement due to its complex hardware and processing requirements. On the other hand, the second category notices that not all application areas require such high data throughputs and speeds. Instead, those applications require a communication technology that focuses on the low cost of implementation, reliability, availability and low complexity. A typical example of a range of applications falling in this category are IoT devices. Thus, in this category, the researchers employ off-the-shelf components along with simple modulation and processing techniques, which make VLC affordable and realistic in such applications [52]. This thesis proposes a system that falls in this latter category.

2.2.2. Advantages of VLC Over Other RF Technologies

Due to the increased connectivity requirements, the RF spectrum became very crowded and cannot anymore handle the high mobile data traffic. In addition, the interference between the different RF technologies became too high, which increased the latency and decreased the reliability of the RF communication technologies. On the contrary, VLC causes no stress on the RF spectrum because it operates in the large and freely available Terahertz region [53]. Due to light's confinement within a limited space and its inability to penetrate opaque materials, VLC is inherently more secure than other RF technologies. It also allows the creation of nano and femtocells for communications and has much higher space and frequency reusability compared to other RF technologies [54]. In addition, it is an energy saving form of communication since it depends on LEDs, which are the core of the contemporary energy efficient lightning [25]. By piggybacking the data communication on the already available lighting appliances, the energy saving factor of VLC is twofold: employing an already low-power transmitter device as well as needing no extra power for operating the communication device. Moreover, VLC is an inexpensive and fast to implement communication technology. Due to its low power consumption, its small cell size and its immunity to RF interference, VLC is considered a major player in the era of 5G and IoT [25]. Visible light communication is therefore increasingly gaining popularity as a complementary or in some application as an alternative technology to radio frequency [55] and is considered to be a smart move in the direction of green communication [56]. Table 2-1 compares the properties of VLC and other RF technologies and highlights the VLC advantages.

Table 2-1: Comparison between VLC and RF properties

Property	RF	VLC
Obstacle penetration	Yes	No
Interference	With other RF technologies	With ambient light sources
Health hazard	Potentially	No
Bandwidth regulation	Requires licensing	Free, no license required
Implementation cost	High	Low
Line-of-sight (LOS)	No LOS	LOS and diffuse
Covered distance	Medium to high	Low
Mobility	Yes	Limited
Power consumption	Medium	Low
Transmitter	Access point	LED
Path loss	High	High

2.2.3. Challenges of VLC

Although VLC has majorly matured as a communication technology over the past decade, it still faces many challenges. One of the major problems is the limited bandwidth of off-the-shelf white LEDs, which lies in the range of 10 MHz for blue but only at 4 MHz for the yellow component produced by the phosphorus coating [44]. To mitigate this problem, researchers proposed either employing a blue filter on the cost of reducing the received power by over 90%, or by post-equalisation, which in turn increases the complexity and processing power [44]. This thesis proposes deploying RGB LEDs instead of the regular blue-phosphorus LEDs for a LED-to-LED communication system. Employing this kind of white LED maximises the bandwidth of the LED as receiver and opens the possibility of employing three different channels instead of just one without sacrificing the received power.

When employed in outdoor environments, the VLC channel faces the problems of atmospheric losses [57]. These cause the absorption as well as the scattering of the information-carrying light beams by obstacles, dust particles, snow, rain, water particles in high humidity, fog and snow. Moreover, visible light rays experience scintillation due to the atmospheric turbulence and the different refractive index of the air medium because of the differences in air temperature [57]. This disrupts the data transfer and the channel quality. Aside from those factors, direct sunlight interferes majorly with visible light communication rays, which might cause photodetector saturation and prevent visible light communication [58].

In an indoor environment, VLC faces a different set of challenges. Firstly, shadowing occurs due to passing persons or moving objects, which prevents the photodetector – at least temporarily – from receiving information from the transmitting LED. To mitigate that effect, redundant data for error correction is transmitted, reducing thereby the total throughput and data rate of the system [59].

In addition, dimming and turning off the light – which is a requirement in office and home environments for mood setting, energy saving or other reasons – reduces the light power of the emitter LED, thereby reducing the signal to noise ratio (SNR) of the VLC system or even stopping data transmission completely. To solve that problem, researchers proposed methods in which data transfer continues at very dim light that is not perceived by the human eye on the cost of increasing the complexity of the system. Thereby, the data stream continues even though users think that the light is turned off [60]–[62].

In indoor environments, where other ambient light sources such as incandescent and fluorescent light bulbs are used for illumination, the VLC channel suffers from interference from these sources [63]. Because of their driving circuitries, these sources do not have a DC non-varying light level that can just be subtracted as DC noise at the receiver. Instead, they transmit time-varying light signals. Hence, their interference needs to be accounted for when designing a VLC receiver [64]. To take their effect into account, this thesis proposes a mathematical model for the interference components of modern and contemporary ambient light sources in chapter 5.

One of the major challenges that VLC faces is the lack of a reliable uplink in a small form factor. If a VLC-based uplink channel is desired, a separate transmitter-receiver pair is required, which doubles the cost and complexity of the whole communication link. Because a VLC system depends on two different devices for transmitting and receiving data (an LED as transmitter and a photodetector as receiver), a bi-directional channel is not inherently possible. Typically, the VLC channel is used for downlink only and an IR channel or another RF technology such as Wi-Fi or Bluetooth is employed for the uplink [65]. As a possible solution, a bidirectional LED-to-LED communication system is proposed and implemented in chapter 8, which employs the same device, namely an LED, for transmitting and receiving the light signals. In this manner, a bi-directional VLC communication channel can be implemented while keeping the cost, space requirements and complexity at a minimum.

2.3. Typical VLC system

A typical VLC system block diagram is presented in Figure 2-1. In the figure, blocks with dashed outlines are optional while those with solid outlines are the main components of a VLC system that cannot be omitted.

On the transmitter side, an LED driver combines the DC signal required for biasing the LED and the modulated data signal from the data source. Depending on the application, required data rates and current magnitude, the LED driver can be either a bias tee or an electronic circuit based on active components such as transistors and operational amplifiers [66]. Optional optical lenses concentrate the emitted light beam and direct it towards the receiver or diffuse the light signal to provide uniform illumination [67]. The modulated light beam travels through the free-space channel towards the receiver side. At the receiver optional optical lenses and concentrators focus the incoming light beam on the active area of the photodetector while optional filters remove light components that are not necessary for the communication process. The photodetector then converts the modulated incoming light signal in photocurrent, which is then amplified by the transimpedance amplifier (TIA). At the data sink, the output voltage from the TIA is then decoded and further processed [67].

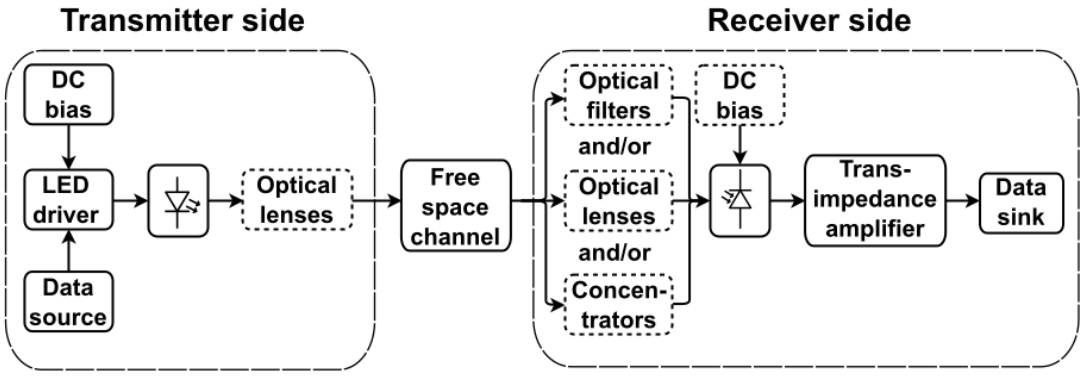

Figure 2-1: Typical VLC system block diagram

There are two types of LEDs that are typically used in VLC: single-coloured LEDs and white LEDs. As their name indicates, single-coloured LEDs can emit only one colour of light, such as red, amber, yellow, green or blue. On the other hand, white LEDs are capable of producing white light either by combining multiple light colours (such as red, green and blue (RGB)) or by converting blue colour into yellow, which in combination with blue appears as white light [67]. The theory of operation of those LEDs is discussed in more details in chapter 3.

Typically, photodetectors employed in a VLC system are either PIN photodiodes or Avalanche photodiodes. Photodiodes can detect light under zero or reverse bias. At zero bias, i.e. in photovoltaic mode, the precision of the photodetector is higher, and the produced noise is lower. This mode is mainly used in energy harvesting applications or where high-precision, but low-data-rate communication is required. On the other hand, the reverse bias mode, i.e. the photoconductive mode, the bias voltage increases the width of the depletion layer between the *p*- and *n*- sides of the photodiode, decreasing thereby the capacitance of the photodiode. This results in higher speeds of operation on the cost of increasing the noise and the dark current. That's why it is mainly employed in applications, where high speed of transmission is essential [68]. The different configurations of the TIA are discussed in further details in chapter 4.

To derive the VLC channel response and determine the effect of the optical filters, concentrators and photodetector active area of the on the received power, an indoor VLC system in a typical indoor environment is considered next.

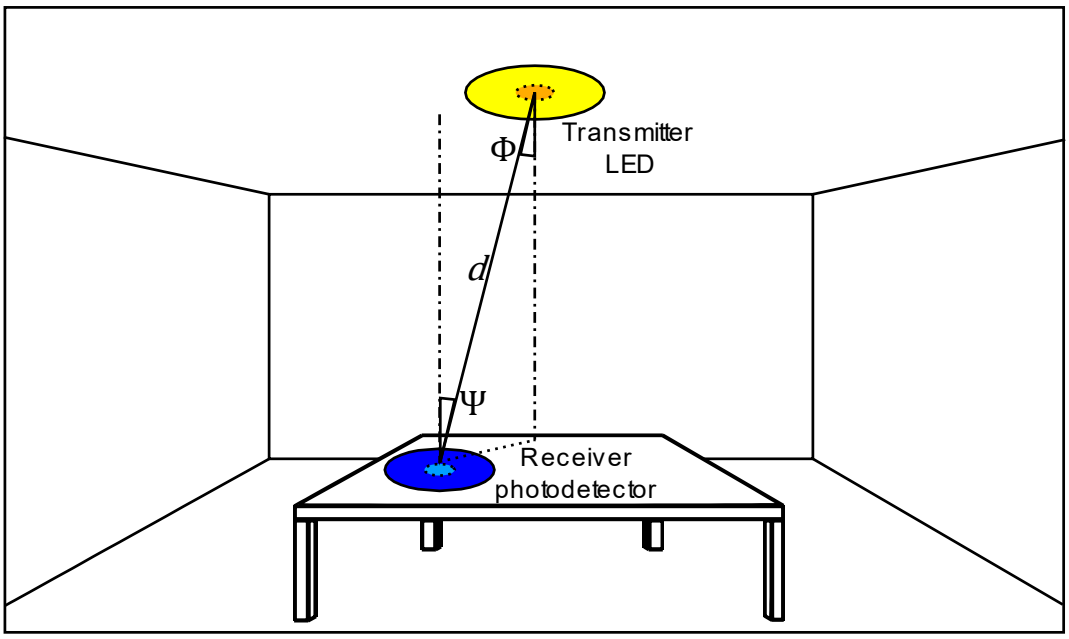

Figure 2-2: VLC in a typical office environment

A simplified office room with integrated VLC system is shown in Figure 2-2. Assuming a single source VLC system with an LED transmitter having a Lambertian radiation pattern, the radiation intensity at any point in the room is [67]:

$$I(\Phi) = I(0)\cos^{m_l}(\Phi), \tag{2.1}$$

where Φ is the angle between the normal axis of the transmitter surface and the irradiance, $I(0)$ is the maximum luminous intensity and m_l is the Lambertian emission order given by [67]:

$$m_l = -\frac{\ln(2)}{\ln(\cos\Phi_{1/2})}, \tag{2.2}$$

where $\Phi_{1/2}$ is the semi-angle at 50% illuminance of the LED.

The received power $P_{received}$ measured at the receiver is hence [67]:

$$P_{\text{received}} = P_t \frac{m_l+1}{2\pi d^2} \cos^{m_l}(\Phi) T_s(\Psi) g(\Psi) \cos(\Psi), \tag{2.3}$$

where P_t is the transmitted power by the LED, d is the distance between the transmitter and the photodetector, $T_s(\Psi)$ is the filter gain if present, $g(\Psi)$ is the concentrator gain if present and Ψ is the angle between the normal axis of the receiver surface and the received beam of light. Ψ can only vary between 0 and the field of view of the concentrator Ψ_{con} in this equation. If an optical concentrator is present in the VLC system, its gain function is described as [67]:

$$g(\Psi) = \begin{cases} \dfrac{n_{\text{con}}^2}{\sin^2 \Psi_{\text{con}}}, & 0 \le \Psi \le \Psi_{\text{con}} \\ 0, & \Psi > \Psi_{\text{con}} \end{cases} \tag{2.4}$$

where n_{con} is the internal refractive index.

The detected optical power is dependent on the effective area $A_e(\Psi)$, i.e. signal-collection area of the photodiode, which is given by [36]:

$$A_e(\Psi) = \begin{cases} A T_s(\Psi) g(\Psi) \cos(\Psi), & 0 \le \Psi \le \Psi_{\text{con}} \\ 0, & \Psi > \Psi_{\text{con}} \end{cases} \tag{2.5}$$

where A is the physical area of the photodetector. The detected power by the photodetector P_{detected} is hence [36]:

$$P_{\text{detected}} = A \cdot P_{\text{received}} \tag{2.6}$$

$$P_{\text{detected}} = A \cdot P_t \frac{m_l+1}{2\pi d^2} \cos^{m_l}(\Phi) T_s(\Psi) g(\Psi) \cos(\Psi). \tag{2.7}$$

The line-of-sight (LOS) DC gain H_{LOS} can hence be expressed as [36]:

$$H_{\mathrm{LOS}} = \begin{cases} \frac{(m+1)A}{2\pi d^2} \cos^{m_l}(\Phi) T_s(\Psi) g(\Psi) \cos(\Psi), & 0 \le \Psi \le \Psi_{\mathrm{con}} \\ 0, & \Psi > \Psi_{\mathrm{con}} \end{cases}. \quad (2.8)$$

2.3.1. VLC Channel Model

In the majority of VLC systems, intensity modulation (IM) with direct detection (DD) is employed. In this way, the intensity of the light emitted by the LED is modulated by the input signal. At the receiver side, the light signal is demodulated by directly converting it to photocurrent and the data is retrieved via enveloped detection. For a typical IM/DD VLC link suffering from additive white Gaussian noise (AWGN) (noise with a flat power spectral density over the entire frequency spectrum and Gaussian power distribution), the linear optical channel model is illustrated in Figure 2-3 [38].

The photocurrent $I_{ph}(t)$ can hence be given by [38]:

$$I_{ph}(t) = R(\lambda)\, P_t(t) \otimes h(t) + n(t), \quad (2.9)$$

where $R(\lambda)$ is the responsivity of the photodetector, $P_t(t)$ is the instantaneous transmitted optical power, $h(t)$ is the channel impulse response and $n(t)$ is additive Gaussian noise.

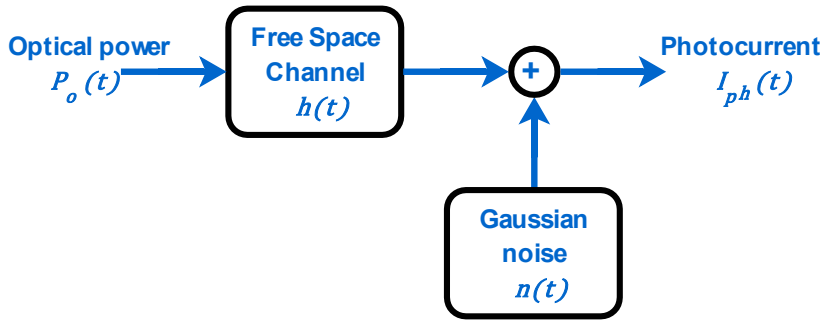

Figure 2-3: IM-DD channel model [38]

The responsivity $R(\lambda)$ of the photodetector is defined as the photocurrent I_{ph} produced per unit of incident optical power P_o as follows:

$$R(\lambda) = \frac{I_{\mathrm{ph}}(t)}{P_o(t)} \ . \tag{2.10}$$

If the transmitted light beam experiences reflections in the channel, those should also be accounted for in the channel model [38]. This is however out of the scope of this study because only short distance, obstacle-free channels are considered for the proposed system.

2.3.2. Application Examples of VLC

Because of its many advantages, VLC has high potential of being employed as communication technology in many applications both indoors and outdoors.

In the outdoors, VLC is employed as communication technology for intelligent transportation systems. The headlights of moving cars and vehicles, the streetlights as well as the traffic lights are all employed as network nodes and access points, conveying information about the road safety and providing connectivity for infotainment systems in smart cities [69]–[71]. In addition, VLC is employed in some cases as the last-mile communication technology between office or university buildings, in hard terrains or in RF restricted scenarios [72]. It is also used for advertisement and other location-based services [73]. Researchers are even employing blue light as information carrier in underwater VLC between submarines because it has been proven to face the lowest absorption coefficient in water, where other RF technologies fail [4].

In indoor environments, VLC has even more potential because it is protected from the interference by direct sunlight that disrupts its channel. In this scenario, the most popular application is Li-Fi, which aims to connect all handheld smart

devices to the internet at vast data rates, employing the lights mounted on the ceiling as access points in home and office environments. Moreover, due to Li-Fi's immunity against RF interference, it is employed for communication in hospitals, healthcare facilities and airplanes, where RF technologies could be dangerous on health monitors or navigation devices [53]. VLC is also employed for accurate indoor positioning both for humans in residential areas as well as products and packages in industrial environments, where global positioning services fail to provide the needed accuracy [74], [75].

One of the most promising application areas for VLC is providing low-complexity connectivity for IoT devices and sensors, enabling them to communicate with each other and with a central hub for information collection and processing.

2.4. The Internet of Things (IoT)

The term Internet of Things (IoT) emerged in 2002. It describes an ambitious idea that extends the typical internet to connect more and more data-collecting devices. The aim of IoT in this scenario was mainly to eliminate the human factor, to automate mundane tasks and to avoid human errors. These devices are not just limited to computers and smartphones, but also include everyday appliances. IoT has found its applications in household, transportation, hospitals and health services, industry, entertainment and even environment monitoring [2], [76].

It is common nowadays to have up to hundreds of devices interconnected in one household. Aside from the regular personal computers, tablets and smartphones, household devices nowadays include smart fridges that monitor groceries status, smart coffee machines that prepare fresh coffee on time according to each user's preference, toothbrushes that count the number and length of dental cleaning

sessions and of course gaming consoles and smart surfaces. Thanks to smart sensors measuring humidity, temperature and plants vitality, garden sprinkles are automated to water the plants automatically as needed while saving water and energy [76].

In traffic and smart cities, vehicles such as self-driving, self-parking and hybrid cars, scooters, mopeds and trucks are equipped with smart sensors and communicating devices thanks to IoT. Even bulletin boards, streetlights and traffic lights are contributing to intelligent transportation networks, a product of the internet of things [76].

The IoT concept extended even to connecting devices that have very specific functions outside the household such as health monitoring sensors in hospitals [77]. It is common nowadays to find hospital rooms equipped with smart patient monitoring devices that track blood pressure, toxin levels, temperature, and other vitals and convey that information wirelessly and instantly to the doctors' tablets and smartphones. This way, the responsible doctors get instantly notified with the current status of their patients, potentially saving lives in the case where a time-sensitive reaction is required. In addition, IoT enables health professionals to track and monitor their patients not only in hospitals, but also in homes and everywhere they go [77]. Thanks to IoT, many countries were able to track the infection chains during the COVID-19 pandemic by providing a GDPR-approved tracking app installed on smartphones to prevent the wide-spread of the disease.

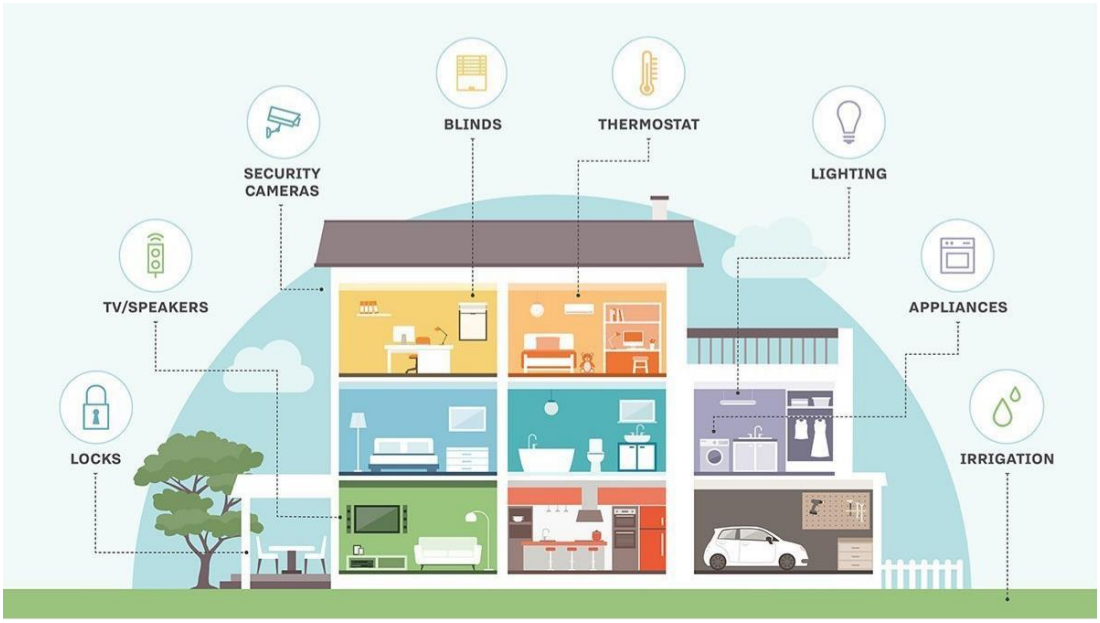

Figure 2-4: Illustration for the use of some IoT devices in residential environments [81]

IoT also has many applications in industry as well. Robotic arms, conveyor belts, smart robots handling packaging in logistic centres and machine-to-machine communication are a contemporary reality in factories [78]. Even in shopping malls and smart stores, IoT enables customer and product monitoring not only to prevent theft and automate the shopping and payment processes, but also to advertise for their products and to send location-based offers tailored to their customers preferences [79].

Last but not least, environment monitoring sensors simplify the accurate prediction of weather changes, hurricanes, storms and earthquakes, allowing people to prepare for them. Thereby, not only inconveniences but also injuries and potential deaths are avoided [80].

To summarise, the main concept behind IoT is to reach a truly wirelessly connected world, where every device is a wireless network node [1]. Figure 2-4 illustrates some examples of IoT applications in a contemporary home environment [81].

Ever since its introduction in 2002 by the British technology pioneer Kevin Ashton, IoT has been on a rising curve. In combination with artificial intelligence, machine and deep learning and the cloud technologies, IoT has been evolving rapidly and in many different directions ever since its birth. Cisco forecasts the IoT market to reach tens of billions of dollars and anticipates a demand for trillions of sensor units [82].

Because the IoT devices vary in size, energy requirements, location and functionality, it is a difficult task to find a suitable connectivity technology for all of them. IoT communication technology has very specific requirements: it must be energy and cost-efficient to be viable for mass production. It must also comply with the security and privacy measures to be trusted and adopted by the users. Because many of the IoT devices have small dimensions, the installed communication devices need to be of a small form factor [83].

Three connectivity types of IoT devices can be distinguished: short-range connectivity as entrance point to a wireless network, wide-area connectivity through cellular network, and long-range connectivity through satellites [1]. The majority of IoT devices are small in nature and require only the former connectivity type.

Connected IoT devices are stressing the spectrum of the radio frequency (RF) communication even further [4]. To solve the spectrum crunch problem, many researchers are working on non-traditional solutions by proposing smaller cell sizes where frequency reuse can be employed. It remains a challenge to find the appropriate low-power, low-complexity and low-cost communication technology to serve the needs of those small IoT devices without applying more pressure on the RF spectrum [1]. While Bluetooth, Wi-Fi and Zigbee are the typical solution in this scenario, they are prone to eavesdropping and cause interference with other

RF technologies if no further complex encoding, encryption and interference mitigation techniques are implemented. Cellular technologies were considered as another option, but their cost and licensing fees are out of the acceptable range for most typical IoT devices and sensors. Moreover, those technologies are not compatible with each other and therefore expensive converting devices are required for the users to manage all their IoT devices from a central hub.

2.5. VLC as Communication Technology for IoT

This gap in IoT connectivity provided a rich ground for the use of VLC as a complementary technology for RF for data exchange especially in indoor environments [1]. After all, VLC provides the low-energy consumption, low-cost, high privacy and security as well as ease of installation that is required by the small IoT devices. Besides, many IoT devices are already equipped with LEDs for illumination or status indication and some of them harvest light energy to be self-sufficient and autonomous communicating devices [84]. Having a device directly connected to the network as soon as it is exposed to light is a very attractive idea to many IoT manufacturers [1].

Many publications study the deployment of VLC in IoT. Katz and O'Brien proposed the concept of Living Surfaces (LS), claiming that the rooms, furniture and other objects people interact with everyday can be equipped with smart sensors and IoT devices for energy harvesting, wireless communication and environment sensing [1]. In their research, they envision a multitude of possible applications that depend on VLC in IoT including smart packaging, interactive logistics, patient management, advertisement and entertainment [1]. Philips Research in the Netherlands considered employing VLC for IoT devices for lighting control and device positioning in indoor offices. In their research, they have estimated the optical channel gains and implemented a VLC-based IoT solution which proved that VLC is a greener yet equally efficient type of communication for such scenarios [85]. LocalVLC, a low-cost VLC system that augments IoT services, was proposed by Haus, Ding and Ott with the aim of providing a more pleasant visual lighting experience to the user while employing off-the-shelf LEDs. Their proposed VLC system reaches distances up to 10 m with speeds reaching 1.4 kbps, enough to provide connectivity to typical IoT

sensing devices [86]. As connectivity technology for IoT devices, VLC did not stop at household level. Instead, it also found its applications in industry and specifically in warehouses. Novak, Dobesh and Wilfert proposed an artificial-reality-based system that employs VLC and IoT to optimise warehouse management. Through VLC transmitters and smart glasses or smartphones, data on stored articles could be exchanged with humans in an easy and low-cost way [87].

To manage IoT devices in a VLC network, Kim, Choi and Koh proposed an IoT device management protocol (IDMP) that offers device initialisation and data transfer management options. For the downlink, they employ VLC while ZigBee and Bluetooth are used for the uplink channel in their implemented protocol [88].

To conclude, VLC is considered a viable possibility for connectivity between IoT devices that require short distance, low-energy and cost-efficient communication.

To provide bidirectional VLC-based connectivity for IoT devices, the concept of LED-to-LED communications was proposed. It has the advantage of saving space, complexity and cost by employing the LED mounted on an IoT device as both a transmitter and a receiver. It reduces the cost of the system by replacing the photodetector (which costs up to hundreds of dollars) and upgrades the simplex channel of the VLC system to time-multiplexed half-duplex channel, halving thereby the total number of employed transceiver devices [29]. The system was first introduced by Dietz *et al*. [29] and adopted by Disney Research labs, Zurich, for toy-to-toy communication [30], [89]–[91]. It is the focus of this thesis to propose such a system as well as characterise and optimise it for IoT connectivity.

2.6. LED-to-LED Communication: State-of-the-Art

LED-to-LED communication offers a bidirectional VLC link without increasing the cost, complexity, space or energy requirements of the system.

The structure of a *p*-*n* junction allows the LED to sense an incoming beam of light at zero or reverse bias [92]. When a photon falls on the active area of the LED, its energy is absorbed by the electrons in the valence band. If this energy is larger than the energy gap, these electrons move to the conduction band and are free to move and to conduct current (i.e. photocurrent) [38]. Although the LED sensitivity is low compared to the PIN photodiode (due to the missing intrinsic layer), it can be employed as photodetector in simple low-data-rate, small-distance and low-cost applications [93].

An LED has been previously used as photosensor for ambient light by Dietz *et al.* [29] by making use of its junction capacitor. At the beginning of the photodetection bit, the LED capacitor is charged by reverse biasing it. It is then exposed to the incoming light source. In the presence of light, the charged capacitor loses its stored charge quickly because of the small photocurrent produced by the LED in response to the detected light. In case of no light, the majority of the charge remains stored on the LED capacitor. By measuring the remaining electric field at the end of the detection period, the amount of the detected light can be determined [29].

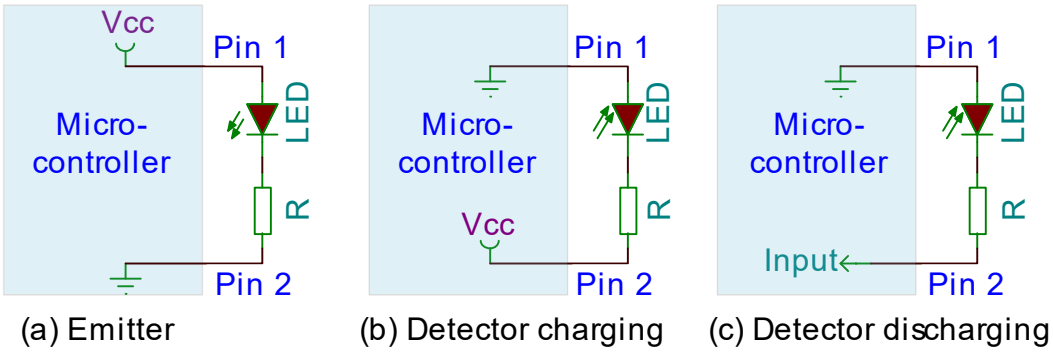

Figure 2-5: LED as transmitter and detector: microcontroller-based design by Dietz et.al [29]

The novelty of Dietz's paper is that it employs only 2 microcontroller pins for controlling the LED as seen in **Error! Reference source not found.**. When the anode of the LED is connected to the supply voltage (Vcc) and the cathode is connected to the ground pin via the series resistor R, the LED is forward biased and functions as emitter as depicted by **Error! Reference source not found.** (a). When the pin functions are switched as in **Error! Reference source not found.** (b), the internal capacitor of the LED is charged at the beginning of the detection bit. To be able to measure the amount of remaining charge on the LED's internal capacitor at the end of the detection bit time, Pin 2 is employed as high impedance measurement pin as seen in **Error! Reference source not found.** (c).

The advantage of using a microcontroller is that it is able to internally change the bias of the LED from forward (for light emission) to reverse (for internal capacitor charging) and then again to open circuit (for capacitance measurement) without any physical change to the LED pins connections. However, the data rate of detection is very low, and the overall speed of the system is limited by the microcontroller speed. Moreover, depending on the charging and discharging of a capacitor is a slow and inefficient way for using the LED as photodetector. In

addition, different off-the-shelf LEDs have different internal capacitances and the system is therefore not generic for all types of LEDs.

Stojanovic and Karadaglic employed the exact technique in their study to employ the LED as transmitter and receiver with the help of a single microcontroller in [94]. They also deducted that employing several LEDs for photodetection in parallel increases the sensitivity and enables the system to be employed for applications such as penetration and smoke detection.

Employing the same method as in [29], researchers from Disney Research Lab, Zurich, achieved a toy-to-toy communication channel based solely on LEDs for transmission and detection with 1 kbps data rate over small distances reaching 5 cm [90], [93]. Their system employs Manchester bit encoding to avoid the flickering of the LED being noticed by the human eye. On the physical level, they employed on-off-keying (OOK) as modulation technique. The system makes use of the software capabilities of the microcontroller to provide software-based synchronisation and locking between the transmitter and receiver devices [91]. However, the downside of basing the synchronisation entirely on software is that redundant bits are used for detection, which slows the speed of the system and lowers its throughput.

Schmid *et al.* improved the system by introducing simple VLC devices that turn the sound signals on the audio jack of computers, tablets and smartphones into light signals without the need for external batteries or microcontrollers. This enabled those devices to communicate with toys that are equipped with LEDs as photodetectors without increasing the cost or complexity of the communicating devices [95]. Although the proposed devices in their study depend on a PIN photodetector and not an LED, they offer a step closer towards enabling VLC

connectivity on smartphones and handheld devices and provide a means of communication with LED-enabled gadgets.

Due to the inconvenience of employing the LED as light-dependant capacitor, researchers turned their attention to studying the characteristics of the LED as a regular *p-n* junction photodetector. Miyazaki *et al*. investigated the wavelength selectivity of the LED photodetector. In their paper, they study the response and characteristics of a blue and a red LED and report that they show slightly shifted emission and extinction peaks, where the extinction peak wavelength is always lower than the emission wavelength. Their research claims that the LED can be employed as a wavelength-selective photodetector, eliminating thereby the requirement for using a filter at the receiver side. Moreover, the paper depicts that the blue LED response to incoming light is as low as 2.6 ns when it is reversed biased at 75 V [96]. Although that amount of reverse bias is not applicable in IoT device connectivity due to the limited battery power and potential, their study paved the way of investigating the LED as a photodetector for specific wavelengths and opened up the possibility of employing multi-coloured LEDs in wavelength division multiplexing (WDM).

Further investigations by Kowalczyk and Siuzdak characterised the LED as photodetector [33], [97]. They confirmed that the single-coloured LEDs can be used as photodetectors in addition to their main role as light emitters. Their research concludes that the responsivity of such single-coloured LEDs lies between 0.002 and 0.156 A/W depending on the type, manufacturer and colour of the LEDs and that the bandwidth of such LED photodetectors can be an order of magnitude higher than that of an LED emitter [33]. In addition, they investigate the photodetection capabilities of each LED colour and prove that the LEDs are capable of receiving wavelengths that are higher than what they are emitting. In

their paper they conclude that reverse biasing the LED to a certain point (dependant on the type of LED) increases both its bandwidth and sensitivity as a photodetector [97].

Based on the findings about the characteristics of the LED as photodetector, researchers proposed various LED-to-LED link designs. A 100 Mbps LED-to-LED communication system was designed by Kowalczyk *et al*. [31] and another design that reached 110 Mbps was proposed by Chun *et al*. [32]. Although the achieved data rates are high, they are only achieved through design optimisation of the receiver circuit and the careful choice of high-quality communication LEDs along with complex modulation and wavelength division multiplexing techniques. The proposed systems in [31] requires a complex modulation technique and complex equalizers in the detection phase. The system proposed in [32] is based on expensive and specially designed single-colour LEDs, as well as complicated optics and high processing power for achieving said data rates. Besides, they employ complex modulation techniques such as quadrature amplitude modulation orthogonal frequency division multiplexing (QAM-OFDM), that can only be generated using high-complexity processors and coding. This does not agree with the low-complexity nature of communication required by many IoT devices.

To the best of the author's knowledge, there are gaps in the field of LED-to-LED communication mentioned in literature that need to be fully filled before reaching the full potential of such a system. First, only single-coloured (mostly red and amber) LEDs are employed, although white light is best used for indoor illumination and VLC [98]. This is mainly due to the fact that white phosphorus LEDs fail to detect light power [34] because their phosphorus coating that is used to convert blue light into yellow light prevents incident photons from entering the

semiconductor die on the inside of the device. On the other hand, the RGB LED is an alternative, which is also capable of producing white light. That is why this thesis focuses on employing an RGB LED as transmitter and receiver.

Second, the published research does not consider lowering the cost and complexity of the system to comply with the mass production requirements of simple IoT devices. Instead, the main focus is on increasing the data rate and system performance despite the cost of employing complicated modulation and post-processing techniques. These systems further increase the expenses and the complexity by using expensive and specially designed optical lenses and concentrators [32]. To mitigate that problem, this thesis proposes a low-complexity driving and detection circuit and focuses on reducing the cost while satisfying the low-data-rate and low-throughput requirements for IoT communications.

Moreover, none of the presented systems test the LED-to-LED system in a bidirectional, time-division-multiplexing manner. Instead, they focus only on optimising the system performance of a unidirectional LED-to-LED link, ignoring the fact that a back-channel is also needed for a fully autonomous communication system. For that reason, this thesis characterises and implements a switching solution that allows a half-duplex LED-to-LED system employing an analogue switch.

In order to grasp how an LED-to-LED system functions with the aim of optimising it, the semiconductor principles behind light production and detection need to be investigated. The theory of operation of semiconductor-based photonic devices employed in VLC are therefore discussed in the following sections of this chapter.

2.7. Conclusion

Visible light communication has the potential of providing the large number of contemporary IoT devices with a low-complexity, reliable, space and energy saving connectivity without pressuring the overcrowded RF spectrum. Many researchers have already deployed and optimised VLC systems for such applications, benefitting from the various VLC advantages over Bluetooth, Wi-Fi, Zigbee and cellular networks. However, VLC still lacks the autonomy of other RF technologies due to its unidirectional and simplex channel nature. It is therefore the purpose of this thesis to propose a low-complexity LED-to-LED system for IoT devices that provides the low-data-rate, yet reliable and energy-efficient connectivity required.

Chapter 3

LED characterisation for an LED-to-LED System

3.1. Introduction

The LED is the main component in the LED-to-LED communication system since it has a double function of emitting and receiving the data-carrying light signals. Unfortunately, component manufacturers do not always reveal the most important features of the LEDs as emitter for VLC communications [99]. Such features include the output power linearity relative to the forward current, the spectrum and the noise generated by the LED. Even the most detailed LED datasheets fail to mention the characteristics of the LED as photodetector, leaving the researchers in the field of LED-to-LED communication depending on trial and error in their research [99]. Those features include the LED photodetector bandwidth, rise time, noise characteristics, responsivity and active area. It is therefore the aim of this chapter to characterise the LED as emitter and photodetector to employ it as transceiver in LED-to-LED communications.

3.2. The LED as Transmitter and Photodetector

Since an LED consists of a *p-n* junction, it is capable of both light production and light detection. Under forward bias, the LED operates as a light emitter while under reverse or zero bias, the LED's *p-n* junction can operate as a PN photodiode. Figure 3-1 shows the structure of the LED and its operation both as light emitter and light detector according to the external applied electric field.

Since LEDs are mainly manufactured and optimised for light emission and not for light detection, they are not as efficient as PIN photodiodes when operating as photodetectors. Firstly, they lack the high sensitivity and responsivity of the regular PIN photodiodes due to the missing intrinsic region. Secondly, LEDs have a much smaller active area compared to a regular PIN photodiode [33]. Some of the LEDs have in addition a packaging that does not allow incoming light beams to be focused on the active area of the LED, as opposed to commercial PIN photodiodes [33].

Last but not least, LEDs are made of semiconductor materials that are optimised for light emission, but that have limited wavelength bands as light detectors, making the LED a wavelength-selective photodetector [96].

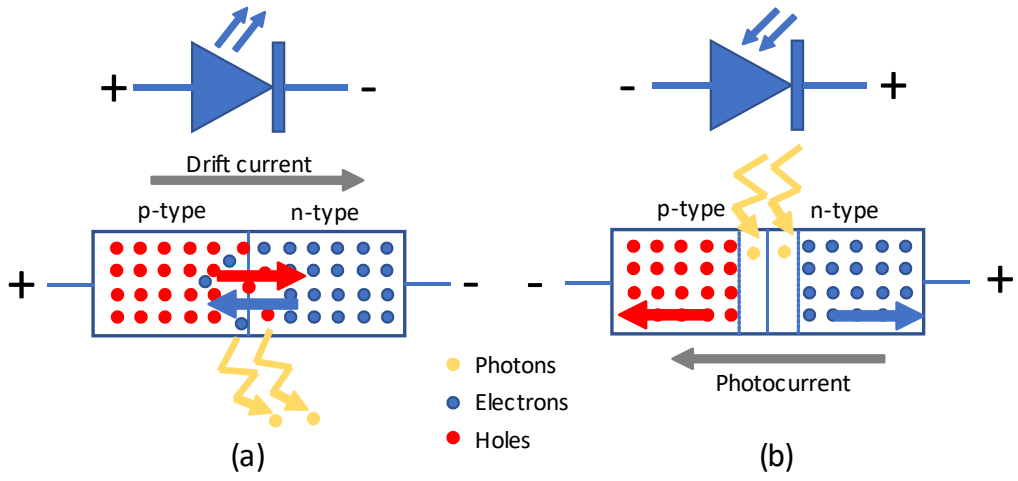

Figure 3-1: Operation of an LED in (a) forward bias as emitter and (b) reverse bias as photodetector

However, employing the LED as both a light emitter and light detector in the same VLC system has a lot of merits. In addition to saving space, cost and complexity by employing just one device as sender and receiver, the wavelength-selective property of the LED can be advantageous in applications requiring low complexity, yet wavelength division multiplexing to support a larger number of channels in parallel [100]. In addition, LEDs can operate as photodetectors at no bias, unlike PIN photodetectors that require a reverse bias to function. This is majorly advantageous in low-complexity applications that operate on a single low-voltage battery as power supply. In chapter 6 of this thesis, it is proven that LEDs are capable of detecting incoming light signals even when slightly forward biased. This gives them the potential of higher data rates since the switching time between transmission and reception can be decreased by not fully turning off the LED for reception.

The low sensitivity and low responsivity of the LED photodetector can be mitigated with the help of a suitable photodetector circuit providing a large gain factor as well as with a simple post-processing technique to increase the error-free transmission distance and data rate [31]. This thesis focuses on designing such a system to optimise the use of LEDs as both emitters and receivers.

3.3. Characteristics of the LED as Transmitter for VLC

In this section, the characteristics of an off-the-shelf RGB LED as emitter are investigated and experimentally derived. Both the linearity of the optical power emitted by the LED relative to the current feeding it and the spectrum of the RGB LED are experimentally determined.

The measurement setup depicted in Figure 3-2 is employed to measure the light power and spectrum of the RGB LED as transmitter. All the experiments are performed in a dark room. The RGB sub-LEDs are forward biased via a variable power supply to turn them on. At the receiving end - 3 cm away from the transmitter LED - a power and energy meter (Thorlabs PM200) captures the light emitted from the RGB LED while its forward current is varied. When the RGB sub-LEDs are fed with 20 mA of current, a spectrum analyser (Instrument Systems CAS140CT spectrometer with integrating sphere) is employed to capture the light and display its spectrum. For comparison purposes, the spectrum of a blue-phosphorus LED is also captured. The data from the spectrum analyser is used to determine the peak-wavelength for each sub-LED as well as its full width half maximum to determine the linewidth of each sub-LED [34].

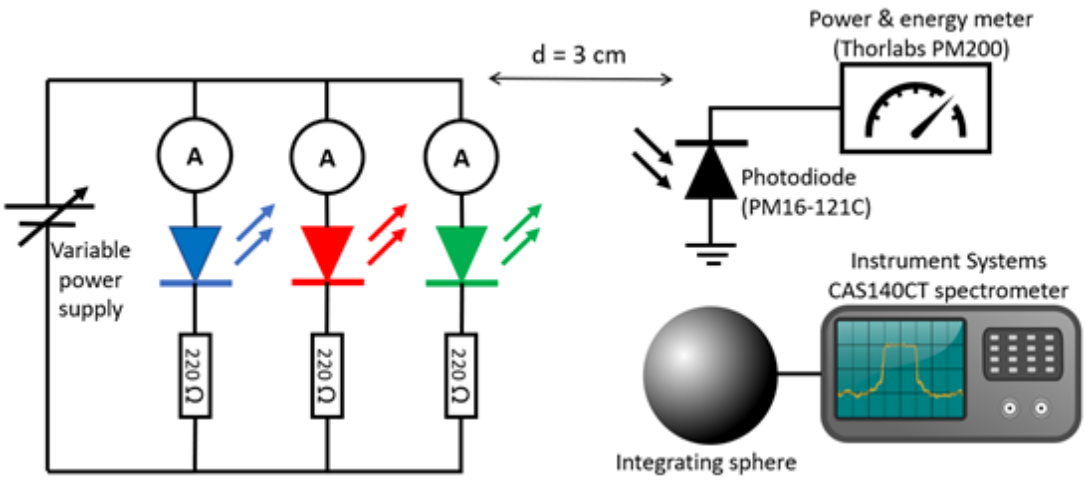

Figure 3-2: Block diagram of the measurement setup for testing the parameters of the LED transmitter [34]

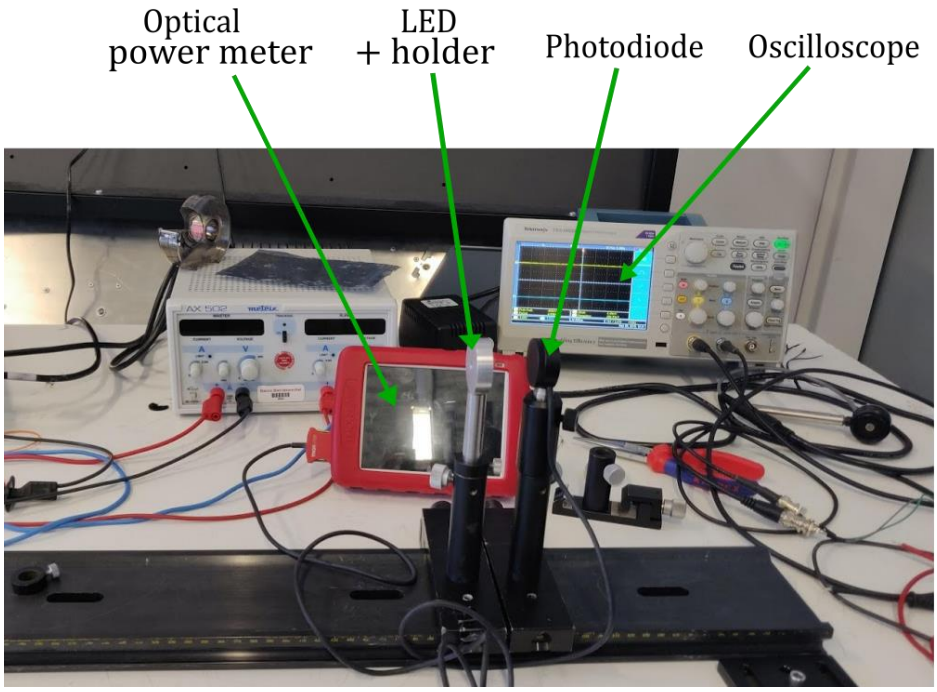

Figure 3-3: Experimental setup for measuring the LED optical power linearity

Figure 3-3 shows a photo of the experimental setup employed to measure the LED optical power linearity. A picture of the equipment used to practically measure the spectrum of the employed RGB LED and blue-phosphorus LED is shown in Figure 3-4.

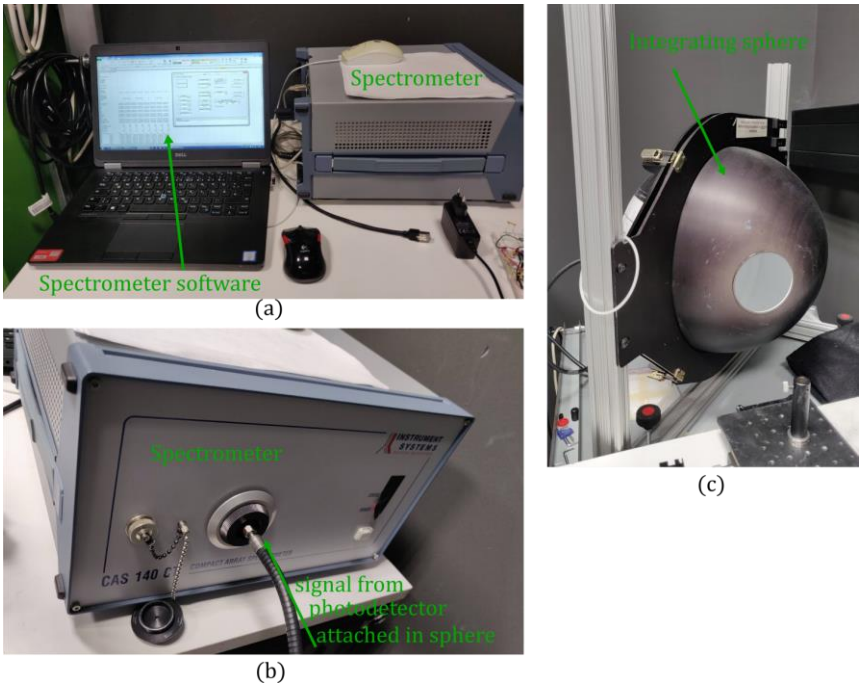

Figure 3-4: Spectrum measurement (a) spectrometer and software (b) spectrometer and connection to integrating sphere (c) spectrometer integrating sphere

3.3.1. Optical Power Linearity of the LED as Transmitter

Measuring the output optical power of each sub-LED at a constant forward current gives an indication which sub-LED is best suited as a light emitter: The higher the optical power at the same value of forward current, the brighter and more energy efficient the sub-LED is and hence the more favourable as emitter. As shown in Figure 3-5, the measured output optical power depicts that at every value of forward current, the blue LED has the highest intensity level, followed by the green LED. At 20 mA, the forward current recommended to drive the sub-LEDs, the blue, green and red sub-LEDs provide 0.8 mW, 0.45 mW and 0.17 mW of optical power, respectively. This indicates that the blue and green sub-LEDs would be more suitable as transmitters than the red sub-LED.

Moreover, the figure depicts the expected linearity of output optical power relative to the forward current for all three sub-LEDs. This is apparent in the nearly straight-line shape of the optical power graph indicating proportionality with the forward current. This is especially advantageous for the intensity modulation of the transmitter sub-LED.

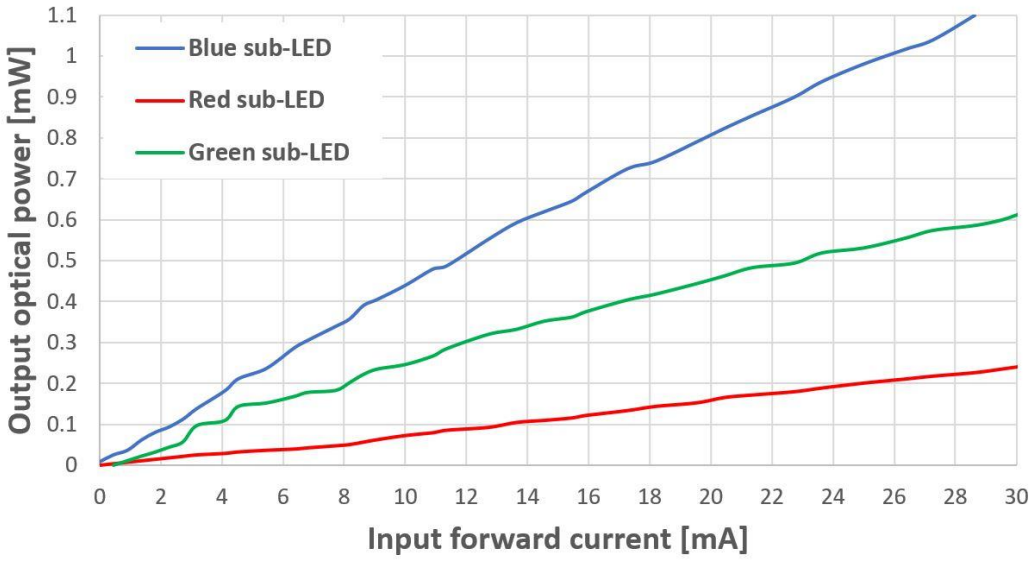

Figure 3-5: Output optical power of sub-LEDs at different forward current values [34]

3.3.2. Spectrum of an RGB LED Transmitter

The investigation of the spectrum of the RGB LED as transmitter (shown in Figure 3-6) provides three important parameters: Firstly, it shows the peak transmission wavelengths of the three colours which is an indication of their respective photons' energy. This parameter determines which LED is suitable for the detection of those photons at the receiver side. Secondly, the spectrum allows the calculation of the full-width-half-maximum (FWHM) of each sub-LED colour, indicating the linewidth of that sub-LED. This gives an indication of the bandwidth of the LED as emitter. Lastly, the amplitudes of the peaks should confirm the power measurement performed in the first experiment at a certain forward current – 20 mA in this case.

The measured and normalised spectrum of the RGB LED and the blue-phosphorus LED are shown in Figure 3-6 in solid and dotted lines, respectively. As expected, the RGB LED spectrum has three peaks with maxima at 465.27 nm, 515.66 nm and 629.77 nm for the blue, green and red sub-LEDs,

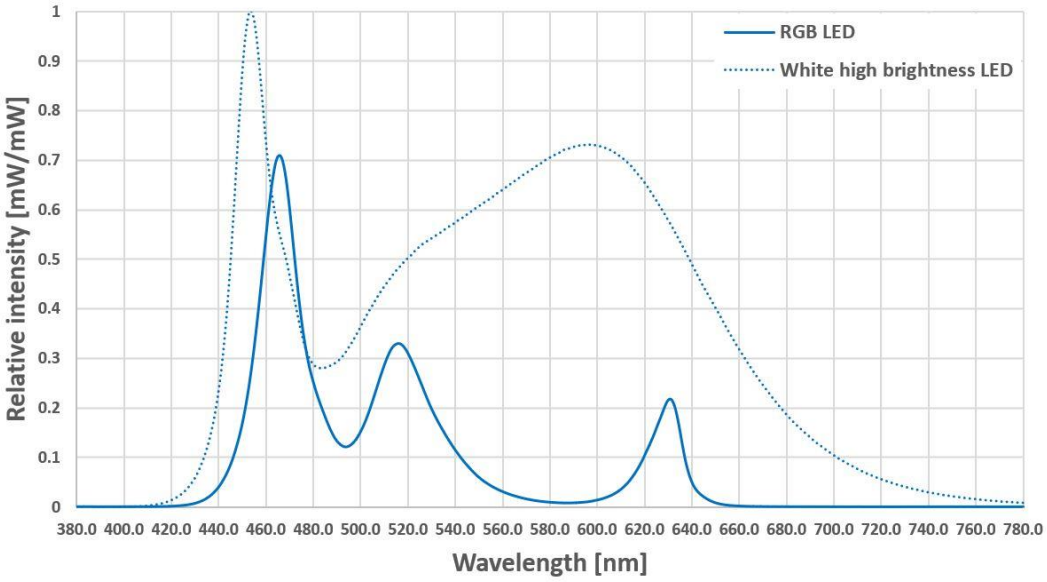

Figure 3-6: Normalised spectrum of the RGB LED in comparison with the spectrum of the blue-phosphorus LED [34]

respectively. The peak heights confirm the result of the previous experiment, showing that the blue sub-LED has the highest intensity followed by the green and red sub-LEDs with FWHM of 19.34 nm, 30.09 nm and 15.77 nm for blue, green and red, respectively. It is also seen from the figure that the FWHM of the blue-phosphorus LED is much wider than the RGB LED, which lowers the bandwidth of the system if employed as emitter.

From the peak wavelengths, the photon energy (which is equal to the energy gaps) for each sub-LED can be calculated according to equation **Error! Reference source not found.**:

$$E_{\text{photon}} = \frac{hc}{\lambda}. \tag{3.1}$$

They are found to be 1.969 eV, 2.404 eV and 2.665 eV for red, green and blue, respectively. This parameter gives another indication about the most suitable choice of sub-LED for photoemission and photoreception: Because the photons emitted by the red sub-LED cannot be detected either by the green or blue sub-LEDs, the red sub-LED is not optimum for photoemission. Instead, it is most suitable for photodetection since its bandgap is lower than the photon energy emitted by the green and the blue sub-LEDs. On the other hand, the green and blue sub-LEDs have higher photon energy and higher intensities, making them suitable as photoemitters but not as photodetectors.

Further experiments are presented in the section below to measure the responsivity of all three sub-LEDs to all three colours. This will help make a finite decision about the most suitable choice of sub-LED for photoemission and detection.

3.4. Characteristics of the LED Photodetector

The most important parameters of the LED as photodetector are devised through the experiments proposed in this section. Those parameters include the linearity, the responsivity, the effect of reverse bias, the 3-dB bandwidth, the angle of best reception, the FWHM of the LED acceptance cone, the produced noise and finally the response of the LED photodetector.

3.4.1. Responsivity and Linearity

The measurement setup depicted in Figure 3-7 is proposed to measure the responsivity of the sub-LEDs as photodetectors as well as the effect of the reverse bias on said responsivity. The RGB LED at the transmitter side is driven by a variable power supply to vary the forward current and hence the light intensity. Each sub-LED is turned on separately. At a 3 cm distance from the transmitter, an identical RGB LED is reverse biased via another variable power supply. To eliminate the receiver circuit effect on the bandwidth, no TIA is used on the receiver side. Instead, only a 1 MΩ resistor is connected in series to the

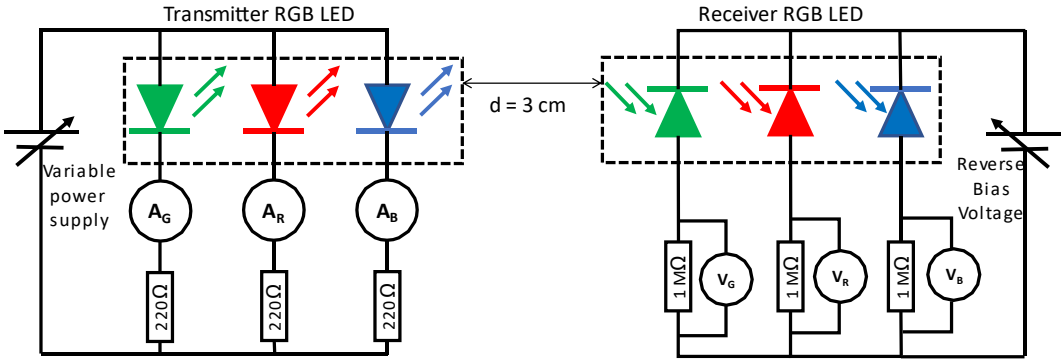

Figure 3-7: Block diagram of experimental setup to measure the responsivity of the RGB sub-LEDs

receiver sub-LEDs, on which the voltage is measured. The experiment is repeated 5 times, the results were then averaged.

The measured voltage is proportional to the produced photocurrent according to Ohm's law. The optical power that is reaching the receiver LED at each forward current can be deduced from Figure 3-8. The responsivity is calculated from the measured photocurrent according to equation:

$$R(\lambda) = \frac{I_{\mathrm{ph}}}{P_o}. \tag{3.2}$$

Figure 3-8 depicts the photocurrent induced by each of the sub-LEDs in response to incident optical power from the blue (solid line) and green (dotted line) transmitter LEDs, respectively. Three deductions can be made from the graph: Firstly, the produced photocurrent is proportional to the incident optical power for all sub-LEDs. This proportionality reflects the linearity of the LED as photodetector and indicates that the responsivity stays constant over the range of incident optical power between 0.1 and 1 mW. Secondly, the graphs' slopes represent the responsivity values for each sub-LED relative to the green and blue

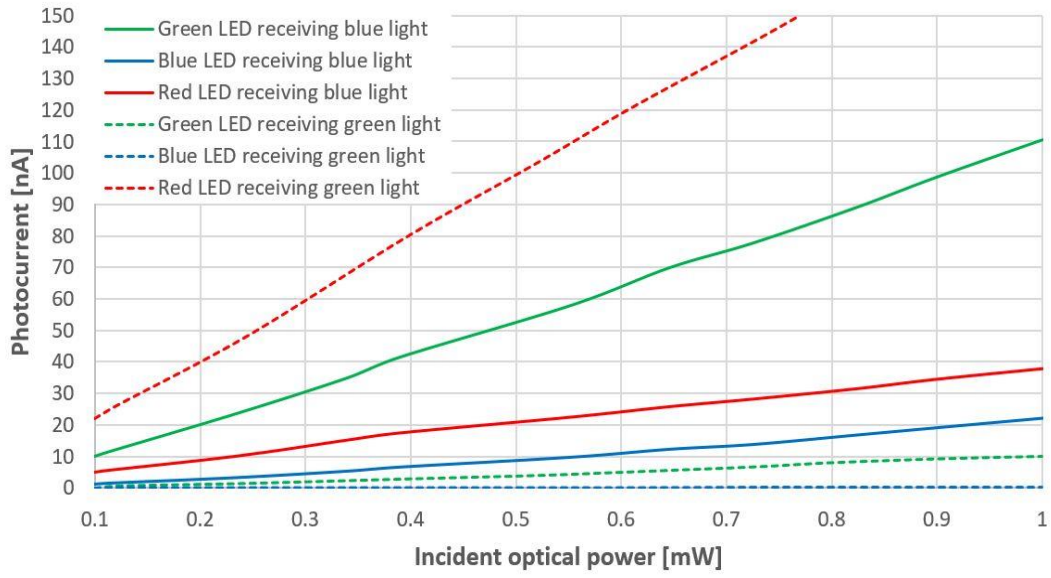

Figure 3-8: Response of the sub-LEDs to incident optical power at no bias [34]

light. It is obvious from those slopes that the responsivity of the red sub-LED is highest both when receiving blue and green light. On the other hand, the responsivities of the green and blue sub-LEDs are much lower. This indicates that those sub-LEDs are not optimal for photodetection. Thirdly, the figure shows that the sub-LEDs are capable of detecting light even under no bias. This is an advantage of the LED as photodetector over regular PIN photodiodes, which require reverse biasing for right photodetection. The graph does not show the response of the sub-LEDs to the emitted red light because all sub-LEDs fail to produce any photocurrent in response to red light. To validate that finding and make sure that it is not due to the low light intensity of the emitter LED, a LASER diode of the same peak wavelength but much higher emitted optical power replaces the emitter LED. Even with the higher optical power of the emitted red light, all three sub-LEDs show no response in terms of photocurrent.

Table 3-1 depicts the responsivity values of each sub-LED in response to the green and blue light at different reverse biases. The maximum reverse voltage before break-down of the LED photodetector is 25 V, hence only reverse biases up to that value are tested. It can be seen from the table that reverse biasing the green sub-LED does not have a major effect on its responsivity. On the other

Table 3-1: Responsivity of the sub-LEDs at different reverse biases in mA/W [34]

Detector	**Green transmitter**			**Blue transmitter**		
	Red	Green	Blue	Red	Green	Blue
V_R = 0 V	0.202	0.008	N/A	0.0424	0.1054	0.0173
V_R = 2 V	0.212	0.010	N/A	0.0436	0.1084	0.0143
V_R = 5 V	0.212	0.007	N/A	0.0426	0.1076	0.00945
V_R = 25 V	0.256	0.011	N/A	0.0675	0.1172	0.006

hand, the red sub-LED shows a relatively high increase in responsivity from 0.212 mA/W to 0.256 mA/W upon increasing the reverse bias from 5 V to 25 V. However, the responsivity stays almost constant between 0 and 5 V reverse bias. Similarly, the red sub-LED responsivity to blue light rises dramatically at 25 V in response to blue light, compared to the case with no bias.

The blue sub-LED shows the least responsivity to all light colours at all reverse bias values. It shows no response to green and red light. This is because the blue LED has a lower light wavelength and hence a larger energy gap than the energy of the green and red LEDs. Hence, the green and red photons cannot overcome the blue energy gap, nor can they stimulate electrons to move to the conduction band to produce photocurrent.

When exposed to blue light however, the blue LED could create some photocurrent, but its responsivity drops from 0.017 mA/W to 0.006 mA/W when its reverse bias increases from zero to 25 V. The increasing reverse bias widens the energy gap inside the blue sub-LED further, hence the photons that could overcome the energy gap at no bias are no more able to produce any photocurrent in the case of the increased energy gap.

In conclusion, this experiment shows that an LED can be used as a photodetector only when the energy of the incoming photons is larger than its own energy gap. For the RGB LED, this means that the red sub-LED is more suitable as a photodetector. Reverse biasing the red sub-LED beyond 5 V can increase its responsivity to both light colours. However, its responsivity shows no significant improvement by the slight increase of the reverse bias from zero to 5 V. This means that for the sake of IoT devices connectivity, the red sub-LED photodetector can work in the zero-bias mode, which reduces the switching time and the complexity of the LED-to-LED system.

3.4.2. Bandwidth of sub-LEDs

One of the most important factors of a photodetector is its bandwidth since it can limit the maximum data rate of the entire communication system. To measure the bandwidth of the sub-LEDs as photodetectors, a blue-phosphorus high brightness LED is employed as emitter to guarantee that the whole visible light spectrum is covered, and that the measurement is not wavelength-dependent. The proposed measurement setup for measuring the bandwidth of the LED photodetector is depicted in Figure 3-9.The blue-phosphorus LED is driven by a typical Bias-Tee LED driver that provides DC and AC current. The bias-Tee design has been chosen for this experiment instead of other LED driver topologies because of its ability to drive the LED at high frequencies. The AC signal is a 100 kHz square wave with 50% duty cycle and 5 V peak-to-peak amplitude. The RGB LED photodetector under test is placed co-axially at a 3 cm distance from the emitter LED while directly facing it. At this distance, the LED photodetector is not saturated and can still detect the light emitted from the transmitter.

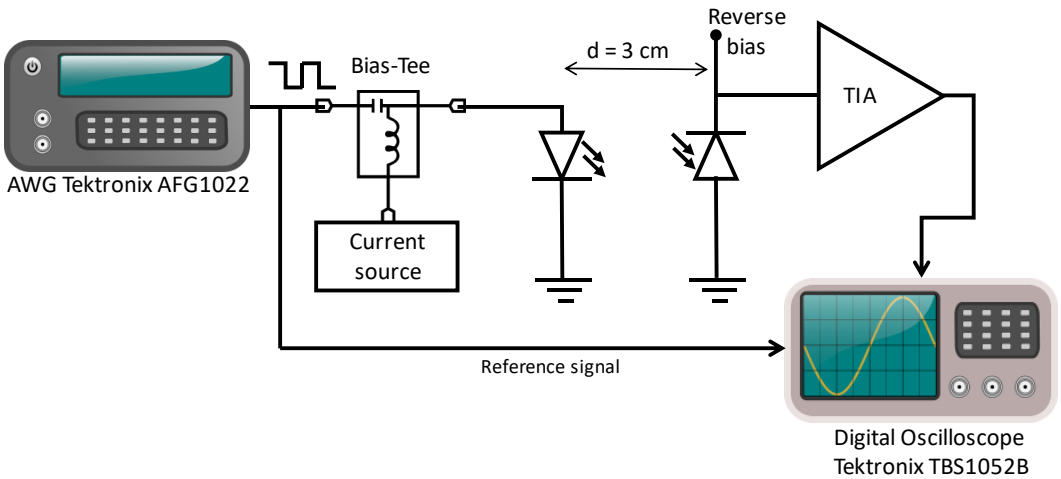

Figure 3-9: Block diagram of setup for measuring the bandwidth of the LED photodetector [34]

In this experiment it is imperative to employ a TIA at the output of the LED photodetector. This is because employing a large resistance in series with the LED photodetector (as in the previous experiment) will reduce the bandwidth significantly. The large resistance value multiplied by the internal capacitance of the LED would result in a large time constant that limits the overall bandwidth. Hence a large-bandwidth TIA circuit is employed to amplify the photocurrent and convert it to a measurable voltage signal without affecting the bandwidth. Both the output signal of the TIA as well as a reference signal from the function generator are stored for offline analysis, as shown in Figure 3-9.

The bandwidth is calculated by measuring the rise time t_r of the output signal. The rise time is defined as the time it takes the output signal to rise from 10% to 90% of the high steady state value. For a first order RC system, the bandwidth BW_{3dB} can then be estimated from the rise time according to the equation [101]:

$$BW_{3dB} = \frac{0.35}{t_r}. \tag{3.3}$$

Since the equivalent circuit for a photodiode resembles a first order RC circuit, equation (3.3) is a valid estimation for its bandwidth. The bandwidth measurement was performed for the red and green sub-LEDs and compared to that of a PIN photodiode at no bias, 25 V reverse bias as well as 2 V forward bias (when the LEDs are dimly lit). The bandwidth of the blue sub-LED was not measured due to its very low sensitivity and responsivity as photodetector. It is therefore eliminated as a photodetector option.

The captured waveforms along with the reference waveform from the function generator are displayed in Figure 3-10 when the red sub-LED is employed as photodetector. The graph shows that reverse biasing the red sub-LED increases improves the received signal quality in terms of bandwidth. Looking at Figure 3-10(c) it can be seen that the LED can detect light signals even when slightly forward biased, i.e. when dimly lit.

At 2 V forward bias, the depletion region of the red sub-LED has not yet entirely vanished and therefore, the weak detection of photons is still possible. This feature gives the LED photodetector an advantage over regular PIN photodiodes, which cannot detect any light under forward bias due to its intrinsic region. In addition, being able to detect light at no or even slight forward bias allows the fast transition between reception and emission modes.

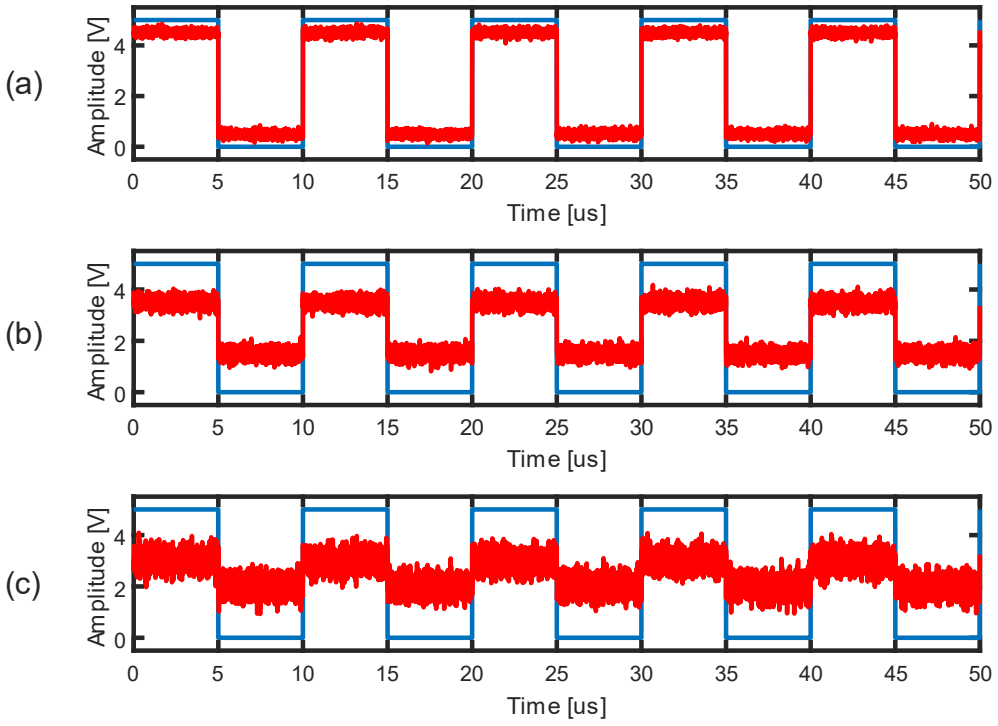

Figure 3-10: Captured waveforms at the output of the TIA drawn in red compared to the reference waveform from the function generator drawn in blue at (a) 25 V reverse bias, (b) no bias and (c) 2 V forward bias [34]

Table 3-2: Bandwidth of red and green sub-LED and PIN photodiode at different biases [34]

Bias	**0**	**-25 V**	**+2 V**
Red	2.4 MHz	4.9 MHz	0.8 MHz
Green	2.4 MHz	6 MHz	3.2 MHz
PIN	0.1 MHz	9.2 MHz	N/A

The bandwidths of the red and green sub-LEDs are compared to that of the PIN photodiode at different bias voltages in Table 3-2. The table confirms that, in addition to being able to receive at acceptable data rates at zero and reverse bias, the red and green sub-LEDs are able to detect light signals even when slightly forward biased. This is of great advantage in the design of the proper LED driver circuit since it allows the voltage swing between the “emitter” state and “detector” state to be minimal, increasing thereby the switching speed and the overall system maximum data rate.

While the LED photodetector has a lower responsivity and bandwidth compared to the PIN photodiode, it has higher bandwidth under zero bias and low reverse biases. This is why the LED can operate well in the photovoltaic mode, unlike a regular PIN diode.

3.4.3. Angle of Reception

This section aims to test the relative response of the LED photodetector at different angles of the received light. A small motor from a LEGO MINDSTORMS® EV3 set is programmed to rotate the attached RGB LED in 2 degrees intervals in front of a white light source. To guarantee that the RGB LED receives the same intensity at all rotation positions, a convex lens is placed at its focal distance from the white light source to collimate the light. A picture of the experimental setup is shown in Figure 3-11. The photocurrent produced by the sub-LEDs is amplified via a TIA and logged for each rotation position. For comparison, the experiment is repeated for a PIN photodetector with maximum sensitivity at a wavelength of 550 nm.

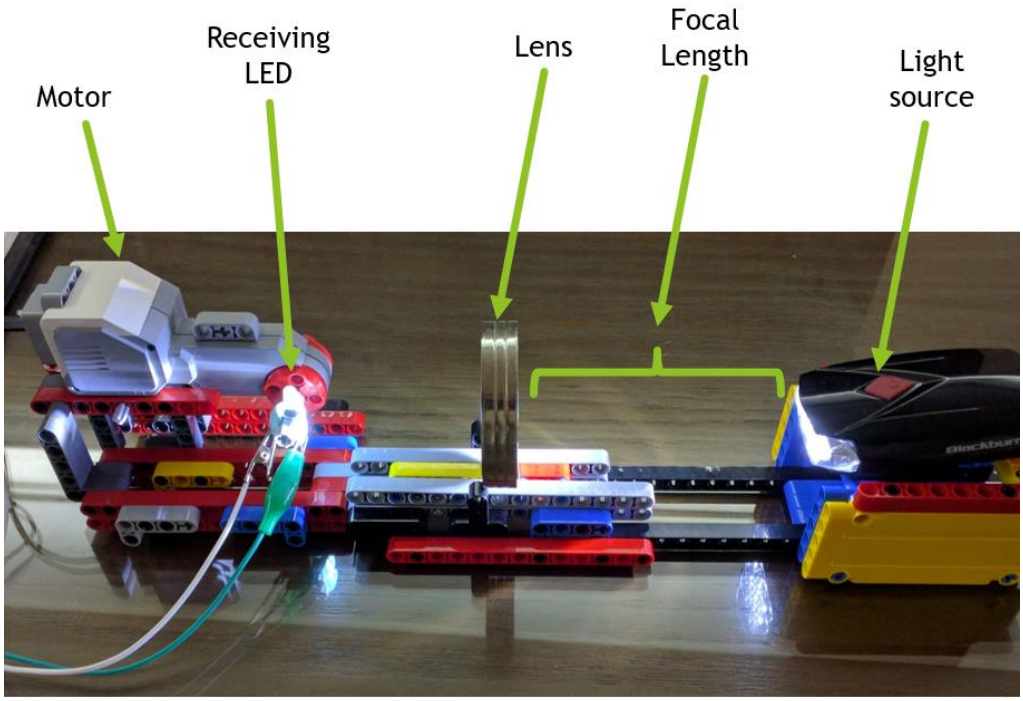

Figure 3-11: Experimental setup to measure the angle of reception of the LED photodetector

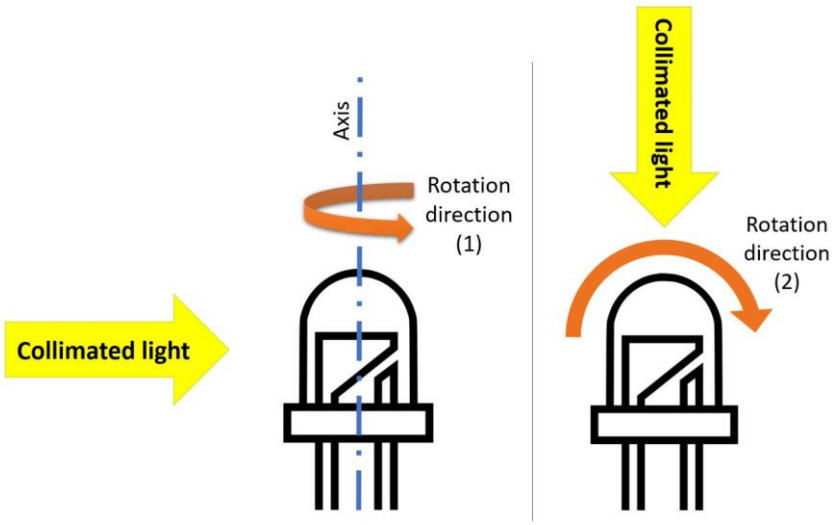

Figure 3-12: Rotation directions to test the relative response of the RGB LED to incoming light from different angles [34]

Two rotation directions were considered as shown in Figure 3-12: around and perpendicular to the LED's axis, respectively.

The results of these experiments indicate that the rotation of the LED around its own axis (Rotation direction (1)) has no effect on the produced photocurrent. The photocurrent fluctuates around a constant value at all angles of incident light. In rotation direction (2), however, the LED shows the highest response to incident light when it is directly facing the light source in a line-of-sight manner.

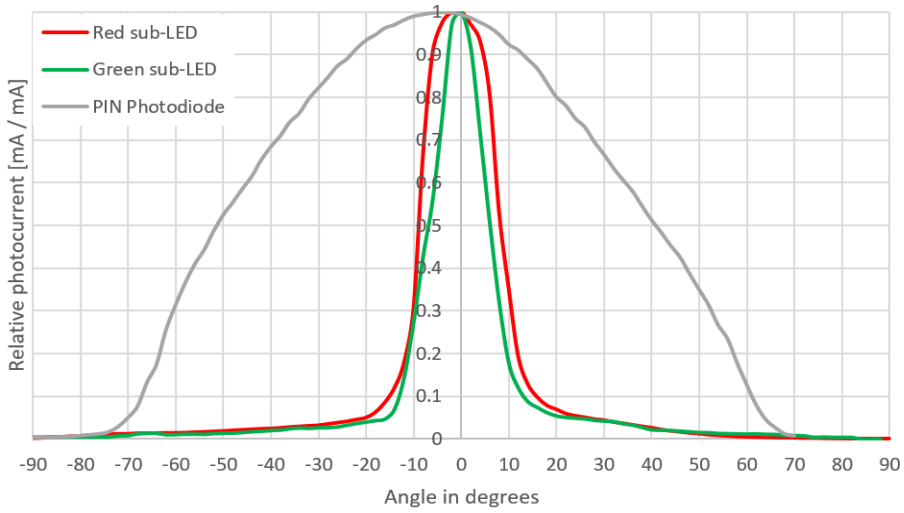

Figure 3-13: Normalised response of red and green sub-LEDs and PIN photodetector in response to incident light from different angles [34]

Figure 3-13 depicts the response of the green and red sub-LEDs and compares them to that of a PIN photodiode. The field of view of the photodetectors is calculated from the FWHM of the curves. It is found to be 18 degrees for the red sub-LED, 14 degrees for the green sub-LED, and 90 degrees for the PIN photodetector. It can be deduced from these results that the LED photodetector has a directive nature which can be advantages for applications such as indoor localisation.

3.4.4. Noise Measurement of red sub-LED Photodetector:

To the best of the author's knowledge, none of the researchers in the field considered analysing the noise produced by an LED photodetector. This is a significant parameter since the type and distribution of noise dictates the use of the appropriate techniques for optimising the system design. In order to analyse the noise of the red sub-LED photodetector, a DC signal is transmitted. The LED photodetector saturates at distances less than 3 cm, cropping thereby the noise signal. Hence, a correct measurement of the noise signal is only possible starting at 3 cm distance. In order to measure only the LED photodetector noise, no TIA is used to avoid the impact of the TIA noise. Instead, the photocurrent of the red sub-LED flows through a 2 MΩ resistor directly and the resulting voltage signal is captured on the oscilloscope. The impact of the noise on the received signal is shown in Figure 3-14. It can be seen from the figure that the expected DC output is contaminated by a noise of large amplitude. This is captured for offline analysis.

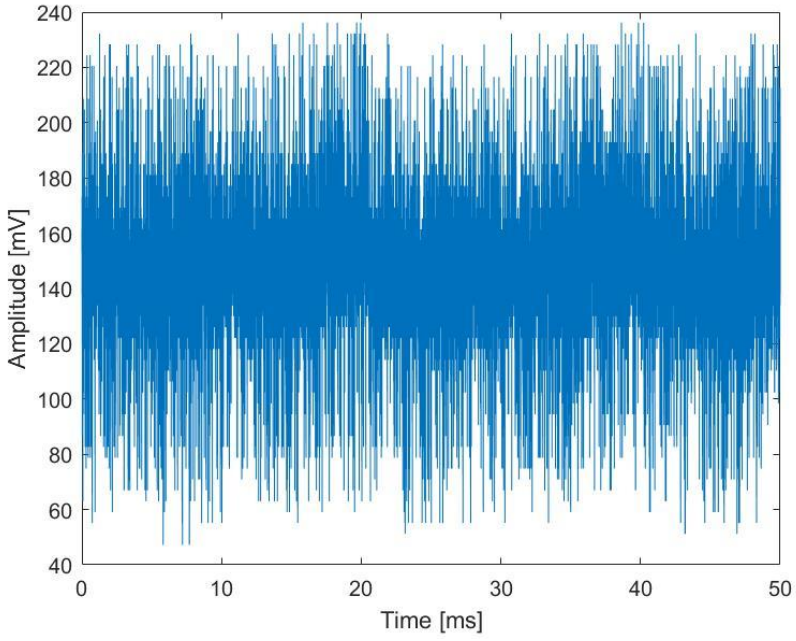

Figure 3-14: Captured noise signal from the red sub-LED upon receiving a DC light signal

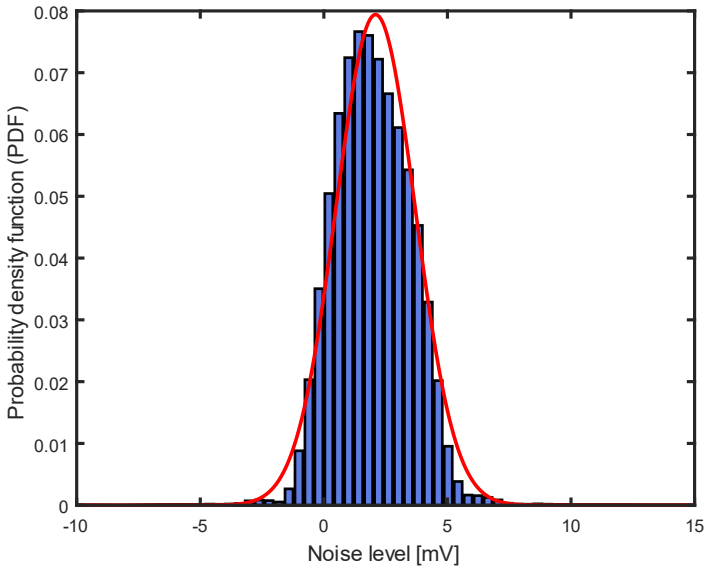

Figure 3-15: Histogram of the noise signal of the red sub-LED photodetector

First, the histogram of the noise signal is calculated and presented in Figure 3-15. This histogram shows the probability density function (PDF), i.e. the distribution of the noise-infected DC signal. Then, the DC component is subtracted, and the mean and standard deviation of the remaining noise signal are calculated. The PDF is compared to the most common statistical distribution functions. The R^2 factor is calculated as an indication of the correlation between the measured values and the values of the statistical functions and ranges from 0 (i.e. no correlation) to 1 (i.e. exact match). To determine the bandwidth of the noise signal and whether it is white or coloured, the FFT is performed.

The noise histogram in Figure 3-15 can be closely fitted to the Normal (Gaussian) function with zero mean and variance of 33.4 mW which is equal to the noise power. The variance and standard deviation vary with varying distance. The R^2 factor is calculated to be 0.9903 in this scenario, indicating a close match between the noise PDF and the Gaussian function. The performed FFT indicates that the noise is white, i.e. it has a flat frequency response over the entire

spectrum. Hence, the noise of the LED photodetector is defined to be zero-mean additive white gaussian noise (AWGN).

3.4.5. Response of LED as Photodetector:

The aim of this experiment is to deduce the response of the RGB LED as photodetector to incoming light at different energy levels and to relate the signal decay response to a well-known function.

In order to measure the decay of the signal with respect to the channel distance, the noise component is removed from the DC light signal sent from the transmitter LED along the transmission channel. The obtained energy levels at each distance are shown in Figure 3-16 depicted as a yellow line. The graph shows a significant drop up to a distance of 1 cm. This drop in energy along the distance is expected. It is important to relate the signal decay response using the LED photodetector

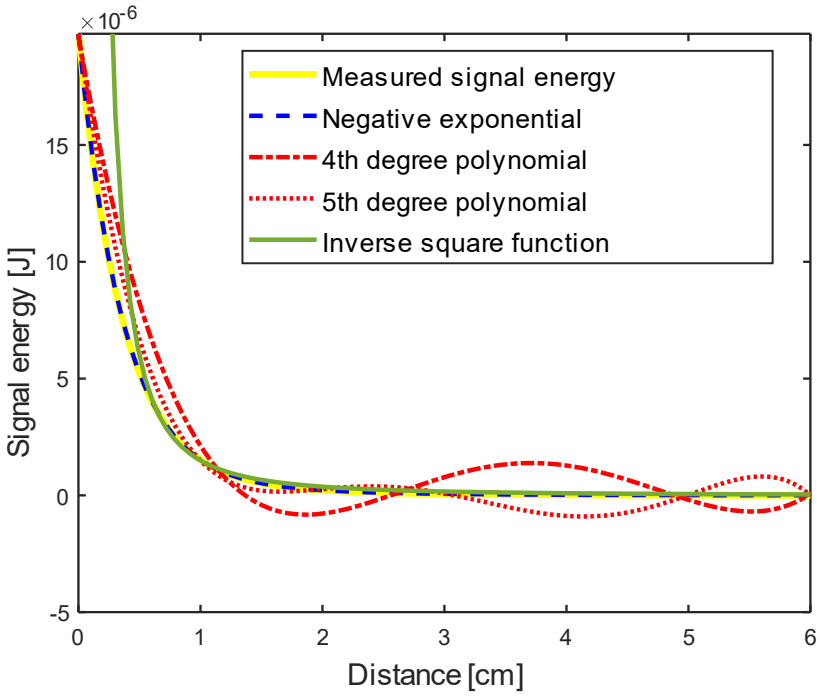

Figure 3-16: Response of the red sub-LED photodetector to incoming light at varying distance and its fitting to well-known functions

to a well-known function. The comparison of the measured energy levels with different functions (a negative exponential function, a 4th degree polynomial, a 5th degree polynomial and an inverse quadratic function) is shown in Figure 3-16. The figure proves that the LED photodetector can be described by the inverse square law of light ($1/d^2$) at distances longer than 0.5 cm [102]. It also shows that the measured signal overlaps with the negative exponential function. Therefore, the response can be best described as a two terms exponential function as follows:

$$E = 1.9 \times 10^{-5} \times e^{-2.8d} + 9.1 \times 10^{-7} \times e^{-0.89d}\,, \qquad (3.4)$$

where d is the transmission distance.

3.5. Conclusion

This chapter focuses on characterising the RGB LED both as emitter and photodetector with the aim of employing it as transceiver device in an LED-to-LED communication system. The chapter proposed a series of practical experiments to measure the linearity and intensity of the sub-LEDs in response to the forward current. The results of those experiments prove that the blue sub-LED has the highest intensity as emitter followed by the green sub-LED at every level of forward input current. Employing a spectrum analyser for calculating the energy of the photons emitted by each sub-LED and the FWHM of the sub-LEDs proved that the blue sub-LED has the smallest FWHM and the highest photon energy while the red sub-LED has the lowest bandgap energy.

Further experiments characterised the LED as photodetector. When testing the dependence of its bandwidth on the reverse bias and wavelength of incoming

light, the results of the experiments show that the red sub-LED has the highest responsivity when detecting green light, followed by the green sub-LED when the blue light falls onto it. Unlike the red and green LEDs, the blue sub-LED is unable to detect light due to its large energy gap. It is therefore not considered as photodetector in the LED-to-LED communication system. The responsivity of the sub-LED as photodetector increases slightly with increasing reverse bias. However, the most interesting feature of the LED as photodetector is its ability to detect light even when slightly forward biased.

The directivity of the LED as photodetector is measured and found to be 18 degrees for the red sub-LED, compared to 90 degrees for a regular PIN photodiode. This indicates that the LED can be employed for applications that require a low field of view and more directive photodetection.

The response and noise of the LED photodetector were also empirically characterised. The results of the experiments prove that the LED photodetector has AWGN characteristics and its response follows a two-term negative exponential function, matching it to the inverse square law of light.

In the next chapter, a transceiver module is designed to accommodate the LED as a transmitter and photodetector in a bidirectional LED-to-LED system.

Chapter 4

Transceiver Design for LED-to-LED Communication System

4.1. Introduction

The aim of this chapter is to introduce the proposed LED-to-LED system design and to characterise its components both through simulations and practical implementation. Firstly, the current-mirror-based transmitter is optimised to drive the LED at the needed forward current of 20 mA and with switching speeds up to 412 kHz. Secondly, the TIA-based receiver circuit is characterised and designed to accommodate the low sensitivity of the LED photodetector and to provide a transimpedance gain of 2 V/μA. Then the back-to-back signal performance is evaluated and optimised. Lastly, an analogue switching circuit is proposed and characterised with the aim of switching between transmission and reception mode without distorting the transmitted signals at a switching speed up to 710 Hz. This completes the bidirectional low-complexity LED-to-LED system proposed in this thesis.

4.2. System Design

Figure 4-1 shows a diagram of the proposed system inside an IoT device. The output data from the simple IoT processor is modulated and fed to the LED driver in the transmitter module. The main function of the LED driver circuit is to bias the LED at the right level and to modulate its forward current with the incoming data stream.

During transmission mode, the control signal from the IoT device processor to the signal routing and switching chip enables transmission and stops detection. The modulating current is then fed to the RGB LED through the signal routing and switching chip. In reception mode, the control signal enables the receiver and disables the transmitter circuits. In this case, the LED is turned to zero bias and acts as a photodetector. The small photocurrent that it generates upon receiving light is amplified by the transimpedance amplifier circuit, then demodulated in the receiver module. It is then filtered and decoded in the embedded processor.

The following sections design the modules of the proposed LED-to-LED communication device and evaluate their performance.

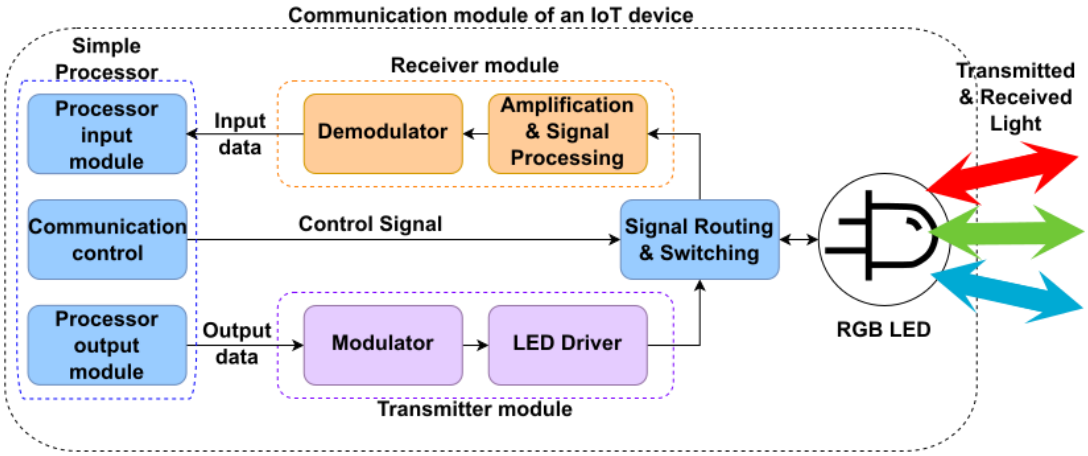

Figure 4-1: Diagram of proposed communication module for IoT devices based on LED-to-LED communication

4.3. Transmitter Design

The transmitter module main target is to drive the LED with the modulated forward current in response to the incoming data stream at the desired data rate.

The challenges facing the LED transmitter design are threefold: Firstly, the circuit should drive the LED with enough current to guarantee adequate brightness, taking into consideration that the output signal from the processor has a low voltage and can provide only limited current. Secondly, the LED should be switched on and off at a high speed (>100 Hz) to prevent the observer from noticing any flickering [38], [103] . Lastly, the design should be scalable to allow multiple LEDs to be driven in parallel (if needed) and to be easily combined with a detector circuit within the same device.

Typically, an LED driver circuit is based on a Bias-Tee solution. The Bias-Tee is a three-port network that combines a DC signal for biasing the LED on one input port and an AC signal for modulating the LED on the second input port. At the output port, the combined signals are fed to the LED. Figure 4-2 shows a typical Bias-Tee design employed as LED driver [104].

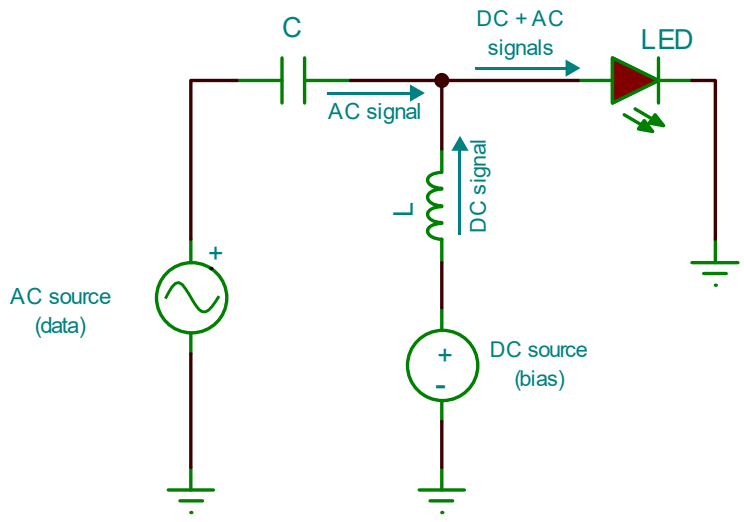

Figure 4-2: Bias-Tee based LED driver circuit

While this simple design is effective for modulating the LED at high data rates, it has two major setbacks: Firstly, the practically implemented Bias-Tee is based on imperfect coils and capacitors that have self-resonant frequencies and parasitic resistors causing undesired behaviour at certain frequencies. Hence, achieving a Bias-Tee design that works in a wide frequency range is not possible. It is therefore difficult to produce a Bias-Tee-based LED driver that works at the low frequency range required by typical IoT devices. Secondly, the Bias-Tee solution is not scalable for simultaneously driving multiple LEDs. If many LEDs are to be driven simultaneously, building a Bias-Tee network to drive each LED is space-wasting, expensive and cumbersome [105].

Because the LED is a current-controlled device, it should be driven by a current source. The current-mirror LED driver design depicted in Figure 4-3 is inspired by Burton's design published in [105]. It guarantees scalability - if many LEDs need to be driven simultaneously - and provides the required forward current and switching speed for the proposed LED-to-LED system. The three diodes D1 to D3 simulated at the output stage in the design represent the equivalent of a single LED. The forward voltage of a regular Silicon diode is about 0.75 V, while that of a green or blue LED is about 2.3 V according to the LED's datasheet. Hence, three diodes are placed in series to have an equivalent forward voltage as one LED.

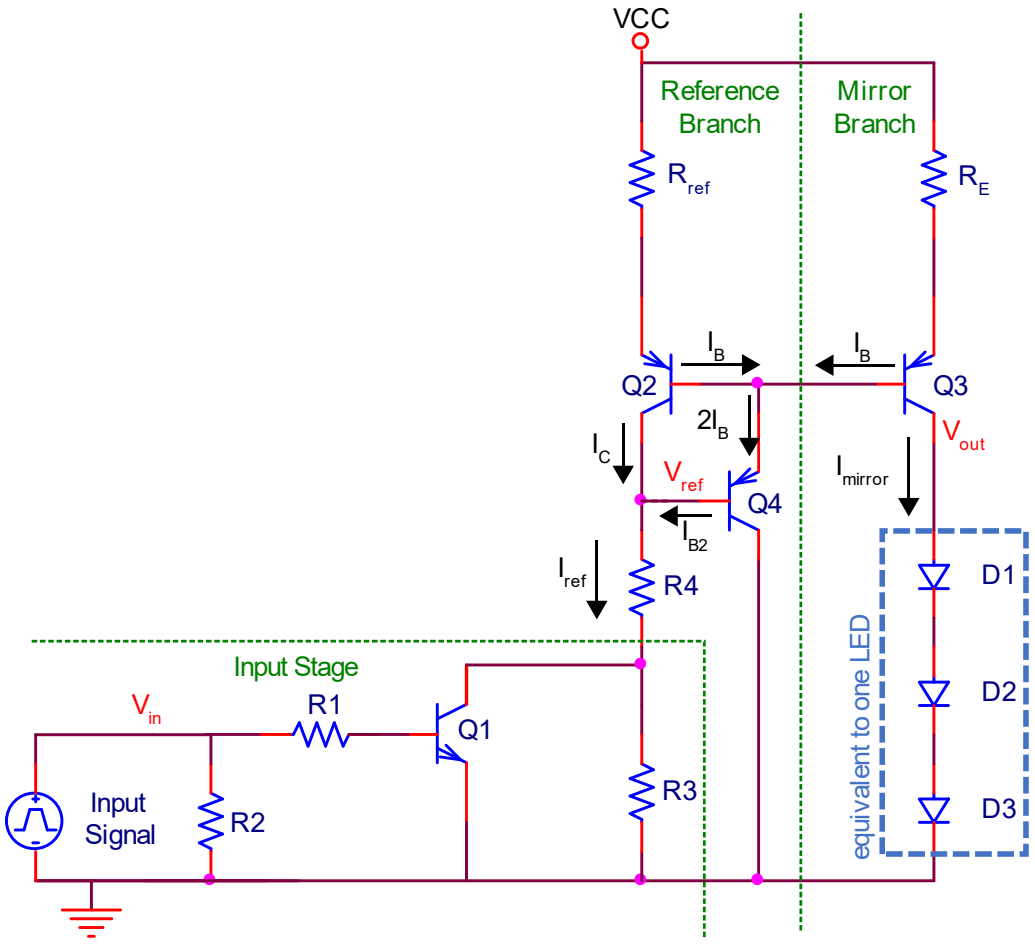

Figure 4-3: Current-mirror based driver circuit

The design is based on an emitter follower Beta Helper current mirror, made up of the three identical bipolar junction transistors (BJT) Q2, Q3 and Q4. Assuming R_E and R_{ref} have identical values, then the base currents for transistors Q2 and Q3 are identical and denoted as I_B in Figure 4-3.

According to Kirchhoff's current law, the emitter current of Q4 is therefore equal to $2I_B$. Hence, the base current of Q4 (denoted I_{B2}) can be written as follows:

$$I_{B2} = \frac{2I_B}{\beta}, \tag{4.1}$$

where β is the current amplification factor of each of the transistors Q2 through Q4. Similarly, the collector current of Q2 (which is identical to the mirror current feeding the LED) can be written in terms of the base current I_B as follows:

$$I_C = I_{\text{mirror}} = \beta I_B \,. \tag{4.2}$$

According to Kirchhoff's current law, the reference current flowing through R4 can be written as the sum of I_C and I_{B2} as follows:

$$I_{\text{ref}} = I_C + I_{B2} = I_{\text{mirror}} + I_{B2} \,. \tag{4.3}$$

By combining equations (4.1), (4.2) and (4.3), the mirror current I_{mirror} is related to the reference current I_{ref} according to the following equation:

$$I_{\text{ref}} = I_{\text{mirror}} + \frac{2I_B}{\beta} = I_{\text{mirror}} + \frac{2I_{mirror}}{\beta^2} \,. \tag{4.4}$$

Hence:

$$\frac{I_{\text{mirror}}}{I_{\text{ref}}} = \frac{\beta^2 + \beta}{\beta^2 + \beta + 2} \,. \tag{4.5}$$

Employing the described Beta Helper current mirror design ensures that the mirror current is very close in value to the reference current even for small β

values. Assuming a worst-case scenario for the β value of 10, the mirror current is 0.982 of the reference current according to equation (4.5). The current ratio tends to 1 with increasing β values, indicating more accurate mirroring of the reference current.

The ratio of the degeneration resistor R_E to the reference resistor R_{ref} determines the amplification factor of the mirror current relative to the reference current. This ratio can be set high to result in less power consumption of the whole circuit by keeping the wasted reference current low and the mirror current high. In the proposed design, the ratio is chosen to be 20:1, resulting in a mirror current that is 20 times larger than the reference current.

The resistor R4 controls the value of the reference current. The value of resistor R4 can be calculated by applying Kirchhoff's voltage law as follows:

$$Vcc - I_C \frac{\beta + 1}{\beta} R_{ref} - V_{EB}(Q2) - V_{EB}(Q4) - I_{ref} R4 - V_{EC_{sat}}(Q1) = 0\,, \quad (4.6)$$

where V_{EB} is the emitter-base voltage and $V_{EC_{sat}}$ is the emitter-collector voltage at saturation (which can be taken from the datasheet of the used transistor). For any bipolar junction transistor (BJT), the value of V_{EB} can be calculated as follows:

$$V_{EB} = V_T \ln\left(I_C / I_S\right)\,, \quad (4.7)$$

where V_T is the thermal voltage (around 25 mV at room temperature) and I_S is the reverse saturation current of the transistor.

With the reference current and the transistor parameters known, the value of R4 can be calculated by rearranging equation (4.6).

The input stage - consisting of the input signal source and transistor Q1 - acts as switch for the current mirror to modulate the output current with the OOK data.

When a logic bit ‘1’ is transmitted, the input signal is high which drives Q1 in saturation mode. This short circuits the R3 parallel resistor and allows a high I_{ref} to flow. When a logic bit ‘0’ is transmitted, the input signal is low which turns Q1 off. I_{ref} then flows through R3 instead of through the transistor, limiting therefore the reference current to just a few milliamperes. The resulting mirror current is therefore insufficient to turn the LED on, but also keeps it from completely turning off (which is the case at 0 A). This allows the switching time for the LED to be minimal, and increases thereby the data rate of the transmitter [105].

The main benefit of this driver circuit design is that it provides stability of the driven LED even with rising temperature. A voltage driver would have caused changes in the voltage level provided to the driven LED in response to changing temperatures. However, since this design is a current-based driver, the value of the provided current to the LED does not change in response to temperature changes, providing thereby much higher stability. In addition, the design allows for repeatability if multiple LEDs are to be driven at the same time. Once the mirroring branch (consisting of Q3, R_E and the attached LED) is repeated, the same amount of current is “mirrored” through all branches and all LEDs are modulated at the same intensity. Due to the resistor ratios, the circuit also saves energy, which is an important factor for IoT devices. Lastly, it consists of off-the-shelf BJT transistors that are cheaply available and fit the mass-production profile of IoT devices, allowing easy commercial deployment.

4.3.1. Performance Measurement of LED driver circuit

To measure the speed and bandwidth of the proposed LED driver circuit without the effect of the LED as transmitter, the LED driver circuit is both simulated and implemented without the LED at its output. Instead, a 10 Ω resistor replaces the LED to guarantee that it has no effect on the frequency response of the design. The current flowing through the collector of Q3 – which is supposed to flow through the LED transmitter – is measured to determine its amplitude and rise time.

The transient response of the driver circuit is simulated using the Texas Instrument TINA-TI® SPICE software and the results are shown in Figure 4-4. It can be seen from the figure that the forward current feeding the LED follows the input waveform: during the '0'-bit of the input voltage, the current is only 2 mA, hence, the LED is off. During the '1'-bit, the current rises to 19 mA, turning thereby the LED on. This concludes that the circuit acts correctly as a transconductance amplifier. It can also be seen from the figure that there is a current overshoot at the begin of the '1' bit, which puts a large amount of energy in a short time on the

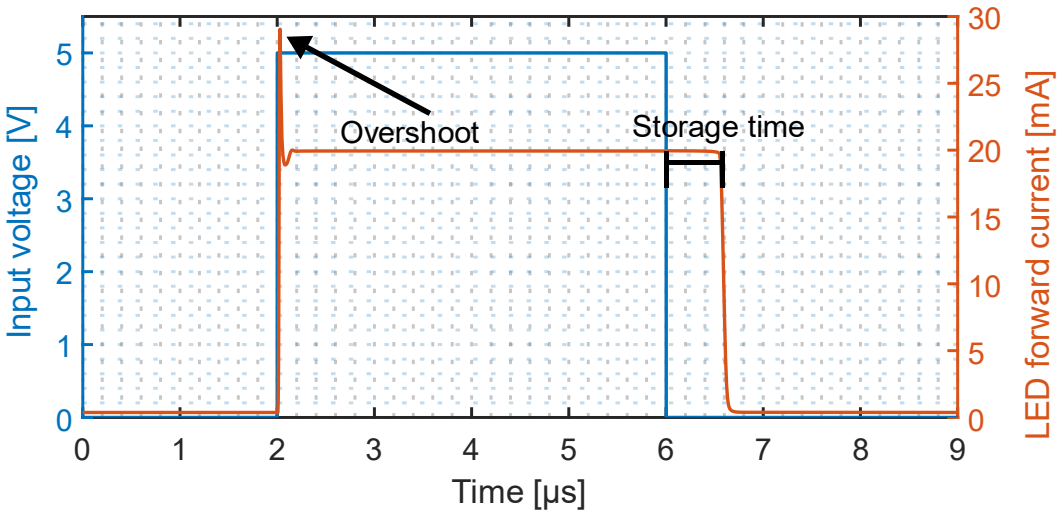

Figure 4-4: Simulation results of LED driver circuit

LED. This resembles an underdamped control system and is advantageous for the fast on-switching of the LED.

During the switching from the high to the low rail, the forward current lags the input voltage by around 400 ns, which is known as storage time. It is caused by residual charges stored in the device after switching off. Thereafter, the forward current curve decays exponentially to the low rail with a fall time t_f of 100 ns. Added up, this results in a total switching-off time t_{off} of 500 ns.

To practically measure the LED driver circuit response, the LED driver is practically implemented as shown in Figure 4-5. The current feeding the LED is measured on the oscilloscope using a current-to-voltage converter. From the measured waveform, t_{off} is measured to be around 960 ns, almost double the simulated results. This is mainly due to the intrinsic capacitors in the components which were not accounted for in the simulation. Although the long t_{off} accounts for almost 10% of the bit duration, it still allows for successful data transmission at the desired data rates. The forward current feeding the LED in the “on” state is practically measured as 18.5 mA, which corresponds to the simulated value. This

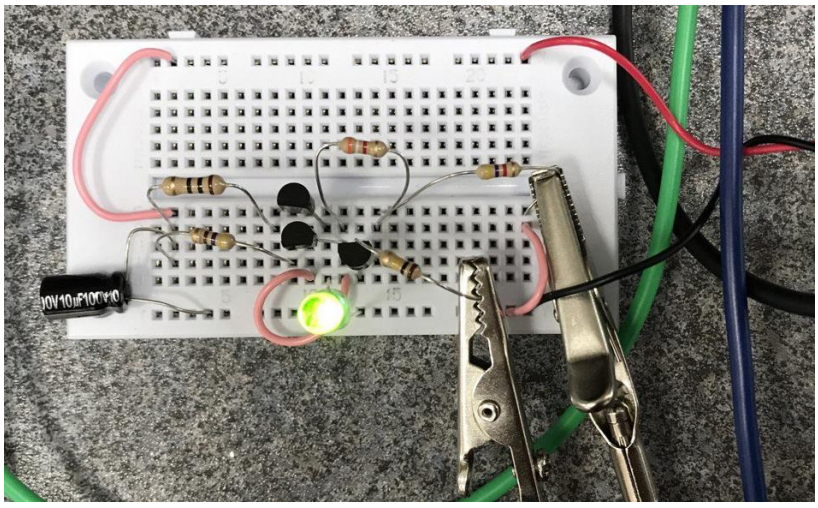

Figure 4-5: Implemented initial design of LED driver on breadboard

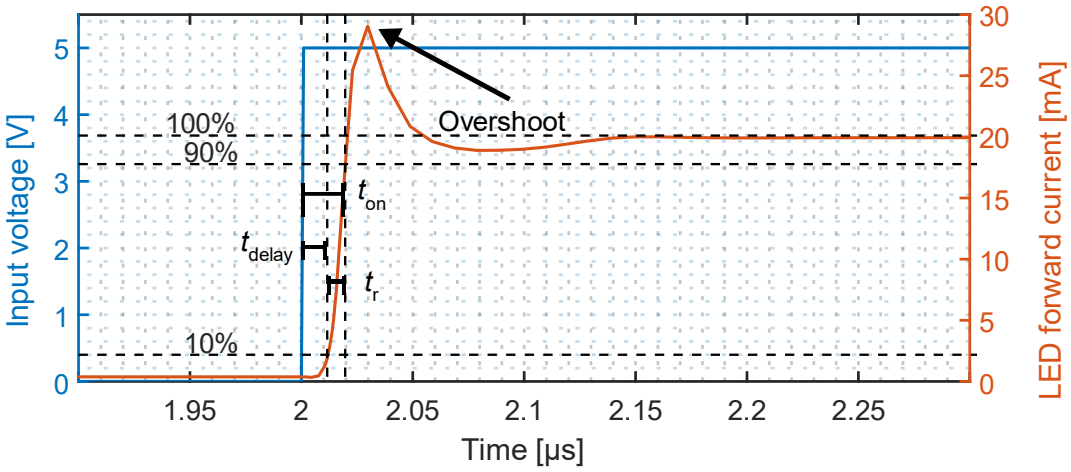

Figure 4-6: Behaviour of the simulated LED driver circuit at the rising edge

allows the LED to be brightly lit in the transmission mode. In the “off” state, the measured current is only 1.5 mA, which keeps the LED turned-off.

It is apparent from Figure 4-4 that the on-switching time t_{on} of the LED driver circuit is much shorter than the off-switching time. To measure it accurately, the circuit is simulated to work only between 1.9 µs to 2.3 µs to zoom in on the behaviour at the rising edge. The resulting waveform is shown in Figure 4-6. From the figure, the delay time t_{delay} and rise time t_{r} can be measured. The delay time is defined as the time from the transition point of the input signal to the time where the output has reached 10% of its high rail. The rise time is defined as the time it takes the output to rise from 10% to 90% of the high rail. The addition of the delay and rise time is the on-switching time. From the figure, the delay time is found to be 13 ns while the rise time is 9 ns, resulting together in an on-switching time t_{on} of 22 ns. The practical results confirmed the simulated rise time. The measured on-time is 25 ns.

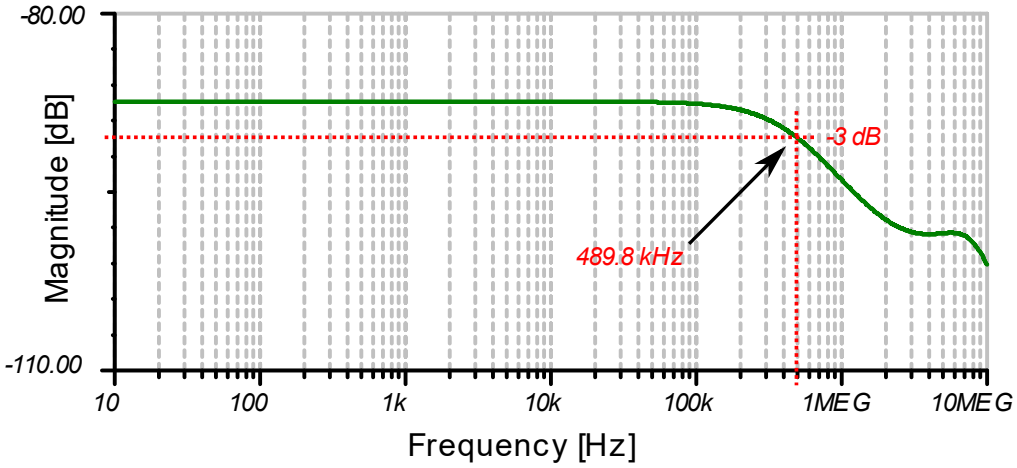

Figure 4-7: Simulated Bode plot of LED driver circuit

The frequency response of the circuit is depicted in Figure 4-7. The circuit has a flat response at low frequencies up to 450 kHz, which resembles the response of a low pass filter. The cut-off frequency is marked on the figure in red and is found to be 489.8 kHz. After that corner frequency, the curve decays with a slope of -30 dB / decade, revealing the existence of poles in the transfer function. At a frequency of 3 MHz, the effect of these poles is negated by a zero. However, the response at this high frequency is insignificant for the proposed system.

To confirm the simulated bandwidth, the 3-dB bandwidth BW_{3dB} of the circuit is practically determined from the measurement of the rise and fall time:

$$BW_{3dB} = \frac{0.35}{t_r}, \tag{4.8}$$

where t_r is the rise time (to be taken as t_f if larger) of the output square wave [106]. Equation (4.8) holds only for 1st order low-pass systems [106]. Since the bode plot of the proposed system resembles that of a first order low-pass filter, the equation can be employed as a rough estimate for the bandwidth. From the

measured fall time of 960 ns, the bandwidth is found to be 412 kHz, confirming thereby the simulated value.

4.3.2. Power Rating of LED driver circuit

The RGB LED operates at 20 mA forward current at a 5 V potential, which results in 100 mW. By reducing the forward current through the RGB LED, power consumption could be reduced on the expense of reducing the LED's brightness and hence the transmission range. However, these 100 mW are the worst-case scenario which considers the LED is to be on at all times. In reality however, the LED is expected to switch between on and off during transmission. Assuming the same probability of occurrence for the '0' and '1' bits, the power consumption is roughly half the 100 mW during transmission. Furthermore, the system can be programmed to turn the transmitter on only when data is sent. In systems where only infrequent data transfer is required, turning off the LED between the transmitted data chunks can save energy.

4.4. Photodetection Technique

Photodetection is the process of converting information-carrying light signals into their equivalent electrical signals for recovering the information. There are two types of photodetection techniques employed in VLC: Intensity modulation / direct detection (IM-DD) and coherent detection. While IM-DD is the simplest and most commonly used scheme, coherent detection allows the full recovery of the carrier information, i.e. the amplitude and phase [67].

In IM-DD, only the intensity of the light transmitted by the LED is varied according to the data. Hence, the detection associated with intensity modulation is an envelope detection and no oscillators are needed on the detector side for retrieving the information. The time-varying photodetector current $I_{\mathrm{ph}}(t)$ can be determined by transforming equation **Error! Reference source not found.** and is given by [67]:

$$I_{\mathrm{ph}}(t) = \frac{\eta e \lambda}{hc} M P_o(t)\,, \tag{4.9}$$

where t is the time, M is the current amplification factor of an APD to be taken unity in case of a PIN photodiode.

On the other hand, coherent detection is a much more complex detection technique that modulates not only the magnitude but also the phase and frequency of the optical carrier. At the receiving end, an optical local oscillator (usually a LASER), filters and electrical detectors are employed for the correct reception. Coherent detection is used in high-data-rates and complex optical systems [67]. For simple IoT devices however, it is important to choose a modulation technique that requires low processing power and is easy to deploy

commercially. Hence, IM-DD with NRZ OOK is employed as modulation technique for the proposed system.

4.5. Receiver Design

At the receiving end of the VLC system, typically a transimpedance amplifier (TIA) is employed to convert the photocurrent produced by the photodiode into an amplified equivalent voltage signal [38]. TIAs can have two configurations based on the application of the system: photovoltaic and photoconductive [107]. The simplest possible forms of both configurations with a single feedback resistor are shown in Figure 4-8.

In photovoltaic mode, the photodiode is under no bias. The main advantage of this configuration is that the dark current noise is minimum, and the precision of the device is high. However, the achieved speeds are limited [107]. Because regular PIN photodiodes need a reverse bias to operate properly, this configuration is only used for energy harvesting and specific high-precision and low-data rate applications. However, because LEDs can operate as photodetectors without reverse biasing, the photovoltaic mode is feasible for

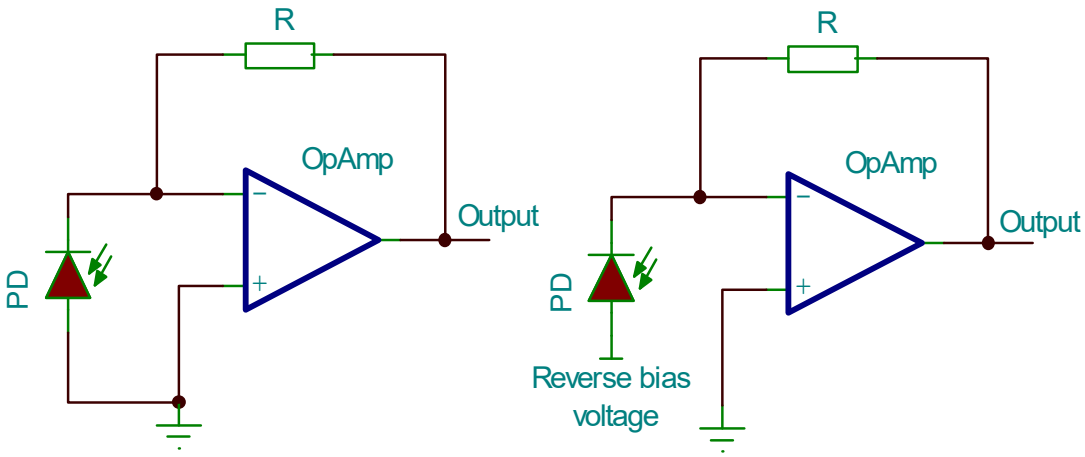

(a) Photovoltaic mode (b) Photoconductive mode

Figure 4-8: Configurations of TIA circuits

LED-to-LED communications. That is why this configuration is selected for the proposed system.

On the other hand, the photoconductive mode employs an external power supply to provide reverse bias for the photodiode. Although this configuration allows for higher data rates, it creates more dark current and a large noise component [107]. Besides, it employs an extra power supply to reverse bias the photodiode, which is not feasible in simple IoT devices relying on one battery.

The gain of the photodetector circuit is adjusted via the feedback resistor (denoted as R in the circuit diagram of Figure 4-9). However, the gain-bandwidth product GBW of the operational amplifier needs to be considered while adjusting the gain. According to Bode [108], the product of an amplifier gain and its bandwidth is a constant given by:

$$GBW = gain \times BW = \frac{g_m}{C}, \tag{4.10}$$

where g_m is the transconductance of the amplifying device and C is the combined capacitance seen by the amplifier. Hence, increasing the gain of the amplifier (by increasing the value of the feedback resistor) will decrease the bandwidth and thereby the data rate of the receiver circuit. The sweet spot providing enough gain to increase the sensitivity while not reducing the bandwidth below the threshold at which the receiver circuit is operating needs to be found for each application.

Since the sensitivity and responsivity of the LED as photodetector are expected to be much smaller than a photodiode, a detector circuit with high transimpedance gain is required to produce an output in the 5 V range in response to a photocurrent of only a few µA. While characterising the output current of the red sub- LED photodetector, it was found that it produces a photocurrent of 2 µA in response to green light from the transmitter LED in a back-to-back configuration. Hence, to meet the high rail of the OpAmp, a gain of 2 V/ µA is required. The TIA design should also have a minimum bandwidth of 200 kHz that allows a minimum data rate of 200 kbps using OOK. This is sufficient for the communication between simple IoT devices.

For the practical receiver design depicted in Figure 4-9, a high-precision and high-speed transimpedance amplifier integrated circuit (IC) (OPA380) is used. The gain of the TIA is adjusted to 2 V/µA by a 2 MΩ resistor in the feedback to mitigate the low responsivity of the LED photodetector. When a photocurrent I_{ph} is generated by the receiver LED, it flows from the cathode to the anode and ideally

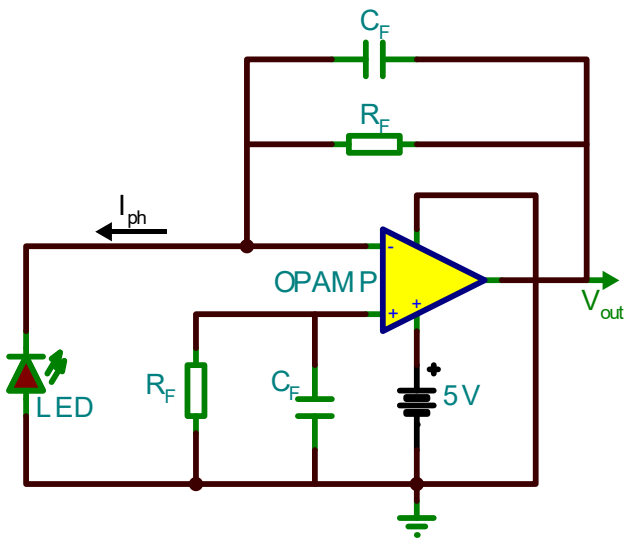

Figure 4-9: Transimpedance amplifier design for the receiver circuit [34]

only through the feedback resistor R_F. This results in a voltage drop V_{out} at the output given by:

$$V_{\mathrm{out}} = I_{\mathrm{ph}} \cdot R_F \,. \tag{4.11}$$

If the TIA feedback circuit consists only of the feedback resistor, the bandwidth of the circuit will be very large, allowing high-frequency ripples due to photodetection noise to pass to the output terminal [109]. The stability of the circuit is determined by the noise gain (NG), which is defined by the following equation [109]:

$$\mathrm{NG} = \frac{1 + sR_F(C_F + C_T)}{1 + C_F R_F}, \tag{4.12}$$

where C_T is the total capacitance on the inverting OpAmp terminal, consisting of the input capacitance of the OpAmp and the photodiode capacitance. From the equation of the noise gain, it is apparent that the transfer function has a zero at frequency f_z, which is given by:

$$f_z = \frac{1}{2\pi C_T R_F}. \tag{4.13}$$

To maintain stability and eliminate gain peaking, a feedback capacitor compensating the photodiode and input capacitances at the negative OpAmp input is needed. This creates a pole at the intersection of the noise gain and the OpAmp open loop gain curves and results in flattening the noise gain slope [109].

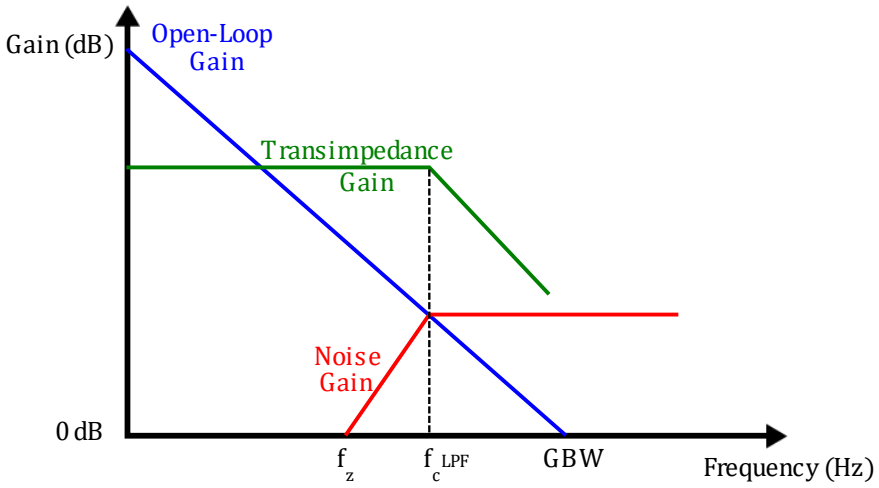

Figure 4-10: Noise gain, open-loop gain and transimpedance gain bode plot sketches upon connecting a feedback capacitor [109]

Hence, a feedback capacitance C_F is connected in parallel to the feedback resistor. Its main function is to create a low-pass filter (LPF) in combination with the feedback capacitor that has a cut-off frequency of $f_{c_{LPF}}$ as indicated by the following equation:

$$f_{c_{LPF}} = \frac{1}{2\pi C_F R_F}. \tag{4.14}$$

This increases the system stability and filters out the unwanted ripples due to the gain peaking [109]. Figure 4-10 shows the intersection of the noise gain plot with the open loop gain plot at the cut-off frequency of the LPF [109]. To theoretically calculate the value of the feedback capacitor C_F, the following equation is used:

$$C_F = \sqrt{\frac{C_T}{2\pi R_F (GBW)}}. \tag{4.15}$$

From the datasheet of the employed OpAmp (OPA380), the input capacitance is 1.1 pF and the gain bandwidth product (GBW) is 90 MHz. The LED photodiode

capacitance is measured using a capacitance meter and found to be 61 pF. According to equation (4.15), this results in a feedback capacitance value of 0.23 pF with a 2 MΩ feedback resistor. The closest practical value that is commercially available for the feedback capacitor is 0.47 pF.

The 3-dB bandwidth $f_{3\mathrm{dB}}$ of the complete photodetector circuit is then given by [109]:

$$f_{3\mathrm{dB}} = \sqrt{\frac{GBW}{2\pi C_T R_F}}. \tag{4.16}$$

For the chosen component values and GBW of 90 MHz, the 3-dB bandwidth is calculated to be 339.6 kHz. To confirm the theoretical performance results, the TIA circuit is simulated with the calculated component values and with the equivalent circuit of the LED as photodetector, as shown in Figure 4-11.

The feedback network is replicated from the positive terminal of the operational amplifier (OpAmp) to the ground to balance the total impedance seen by the

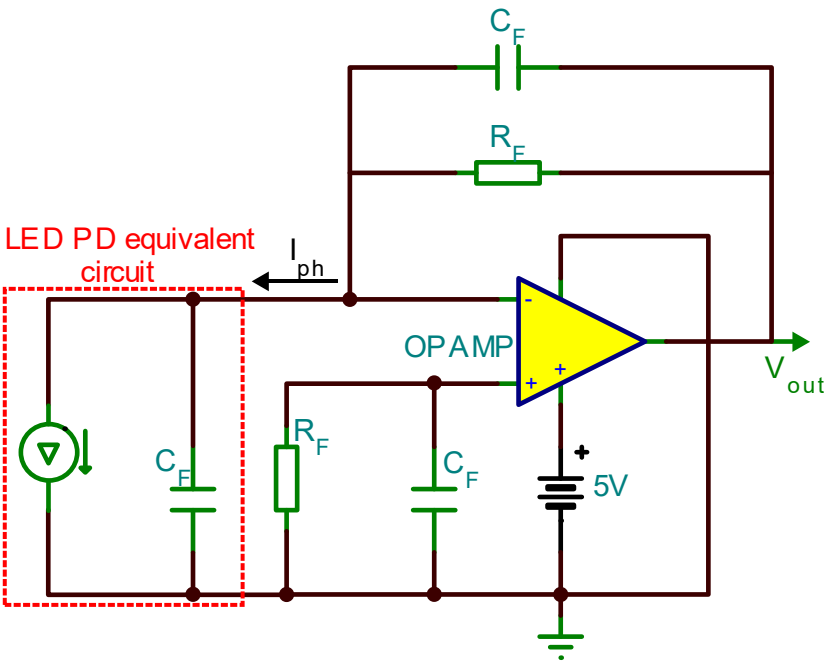

Figure 4-11: Simulated TIA circuit design with LED photodetector equivalent circuit

negative input terminal of the OpAmp. This symmetric design reduces the error due to the leakage current entering the non-ideal OpAmp.

4.5.1. Performance Measurement of receiver circuit

The bandwidth of the LED-based receiver circuit in Figure 4-11 is practically investigated to identify the data rate limitation of the OOK signal. The receiver circuit is simulated using the Texas Instruments® PSPICE software (TINA®) and its Bode plot is graphically displayed in Figure 4-12. The figure depicts that the response of the TIA receiver is similar to that of a low pass filter. The -3 dB point is marked on the figure in dashed red lines, suggesting a cut-off frequency at 334.4 kHz, which accurately mirrors the calculated value. The figure also reveals that there is a single pole at that corner frequency, causing a decaying slope of -20 dB / decade thereafter. The limited TIA bandwidth is considered the bottleneck of this system design and is mainly caused by the high value of the feedback resistor. To mitigate that problem, a two-stage amplifier circuit can be used. This approach is not adopted in this thesis to keep the bill-of-material and complexity of the system as low as possible.

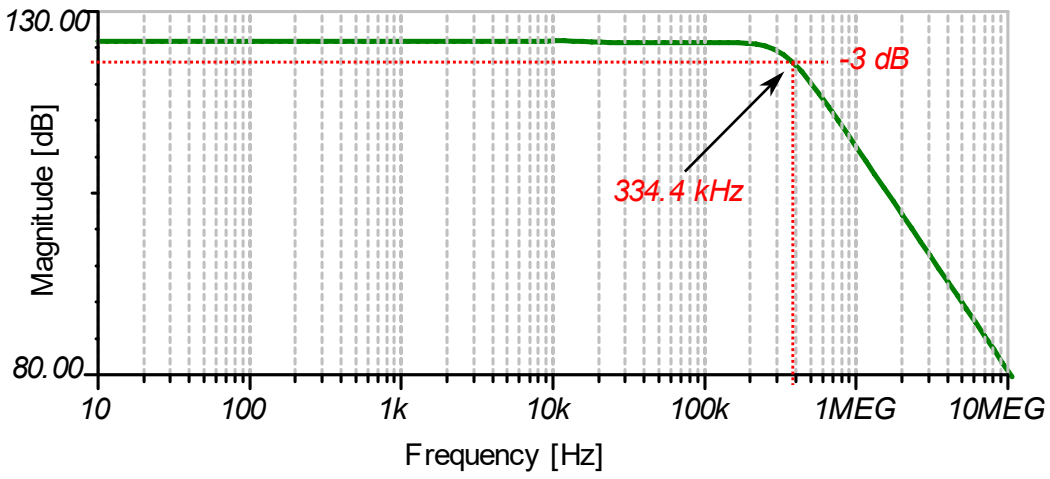

Figure 4-12: Simulated Bode plot of TIA-based receiver circuit

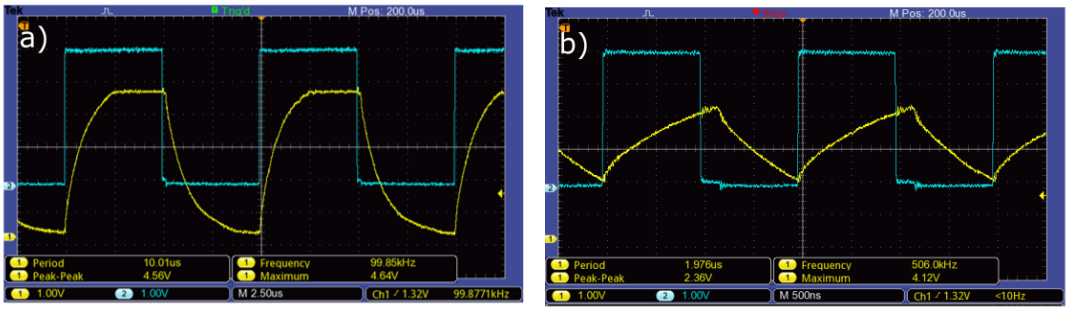

Figure 4-13: Transmitted signal (blue) and received signal (yellow) of the receiver circuit at (a) 100 kHz and (b) 500 kHz

To verify the simulated result practically, the waveforms in Figure 4-13 (a) and (b) are captured when a 100 kHz and 500 kHz square wave – shown in blue – are input to the TIA circuit, respectively. The rise time t_r of the output signal is measured from the captured waveform by the oscilloscope (calculated between 10% and 90% on the rising voltage edge) [101]. t_r is found to be 3.89 µs, which translates to a bandwidth BW_{3dB} of around 90 kHz. This agrees well with the simulated results for the bandwidth.

The waveforms in Figure 4-13 (b) show that at the data rate of 500 kHz the TIA OpAmp fails to saturate to the upper voltage rail, hence acting as an integrator and turning the received square wave close to a triangular shaped waveform. A 500 kHz data rate is therefore not possible for the proposed system as can be seen from Figure 4-13 (b).

From the simulation and practical measurements results, the system is capable of data rates up to roughly 100 kHz. This allows for data rates up to 200 kbps if a single-level modulation technique (such as NRZ OOK) is used. Hence, the overall system is tested only up to a speed of 200 kbps, which is sufficient for communication between small IoT devices.

4.6. System performance in a back-to-back configuration

To test the performance of the whole system without the effect of the LED as transmitter or as photodetector, the optical components are removed from the circuit and the transmitter and receiver circuits were directly connected in a back-to-back configuration.

Pictures of the designed and implemented transceiver printed circuit board (PCB) are shown in Figure 4-14. The PCB contains both the LED driver and the receiver module and has four hole-connections to attach the 4 pins of the RGB LED. The whole PCB has dimensions of just 3 cm x 3 cm.

The simulated circuit is shown in Figure 4-15. A 10 Ω resistor (R_{LED}) replaces the LED to avoid simulating the effect of the parasitic capacitance of the photoemitting device. Because the feeding current to the LED is much larger than the photocurrent generated by the LED as photodetector in response to incoming light signals, a current controlled current source with an amplification factor of 100 μ attenuates the output current of the transmitter circuit and inputs it to the TIA receiver.

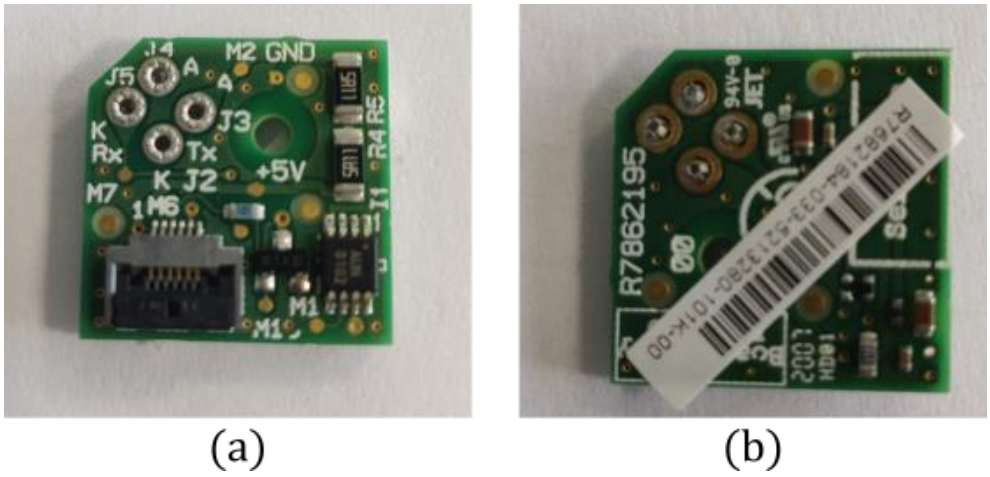

(a) (b)

Figure 4-14: Designed and implemented transceiver PCB (a) front (b) back layer

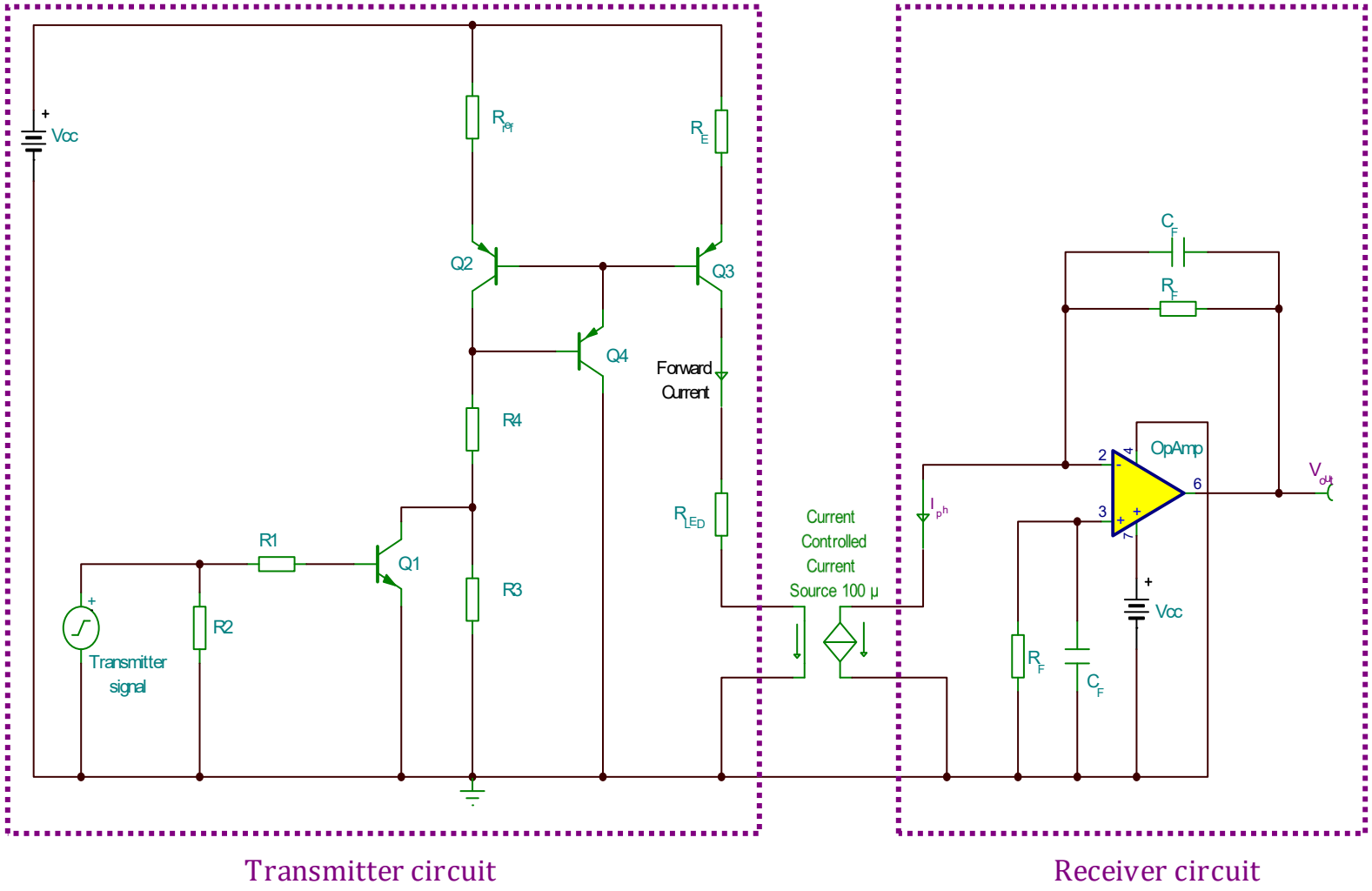

Figure 4-15: Test setup for simulating the back-to-back system without the LED

The simulated waveforms with an input square wave of 100 kHz and 300 kHz are shown in Figure 4-16 (a) and Figure 4-16 (b), respectively. It shows that the forward current and the receiver output both follow the square wave input for both data rates. However, in the 300 kHz case, the long storage time of the LED driver circuit propagates to the receiver and the output of the receiver fails to reach the low voltage rail for a period that resembles that of the transmitter. Hence, the output square-wave shaped signal has a duty cycle larger than 50%. This must be accounted for in the decision-making process at the decoding stage.

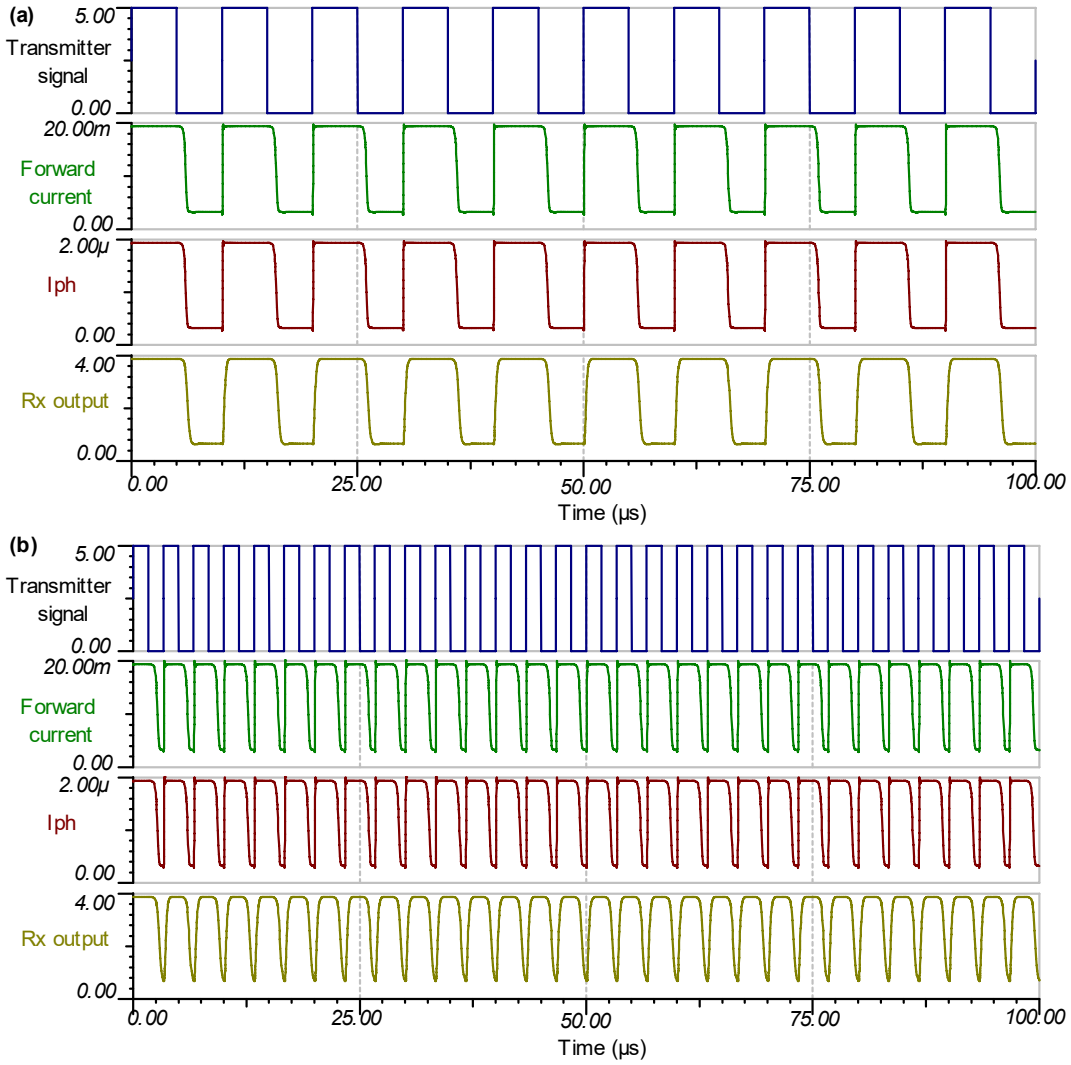

Figure 4-16: Simulated waveforms of transmitted signal, forward current to the transmitter LED, photocurrent generated by receiver LED and output of TIA at (a) 100 kHz and (b) 300 kHz

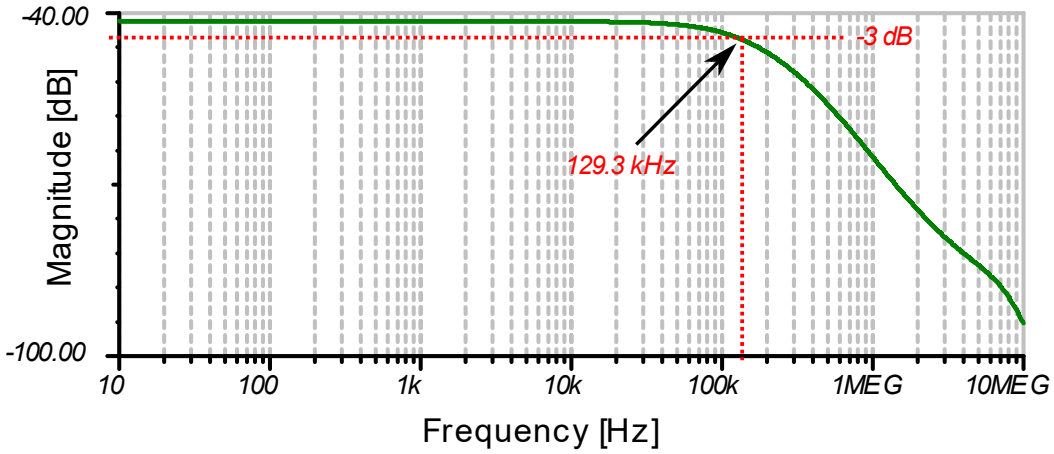

Figure 4-17: Simulated frequency response of the back-to-back electronic link

Figure 4-17 depicts the Bode magnitude plot of the complete electronic back-to-back link without the LED. For the AC simulation of the circuit, the current-controlled current source is configured as an ideal current attenuator in order for it not to affect the frequency response simulation. The Bode plot reveals that the system has a flat frequency response for frequencies up to around 100 kHz. It acts as a low pass filter with a 3 dB cut-off frequency at 129.3 kHz. A single pole of the system at that corner frequency results in a -20 dB / decade decaying slope after the corner frequency.

These results confirm the simulated and measured bandwidth results from the transmitter and receiver circuit. It is expected that the overall system bandwidth is as low as or lower than its parts, seeing that the transmitter and receiver circuits both have a frequency response similar to a low pass filter.

Since a practically implemented current attenuation circuit would affect the bandwidth measurement of the system and provide faulty results, the back-to-back system could not be practically tested without the transmitter and receiver LEDs.

4.7. Switching Between Transmission and Detection

The majority of the published research in the field of LED-to-LED communication focus on proving the feasibility of the communication channel and maximising its performance but consider only the LED-to-LED channel as a one-directional link. However, to benefit from the full capabilities of an LED-to-LED system, it is imperative to switch each LED between photoemission and photodetection mode. This switching has two functions: Firstly, to eliminate flicker so that the LED appears to a nearby human observer as being always turned on, and secondly, to achieve a half-duplex bidirectional channel instead of the broadcasting model achieved by the one-directional LED-to-LED link.

To achieve those two goals, the same LED has to be connected with the LED driver circuit in transmission mode as well as with the TIA circuit in detection mode. Then it needs to be switched between both modes in a time-division-multiplexing manner. The switching between transmission and detection mode has to happen at data rates high enough to prevent flickering from being noticed by a human observer. Hence, the switching frequency f_{switch} must be at least 100 Hz. However, f_{switch} must be low enough to allow for the successful error-free transmission of adequate data chunks during the “on” state of the transmitter.

In their paper, Giustiniano, Tippenhauer and Mangold have divided the frequency spectrum of low-data rate VLC into three regions with respect to flicker control [89]: The visual feedback region denotes the low-pass component of the spectrum which is observed by humans. In this region, small variations of the light intensity are tolerated by the human eye thanks to its low dynamic range [89].

The flicker region on the other hand is noticeable by the human eye and lies below 100 Hz [103]. This region should be avoided by communication over visible

light. Unfortunately, in the case of LED-to-LED communication, the system can reach this region by mistake in two cases: inter-message or intra-message flickering. In inter-message flickering, the LED is turned off for a long while in order to receive the data from the transmitter LED. On the other hand, intra-message flickering occurs when the LED is transmitting a message with a long array of subsequent ‘1’ or subsequent ‘0’ bits. This region can be avoided either by using a line coding technique such as Manchester coding or by reducing the bit duration to reach a data rate not anymore noticeable by the human eye [89].

The third region is the LED-to-LED data region, which lies in the higher frequency range [89]. In this region, the actual message is transmitted without the human observer noticing any flickering thanks to the slow response of the human nerve system connected to the human eye [103].

Many attempts to create a bidirectional LED-to-LED channel are mentioned in literature. Dietz *et al.*, Guistiniano *et al.* and Schmid *et al.* employed the pins of the microcontroller to switch between transmission and detection modes [29], [30], [89]. In their proposed systems, they employ only a single LED connected to two pins of the microcontroller. In transmission mode, the pin connected to the anode is configured as a digital output pin to convey the modulated data to the LED while the pin connected to the cathode is configured as ground. In the photodetection phase, the pin connected to the anode provides the reverse bias while that connected to the cathode is employed as input pin with analogue-to-digital conversion capabilities to read the data received by the LED [29], [30], [89]. However, because they only attempt to achieve very low data rates of transmission and reception with a maximum of 1 kbps, it is sufficient to implement the switch using only the two pins of the microcontroller. This method is not sufficient in the case of the proposed system in this thesis, where the transmitter

circuit is based on a current-mirror LED driver and the receiver circuit is based on an OpAmp TIA.

The authors of [110] and [111] employed analogue switching integrated circuits (IC) to create a bidirectional LED-to-LED channel. Although their idea is feasible, their research provides only inconclusive results and fails to consider the impact of the switching mechanism on the flickering and the overall data rate of the system. The proposed system in [110] employs expensive lenses to focus the light emitted from one LED onto the other. Thanks to these lenses, a transmission distance up to 2 m could be reached while transmitting at data rates up to 2.5 Mbps. However, the paper does not mention the rate of switching and whether the bidirectional channel could achieve the same data rates as the one-directional link. Similarly, in [111], a short-distance communication system is implemented just to transmit text data between two computers at a maximum rate of 9600 baud over 5 cm. There is no mentioning of the switching speed between transmission and detection mode and whether flicker could be noticed during or between transmission intervals.

For the proposed LED-to-LED communication system in this thesis, an analogue switch integrated circuit (CD4066) is employed to switch between transmission and detection mode. In transmission (Tx) mode, the LED pins are connected to the current-mirror-based LED driver circuit to provide forward bias as well as feed the LED with the modulated signal. For reception (Rx) mode, the LED pins are disconnected from the LED driver circuit and are connected to the inputs of the TIA under no bias to detect the incoming light signal.

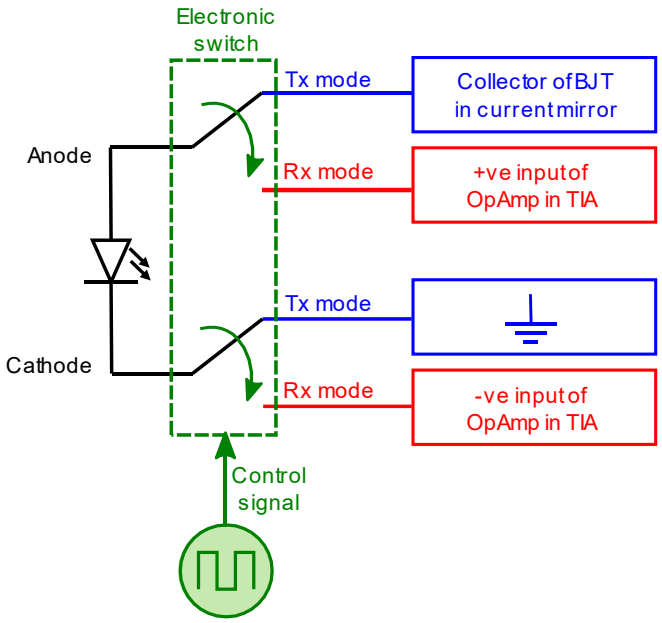

Figure 4-18: Block diagram of switching

The switching block diagram is shown in Figure 4-18. Three important characteristics are tested in a switching circuit:

- The attenuation factor in the “on” state
- The attenuation factor in the “off” state
- The transition characteristics including maximum switching speed

The switching circuit is experimentally characterised regarding those factors without the effect of the remaining electrical or optical components according to the setup depicted in Figure 4-19. The complete circuit including the switching between transmission and detection modes is depicted in Figure 4-20.

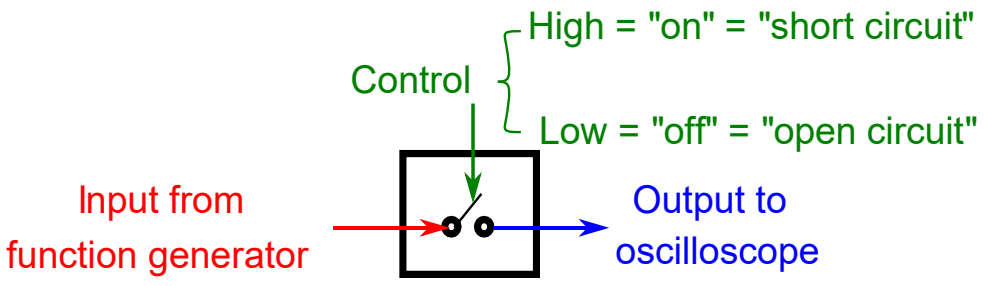

Figure 4-19: Measurement setup to experimentally characterise the switching circuit

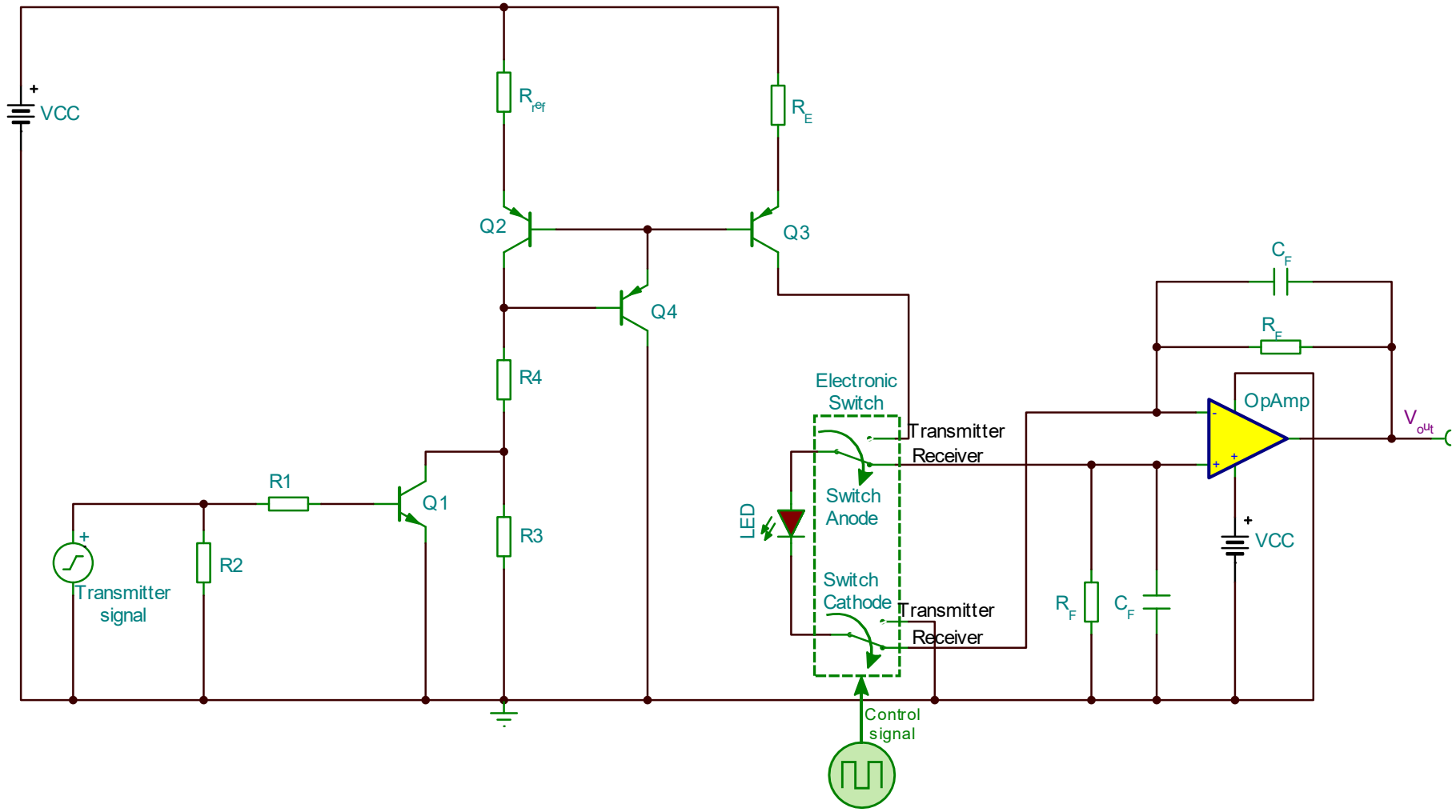

Figure 4-20: Circuit diagram of the entire proposed system including LED driver, switching circuit and TIA

4.7.1. Performance Measurement of Switching Circuit

The attenuation factor of the switch in the "on" state

In order to test the attenuation of the bilateral switch circuit in the "on" state, a square wave of 5 V peak-to-peak and 100 kHz frequency is passed from the input to the output pin while a 5 V DC is applied on the control pin. The control, input and output waveforms are displayed on the oscilloscope and depicted in Figure 4-21, drawn in green, red and blue respectively. The figure shows that the attenuation of the switch in the "on" state is negligible and that the output follows the input waveform. The attenuation is calculated by dividing the amplitude of the output voltage by that of the input voltage. It is found to be -0.08 dB, which means that 99.03% of the transmitted signal is transferred through the switch. In the optimum case, the switching circuit should have an attenuation factor of 0 dB in the "on" state. This corresponds to an ideal buffer circuit that allows the whole input waveform to be transferred without losses to the output port.

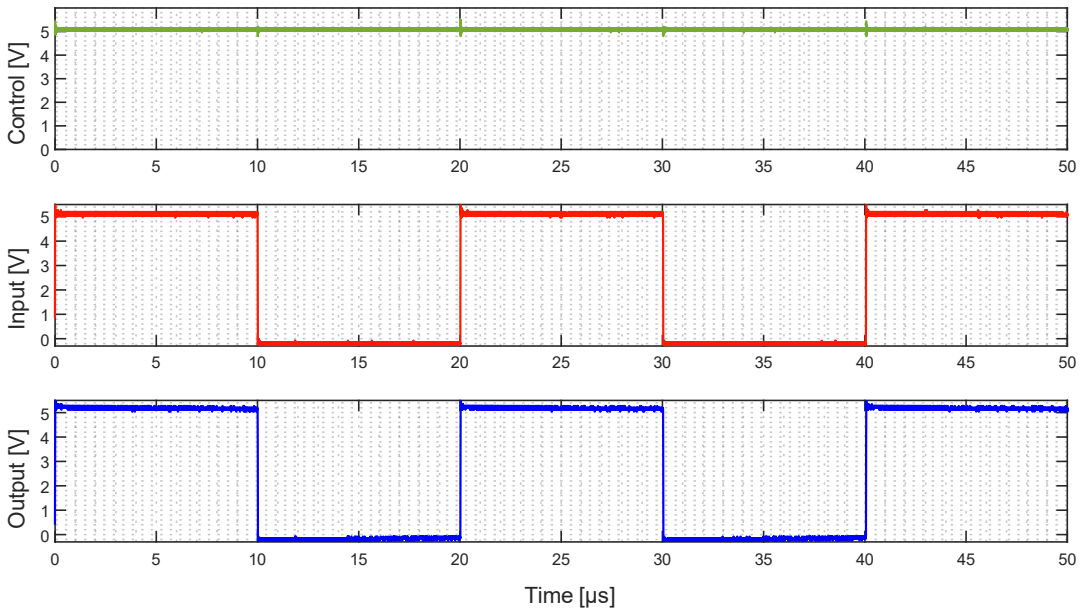

Figure 4-21: Captured waveforms of control, input and output signals when the switch is in the "on" state

Hence, with an attenuation factor of -0.08 dB, the assumption can be made that the switch functions as buffer in the “on” state.

Figure 4-22 zooms in on the captured rising edge of the input and output waveforms (as measured by the oscilloscope) to show the rise time and the propagation delay due to the switch IC. The rise time is measured between 10% and 90% of the difference between the voltage rails of the output signal. It is found to be 8.8 ns for the input signal and 11.2 ns for the output signal. However, since the input signal is not ideal, this rising time cannot be entirely blamed on the switching IC response. The output has a rise time that is only 2.4 ns longer than the input.

Hence, a more accurate measurement is the propagation delay, which is the measure of how much the circuit under test (in this case the switching circuit) delays the output signal with respect to the input signal. The propagation delay is measured from the 50% point of the input signal to the 50% point of the output signal between the voltage rails, as marked on Figure 4-22.

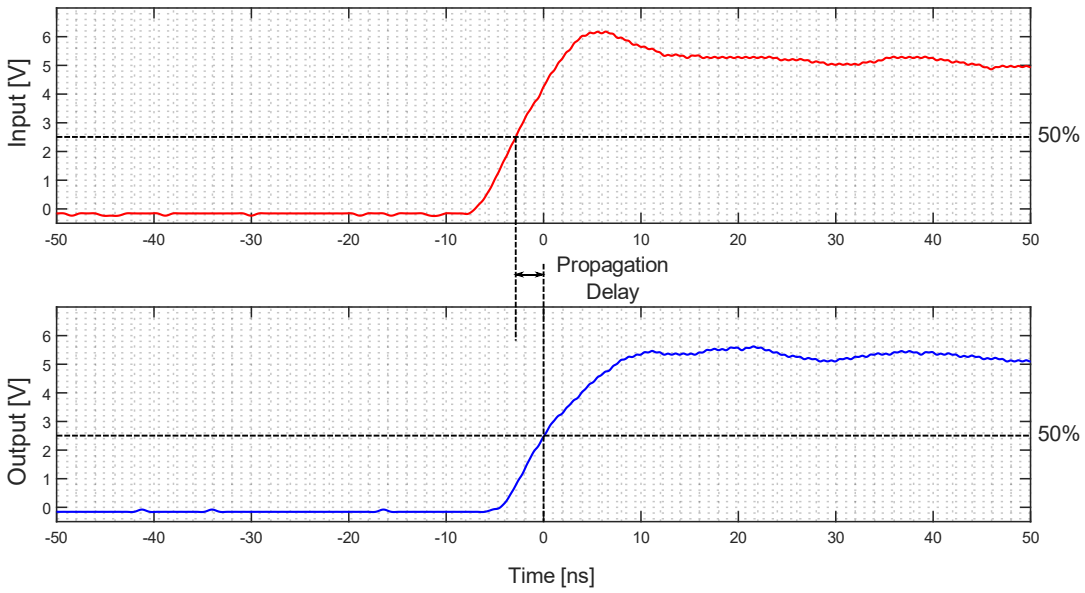

Figure 4-22: Captured waveforms of input and output of the switch during transition

Employing this method, the propagation delay is measured to be 3 ns. Hence it can be safe to say that the switching circuit allows signals up to a frequency of 116 MHz to pass in the “on” state without distortion, according to equation (4.8).

The attenuation factor of the switch in the “off” state

The experiment above is repeated when the control signal is connected to the ground, turning the switch thereby to the “off” state. The captured waveforms on the oscilloscope for the control, input and output signals are depicted in Figure 4-23. Again, the output and input signals are compared, and the attenuation is calculated from their peak-to-peak amplitudes. Ideally, the output in the “off” state should be zero, regardless of the input signal.

The measurements in Figure 4-23 reveal that in the “off state” some of the input signal is transferred to the output port resulting in a DC-shifted square wave with peak-to-peak amplitude of 0.32 V. By dividing the output and input amplitudes, the attenuation factor is found to be -24.5 dB, meaning that 5.9% of the input is transmitted to the output. Moreover, the DC shift of the output signal is not zero

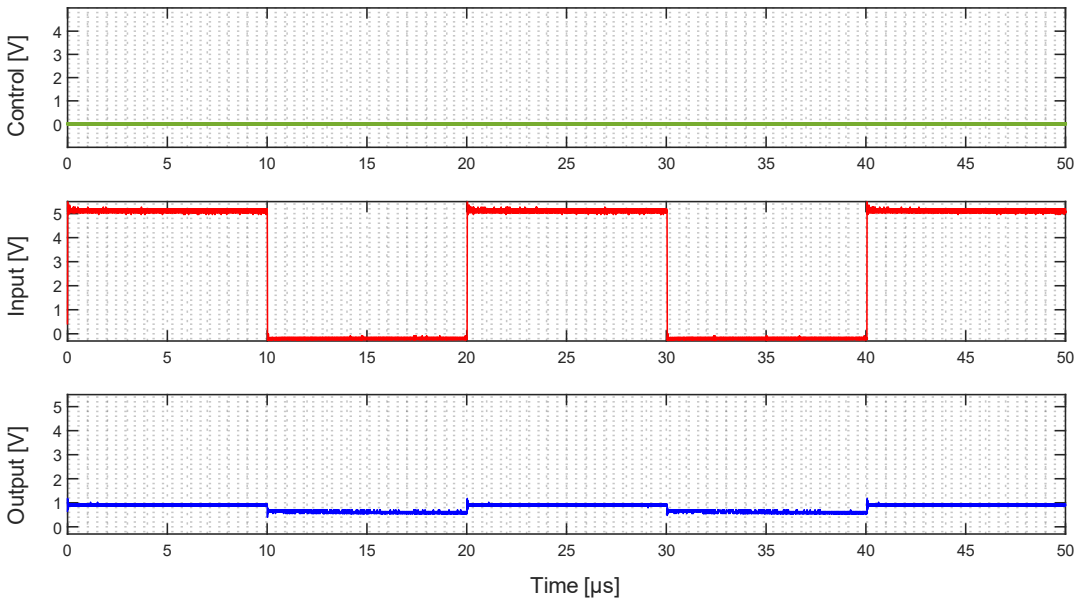

Figure 4-23: Captured waveforms of control, input and output signals when the switch is in the “off” state

as expected, but around 0.6 V. While the output is low compared to the input, it still has to be accounted for in the bidirectional system because such a DC value can cause the TIA to saturate in the detection mode.

The transition characteristics of the switch

In order to test the switching speed, a DC signal is applied to the input port and the output is observed on the oscilloscope upon toggling the control signal from low to high at a frequency of 1 KHz. The control, input and output signals are shown in Figure 4-24. The focus is zoomed on the transition between the “on” and “off” states to see the rise and fall time, which can determine the maximum switching speed. It can be seen from the figure that the rise time of the output signal is very short in comparison to the fall time, which means that the switch turns on quickly but turns off much slower. The fall time is the limiting factor to the switching speed. It is calculated between 90% and 10% at the output signal and is found to be 0,493 ms on average. This results in a maximum possible switching speed of around 710 Hz according to equation (4.8).

It is important to point out that the fall time is dependent on the load resistance. Since in this scenario, the output is measured directly by the probes of the oscilloscopes, it is encountering a load resistance of 10 MΩ, which represents the worst-case scenario.

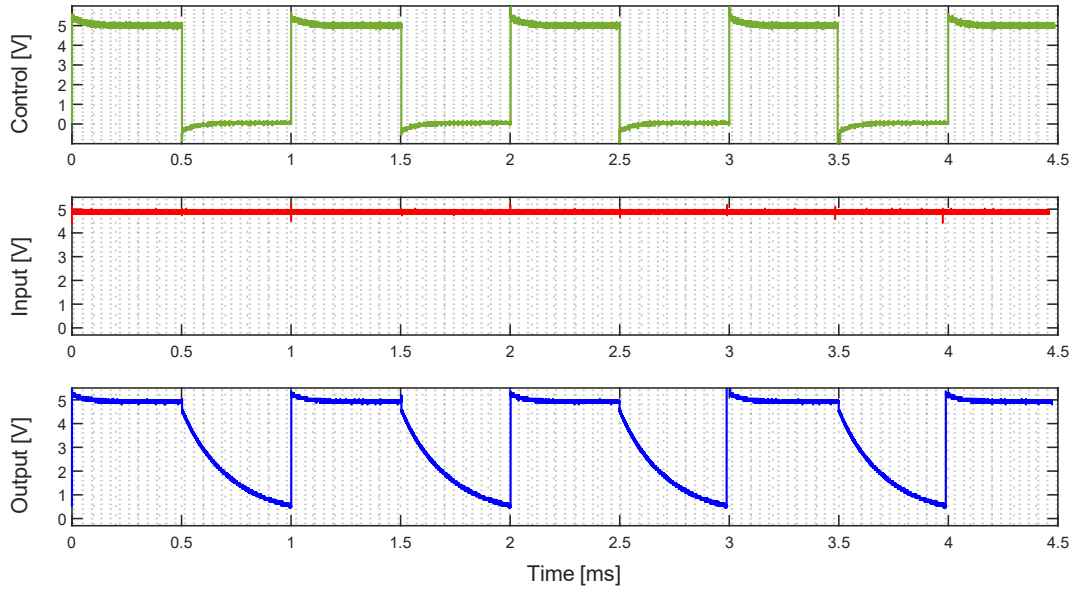

Figure 4-24: Switch response when control signal is toggling at 1 kHz

From the exponential decay of the output curve in Figure 4-24 it can be seen that the output curve resembles the capacitor discharge curve, represented by:

$$V_C = V_S \cdot e^{-t/R_{\text{load}}C}\,, \tag{4.17}$$

where V_C is the voltage on the capacitor, V_S is the source voltage (5 V in this case), t is the time, R_{load} is the load resistance (10 MΩ in this case) and C is the output capacitance. By substituting with a value of V_C and t in equation (4.17) and rearranging the equation to calculate the value of the capacitor C, it is found to be 0,0236 nF.

Assuming that the switch is being directly connected to the LED pins and seeing only the LED as load resistance, the fall time will be much shorter than the measured value when connected to the probes of the oscilloscope. The load resistance R_{load} of the LED is estimated to be 10 Ω in forward bias. When substituting in the exponential decay function with the 90% and 10% voltage values and the known R_{load} as well as the previously calculated output capacitance, the fall time t_f can be calculated as follows:

$$t_f = t_{10\%} - t_{90\%} = -RC \ln\frac{0.5\ V}{5\ V} + RC \ln\frac{4.5\ V}{5\ V} \cong 2.2\ RC\,, \tag{4.18}$$

where $t_{90\%}$ and $t_{10\%}$ are the times at which the voltage reaches 90% and 10% of its maximum value, respectively. The fall time is accordingly calculated to be 5.2 ns, allowing for a maximum switching speed of 67.5 MHz in the best-case scenario. The worst-case scenario is the one that should be accounted for in the design however, because the output of the switch is also connected to the TIA in receiving mode. In that case, the load resistance is large due to the input of the TIA and the large feedback resistor.

To find out the impact of the transition between the “on” and “off” states on a varying input signal, the next experiment focuses on toggling the switch control while sending a square wave of much higher frequency from the input to the output port of the switch IC. The control, input and output signals are shown in Figure 4-25, zoomed in at the transition of the control signal from the “off” to the “on” state. The experiment is repeated at switching frequencies 100 Hz, 200 Hz and 300 Hz, while the transmitted signal frequency is kept at 100 kHz.

From the figure, it is obvious that in the “on” state and during the transition from “on” to “off”, the behaviour of the switching IC is nearly ideal: The transmitted signal is instantly transmitted from the input to the output port upon toggling the control signal from “off” to “on”. The transmitted signal experiences nearly no losses or distortion due to the switching IC. However, in the “off” state (when the control signal is low), the attenuated and DC shifted square wave is visible, which confirms the low performance of the switching circuit in that state.

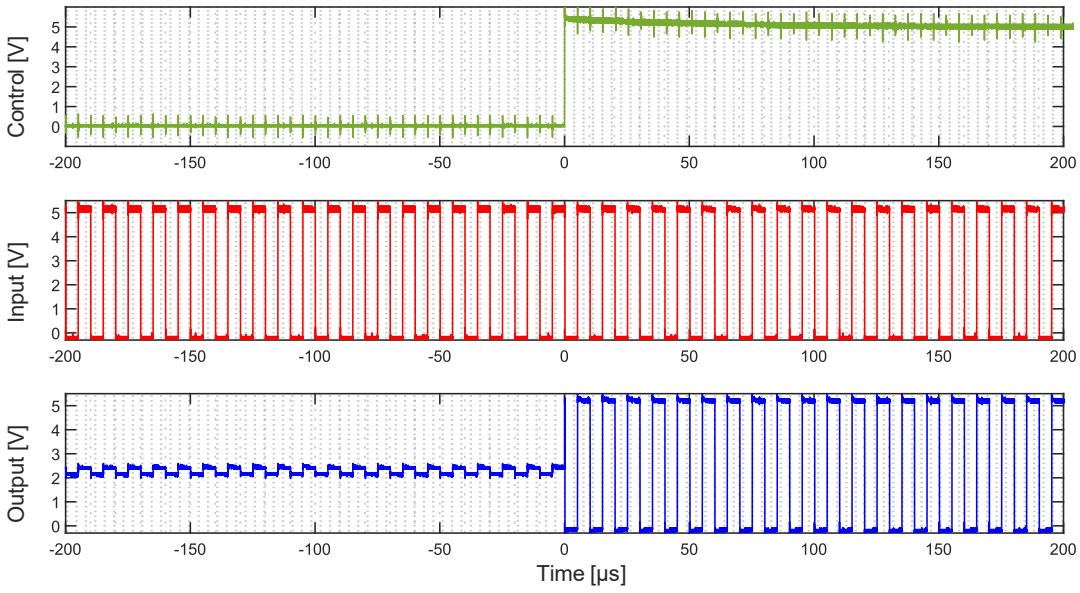

Figure 4-25: Toggling switch input from “off” to “on” at 100 Hz

Figure 4-26 focuses on the falling edge of the control signal instead. Here again, the control signal is toggled at a frequency of 100 Hz while a 100 kHz square wave is transmitted from the input to the output port of the switch IC.

Although the switch shows good response in the “on” state and during the transition from “off” to “on”, its response has major drawbacks in the “off” state and on the falling edge of the control signal. Firstly, it fails to entirely suppress the input signal in the “off” state, so that an attenuated version of it is still visible at the output port. Secondly, the long fall time of the IC upon turning off causes baseline wandering of the suppressed input signal, resulting in a high signal amplitude directly after the switching off. Finally, the DC value of the suppressed signal lies at around 2.5 V, not 0 V as expected. This is problematic in the photodetection scenario, since the photocurrent produced by the receiver LED will be superimposed on the transmitted signals waveforms that have not been properly suppressed by the switch at the pins of the LED. The transmitter signal would then cause an interference with the detected signal, resulting in possible higher bit error rate and prevention of successful transmission.

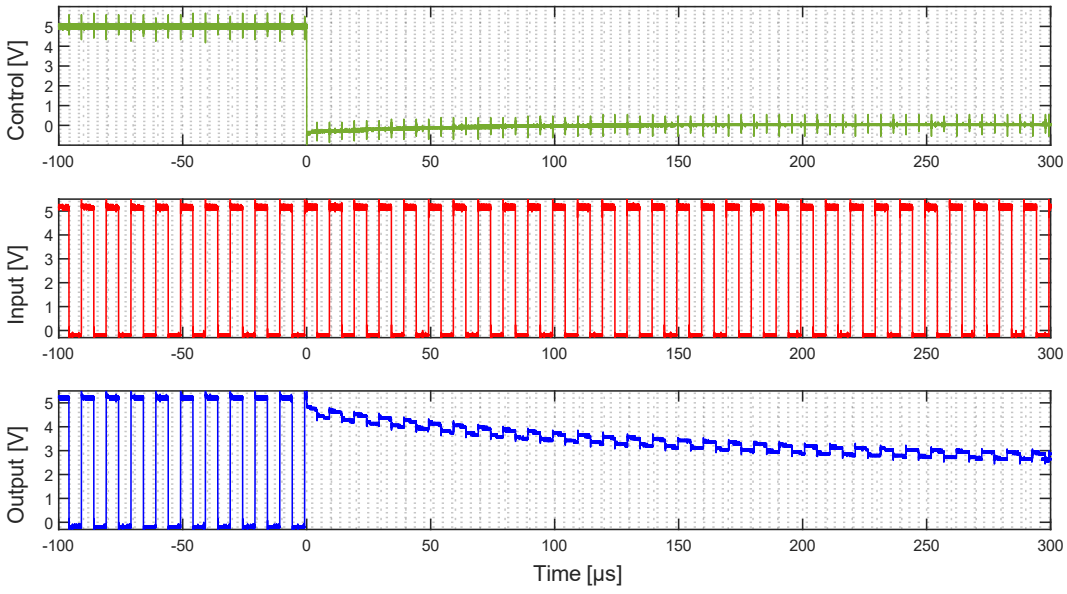

Figure 4-26: Captured signals when toggling switch input from “on” to “off” at 100 Hz

4.7.2. Recommendations for Incorporating the Switching Circuit

Now that the switching circuit is characterised, certain recommendations can be made for combining the switching component and the transceiver to optimise the overall system design.

It is established from the practical measurements of the switching circuit that it can only provide a mediocre response in its “off” state. This response can be seen in three aspects as follows:

- The circuit is unable of completely suppressing the varying input signal in the “off” state. The switch allows an attenuated signal of the input to reach the output despite the low control signal.
- The DC value is measured during the “off” state at the output port of the switch in the presence of an input. This DC value was expected to be zero.
- The circuit has a long fall time at the transition from the “on” to the “off” state causing baseline wandering of the input signals.

To mitigate the inability of the switch to suppress the DC and AC values of the input signal, it is recommended to stop the input signal (transmitter) upon toggling the control signal. This will cause the input and output port of the switch to be held at zero when the control signal is low. In the proposed transceiver design this translates to disabling the transmitted signal during photodetection mode. In this way, the transmitter signal cannot be superimposed on the detected signal on the LED pins. The signal on the LED pins will thus be only due to the photodetection process and errors can thereby be avoided.

To compensate for the long fall time of the switch while transitioning from the “on” to the “off” state, it is recommended that the transmission and detection are delayed a period t_f after the switch transition. This will allow the output signal

from the switch to stabilise on the low rail before being exposed to any data from the photodetection period. Although this will affect the overall data rate of the system, it will guarantee lower bit error rates.

Lastly, perfect synchronisation between the transmitter and receiver devices is required for the error-free transmission of the communication data between the devices to prevent packet collision. An entirely software-based synchronisation solution could be implemented according to [91].

To satisfy those requirements, this thesis proposes and implements a simple algorithm to regulate the transmission and reception timing as will be discussed in the next section as well as in chapter 7.

4.7.3. Relation between Switching Speed and System Data Rate

As previously established, the switching speed between transmission and detection mode should be kept larger than 100 Hz to prevent the nearby human observer from noticing the flickering effect. However, the switching circuitry is only capable of stable functioning at a maximum switching speed of around 710 Hz, so this limit should not be overcome either.

To determine the relation between the data rate of the system and the switching speed, the timing diagram in Figure 4-27 is considered. The figure depicts the control signal as seen by a transceiver circuit on one end of the channel (denoted Tx1). The data sent by transmitter 1 (Tx1) and transmitter 2 (Tx2) on the other end of the channel are drawn in blue and green, respectively. It can be seen from the figure that the transmitted bits are delayed by t_f with respect to the control signal to allow for the output signal to stabilise before data is transmitted. This

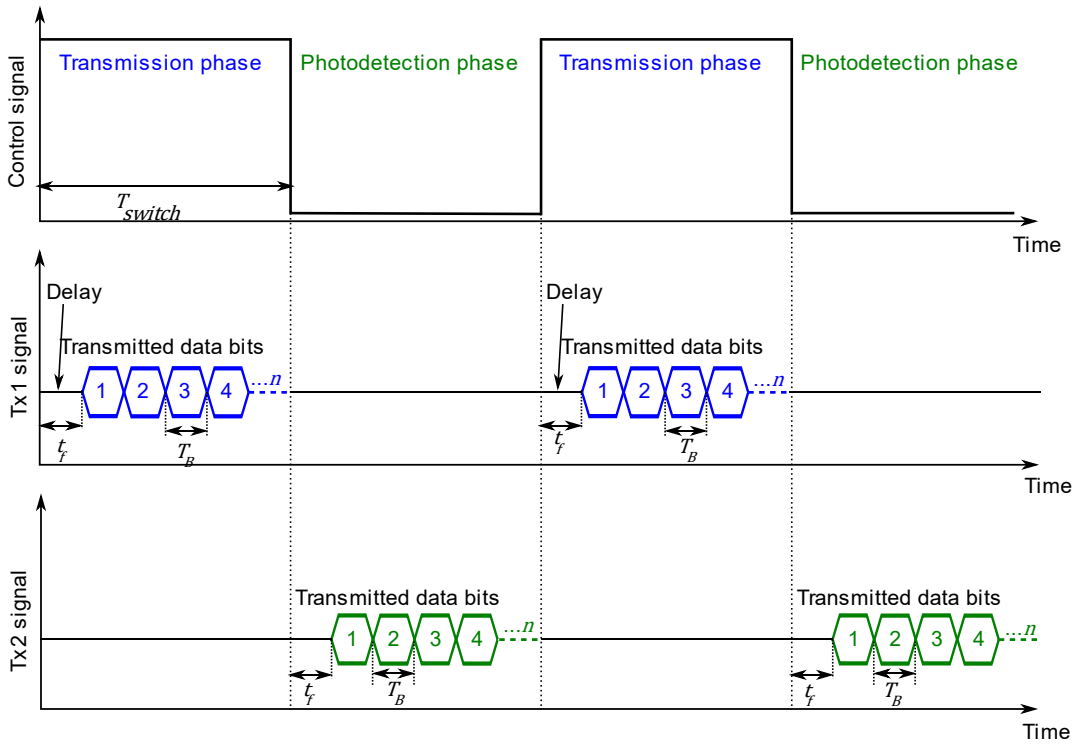

Figure 4-27: Timing diagram for control and transmitted signals

complies with the recommendation made in the previous section to mitigate the effect of the long fall time of the switching circuit.

The overall data rate of the system is defined as the total number of bits sent by Tx1 and Tx2 combined per second, assuming error-free detection. For the sake of simplifying the calculations, it is assumed that Tx1 and Tx2 are both sending data in their respective transmission times only and at equal data rates. Moreover, it is assumed that the “on” and “off” time of the switch T_{switch} are equal for the transmission and photodetection phases and are longer than the bit duration T_b.

From the timing diagram in Figure 4-27, during any transmission phase, n bits (of bit duration T_b each) are sent from one transceiver module to the other after a delay period at the begin of the transmission phase, denoted t_f. Hence, the following equation relates the switching time with the bit duration:

$$T_{\text{switch}} = t_f + nT_b \,. \tag{4.19}$$

Hence, the number of bits transmitted during the switching time (n) can be expressed by transforming equation (4.19) as follows:

$$n = \left\lfloor \frac{T_{\text{switch}} - t_f}{T_b} \right\rfloor. \tag{4.20}$$

It is important to point out here that n must be an integer value. If the term $\frac{T_{\text{switch}} - t_f}{T_b}$ in equation (4.20) resulted in a non-integer value because the value $(T_{\text{switch}} - t_f)$ is not a multiple of T_b, then the resulting number must be rounded down to the next smaller integer, hence the floor brackets.

To get the system data rate, equation (4.20) has to be divided by the switching time T_{switch}, resulting in:

$$\text{data rate} = \frac{n}{T_{\text{switch}}} = \frac{T_{\text{switch}} - t_f}{T_b T_{\text{switch}}}. \tag{4.21}$$

The switching frequency f_{switch} and the bit rate r_B can be related to the switching time T_{switch} and bit duration T_b, respectively, as follows:

$$f_{\text{switch}} = {}^{1}/_{T_{\text{switch}}}, \tag{4.22}$$

$$r_B = {}^{1}/_{T_b}. \tag{4.23}$$

Hence, equation (4.21) can be written as:

$$\text{data rate} = \frac{\frac{1}{f_{\text{switch}}} - t_f}{\frac{1}{r_B} \cdot \frac{1}{f_{\text{switch}}}} = r_B f_{\text{switch}} \left(\frac{1}{f_{\text{switch}}} - t_f \right). \tag{4.24}$$

Simplifying the expression in equation (4.24), the overall system data rate can be written as:

$$\text{data rate} = r_B \left(1 - f_{\text{switch}} t_f\right). \tag{4.25}$$

Equation (4.25) highlights the data rate penalty due to the use of the switching circuit and its fall time. The data rate of the system is reduced by the factor ($f_{\text{switch}} \cdot t_f$) compared to its original value. Since the value of t_f is determined only by circuit components, the switching frequency is the limiting and determining factor of the overall data rate of the system. It is important to consider that the data rate expressed in equation (4.25) applies only to a modulation technique that has two levels, i.e. only one symbol can be sent per bit. An example of such a modulation technique is the NRZ OOK technique, which is chosen for

modulating the data in the proposed system. If the number of symbols per bit S increases due to the use of a multi-level modulation technique, the overall system data rate is expressed as follows:

$$\text{data rate} = (r_B - r_B f_{\text{switch}} t_f) \log_2(S) = r_B \log_2(S) \, (1 - f_{\text{switch}} t_f) \, . \qquad (4.26)$$

To illustrate this relationship on a numerical example, the data rate of the system is calculated for 100 Hz switching frequency, 50 kbps transmission bit rate and 0.5 ms fall time. OOK NRZ modulation is assumed, hence $S = 2$. By substituting with those values in equation (4.26), the resulting data rate is 47.5 kbps, 5% less than the data rate achieved without switching (50 kbps).

4.8. Conclusion

In this chapter, the proposed LED-to-LED communication system is introduced, and its modules and components characterised both through simulations and practical experimentations. All parts of the proposed system are practically characterised without the effect of the LED to evaluate their performance, independent of the optical components.

The LED driver design consists of pnp BJTs configured as a Beta Helper current mirror design to provide 20 mA of current. This drives the LED at high brightness with practically measured speeds up to 412 kHz. The simple OpAmp based transimpedance amplifier design accommodates the low sensitivity of the LED photodetector by providing a 2 V/µA amplification factor while having a bandwidth of up to 335 kHz. The simulation of the back-to-back transceiver reveals the feasibility of the system at speeds up to 130 kHz.

Lastly, the analogue switch controls the flow of the signal to and from the LED and allows successful switching between transmission and detection modes. The switching speed maximum lies at 710 Hz, which is sufficient for flicker prevention. While switched on, the analogue switch is capable of transmitting signals with nearly no losses or distortion at speeds in the MHz range. While switched “off” however, the switching circuit shows significant deficiencies such as a long fall time and not sufficient suppression of the input signal. These effects must be accounted for in the design and implementation of the transmission and detection algorithms. The mathematical derivation of the overall system data rate reveals that the penalty in the maximum achieved data rate is related to the switching frequency and fall time. Therefore, the switching frequency must be chosen wisely to achieve the maximum potential of the system.

In the next chapter, the noise and interference on the visible light communication system due to ambient light sources are characterised to evaluate their effect on the proposed system. Chapter 7 and 8 then implement and practically characterise the whole system with and without the switching circuit, respectively.

Chapter 5

Noise and Interference on Indoor VLC Channel

5.1. Introduction

The performance of a visible light communication link suffers greatly due to the channel effects. Two major sources are affecting the VLC channel: noise and interference. Noise is defined as the unwanted distortion of the signal due to internal and external effects while interference is the unwanted effect due to signals from other sources that are geographically located in the same place as the system under test. This chapter covers the basics of the noise affecting the VLC channel and characterises the interference sources. It also presents a mathematical model for the variance of the thermal and shot noise and the interference on the VLC link due to contemporary and modern ambient light sources.

5.2. Noise in a VLC channel

Noise in a VLC channel is considered a stationary random process with time-invariant variance. It can be categorised into shot noise and thermal noise as discussed in the sections below [63], [112], [113].

5.2.1. Thermal Noise

Thermal noise is caused by variations of electron quantity and motion inside the electronics of the receiver circuit. It arises due to the collision of electrons in conductors and is dependent on the operating temperature T and load resistance R_{load} of the conducting material. Thermal noise is independent on the incident optical power. It is estimated as an additive white Gaussian noise (AWGN) with zero mean and variance given by [38]:

$$\sigma_{\mathrm{Thermal}}^2 = \frac{4kT}{R_{\mathrm{load}}} F_n \,, \tag{5.1}$$

where k is Boltzmann's constant, T is the temperature, R_{load} is the equivalent load resistance and F_n is the noise figure. The noise figure is an indication for the noise created by the system itself and is defined as the ratio between the signal to noise ratio at the output to that at the input. The thermal noise is considered 'white' since its power spectral density does not depend on the frequency.

5.2.2. Shot Noise

Unlike thermal noise, shot noise is dependent on the incident optical power. It is caused due to the fluctuations in the number of photons received by the active area of the photodetector, which is due to the quantum nature of light. Although the average number of photons per second that are produced by a light source is almost constant, the instantaneous number varies and can be modelled by a Poisson distribution.

The photocurrent produced by the photodiode follows those variations in the number of incident photons. The average photocurrent $\langle i_{\mathrm{ph}} \rangle$ produced by an average number of electrons $\langle N_e \rangle$ in the photodiode during a bit duration T_b can hence be written as:

$$\langle i_{\mathrm{ph}} \rangle = \frac{e\langle N_e \rangle}{T_b} \tag{5.2}$$

The magnitude of the shot noise increases with the square root of the incident optical power. It is also dependent on the bandwidth of the employed filter after the photodiode. The variance of the shot noise is given by [38]:

$$\sigma_{\mathrm{shot}}^2 = 2e\langle i_{\mathrm{ph}} \rangle BW_{3dB} \tag{5.3}$$

where e is the electron charge, $\langle i_{\mathrm{ph}} \rangle$ is the average photocurrent produced by the photodiode and BW_{3dB} is the bandwidth of the electrical filter after the photodiode.

5.3. Interference in VLC channel

In addition to noise, ambient light sources (whether natural, such as the sun, or artificial, such as lamps) cause interference on the VLC system and have a twofold effect on its performance. Firstly, they cause a time-varying interference signal which is detected by the VLC system and may hinder the right reception of the communication signal. Secondly, they increase the amount of shot noise at the receiver end of the system because of the increased light power on the detector area [63], [114], [115].

If those sources of interference were constant in time (such as the sun) and do not saturate the photodetector, their effect could be eliminated easily using filters, appropriate thresholding or DC shifting [63]. The irradiance of the sun I_{sun} is defined as the optical power per unit area of the photodetector and is given by:

$$I_{\text{sun}} = W(\lambda) BW_{\text{BPF}} \tag{5.4}$$

where $W(\lambda)$ is the spectral radiant emittance of the sun and BW_{BPF} is the bandwidth of the optical bandpass filter before the photodiode. The impact of such a constant background noise can be reduced using a very narrow field of view and bandwidth of the optical filter [67].

Artificial light sources however are of time-varying nature because they are driven by the mains power and - in some cases - electronic ballast driving circuits. The resulting power is therefore periodic and deterministic. In addition, the produced light from those sources has the same wavelength as the visible light and can therefore not be eliminated using filters. It is therefore imperative to practically determine the DC power, variance and power spectral densities of those artificial light sources to account for them properly in the link budget analysis [63], [114], [115].

Similar measurements have been performed on older light sources such as Tungsten light bulbs. Moreira *et al.* characterised the effect of fluorescent and incandescent ambient light sources on the IR channel [115]. Boucouvalas also considered the effect of a wide range of ambient light sources, including IR remote controls, on the VLC channel and studied their spectra in [63]. However, to the author's knowledge, the interference of modern artificial illumination sources such as gas discharge lamps, dimmable and non-dimmable LEDs still needs to be investigated.

5.3.1. Contemporary Light Sources

To determine the interference from the contemporary light sources, they are first categorised into three main types: thermal light sources, gas discharge lamps and semiconductor light sources [116]. The latter category is also divided into two types: dimmable and non-dimmable sources.

In thermal light sources, also called incandescent sources, current flows through a thin filament inside the vacuum in the light bulb. The heat produced by this current flow causes the filament to glow without burning it out due to the lack of oxygen in the vacuumed chamber. Aside from light, the majority of the power delivered to the thermal light source is converted into heat. That is why thermal light sources are considered inefficient and most of their types have been banned from the European Union (EU). However, more energy-efficient variations of them are still used in the EU and many non-EU countries in domestic and retail environments. An example of thermal light sources is the Tungsten light bulb [116].

Gas discharge lamps on the other hand employ a gas filled discharge tube placed between two electrodes to produce ultra-violet light under the effect of an

alternating electric field. The ultra-violet light is then converted into visible light by the fluorescent coating inside the lamp. These light sources have a higher efficiency and lifetime than thermal light bulbs but produce a lower colour rendering. They are widely used in retail areas and offices to provide wide-area lightning [116]. Examples of gas discharge lamps include fluorescent and energy saving light bulbs.

The last category of ambient light sources is the semiconductors, to which the LED belongs. Because the LED can only operate under DC current, they can only be used in an AC network by employing a DC converter. In the last decade, the LED as light source has become famous for illumination due to its long lifetime, its energy efficiency and its flexibility to produce different colours and temperatures of light.

Some variations of the LED light sources can offer three levels of brightness by containing two LEDs (that have different intensity levels) in the same casing. The lowest brightness level is achieved by turning the low-power LED on, while the middle level is achieved by turning the high-power LED on. Turning both LEDs on at the same time produces the maximum light intensity [27]. This kind of LED is referred to as 3-way LED.

Other variations of LED sources can be dimmed in an analogue way by employing pulse-width-modulation (PWM). The quick on-off switching of the LED at frequencies higher than those detected by the human eye cause the overall LED brightness to decrease according to the duty cycle of the PWM signal. To the user, this appears as if the LED is dimmed. Although this feature is very desirable for producing the right light ambience, it is problematic for the receiver of the VLC channel, which is normally fast enough to detect those PWM signals [27].

In the next section, a measurement setup is proposed to measure the noise and interference caused by those different light sources on the VLC channel.

5.3.2. Measurement Setup

The block diagram in Figure 5-1 shows the measurement setup for measuring the interference caused by ambient light sources on the VLC channel. On the transmitter end, a generic light source driver connected to the mains supply (220 V, 50 Hz) drives the ambient light sources under test separately. The visible light from the source propagates to a photodetector placed 1 m away directly in front of the light source at 0° angle between the axis of the transmitter and receiver. The 1 m distance and 0° angle ensure that the measurement is done at the worst-case scenario but without saturating the PIN photodiode [27].

At the receiving end, the silicon-based PIN photodiode (PM16-121C) (spectral range: 400 - 1100 nm, optical power sensing range: 500 nW – 500 mW) of an optical power and energy meter (Thorlabs PM200) captures the light signal. The measuring device has a response time of 1 µs and can measure up to 1 MHz frequency, which ensures that all fluctuations are captured accurately. The output

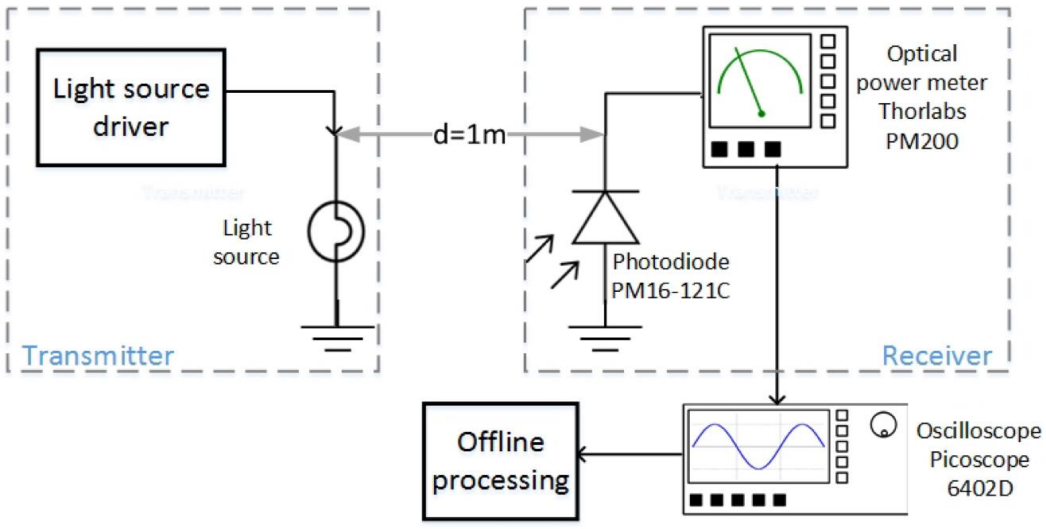

Figure 5-1: Measurement setup for measuring the power of the interference sources [27]

of the power and energy meter is then converted from digital to analogue form and transmitted to a PC oscilloscope (Picoscope 6402D) (Bandwidth: 500 MHz), then stored offline for further analysis. Both the time-domain waveform and the power spectral density (PSD) are captured. The sampling rate of the PC oscilloscope is set to 1 M Samples/s to ensure that all high frequency variations are captured. To ensure that the measured light power is caused only by the source under test, the tests are performed in a dark room. Care has been taken to properly ground all equipment to avoid electromagnetic interference caused by ground loops. The displayed results are the average of several repeated measurements [27]. The stored signals are then analysed offline in terms of their variance, DC component, bandwidth and significant harmonics. The pictures in Figure 5-2 show the equipment and the measurement setup for the performed experiments.

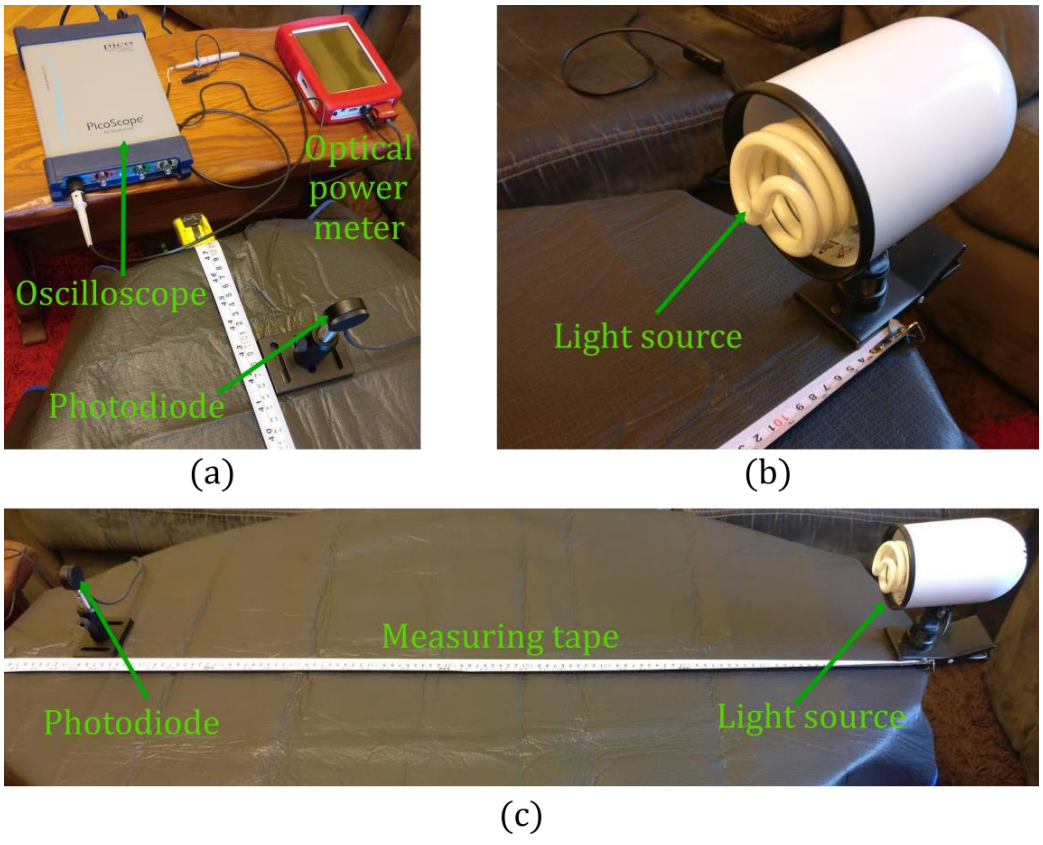

Figure 5-2: Experimental setup and equipment. (a) Receiver: Optical power meter connected to oscilloscope, (b) light source and driver, (c) 1 m channel

5.3.3. Measurement Results

Thermal light sources

Firstly, the power transmitted by a thermal light source, specifically a Tungsten light bulb (Philips® 248872 Soft white 65 W) is measured. The time domain wave form resembles an almost perfect sine wave of 10 ms period with an average DC power of 1 mW and 0.28 mW of peak-to-peak amplitude, as seen in Figure 5-3. The value of power is measured from the voltage V_{out} according to the following equation:

$$V_{\text{out}} = 2V \frac{\text{measured power value}}{\text{full scale power value}}. \tag{5.5}$$

Transforming equation (5.5), the measured power value can be calculated from the set full scale value on the power meter and the output voltage value displayed on the oscilloscope.

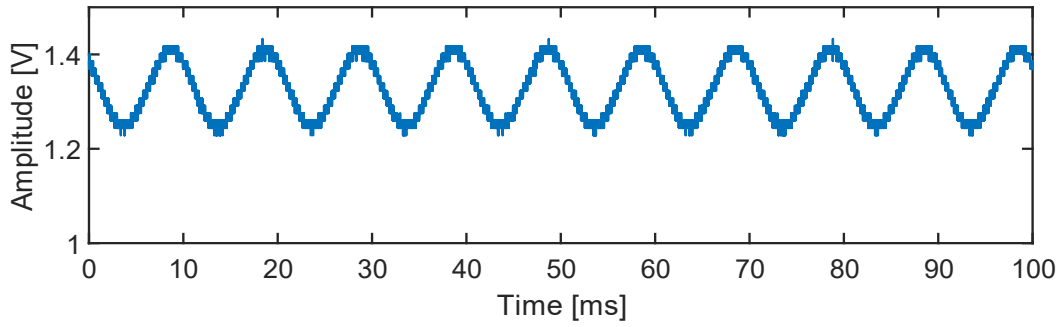

Figure 5-3: Time domain wave form of a Tungsten light bulb power [27]

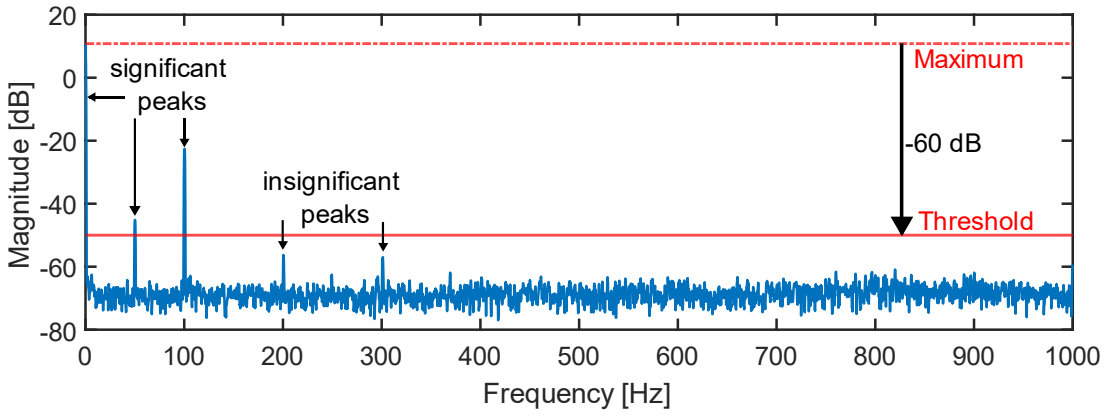

Figure 5-4: Power spectral density of the light power of a Tungsten light bulb

Using the fast Fourier transform (FFT), the frequency domain of the same waveform (corresponding to the PSD of the interference signal) is depicted in Figure 5-4. The periodic signal has a peak at 50 Hz, 100 Hz and 100-Hz harmonics up to 400 Hz. However, magnitudes below -60 dB of the fundamental magnitude are considered insignificant as shown in Figure 5-4 [115]. Hence, the significant bandwidth of a Tungsten light bulb is only 100 Hz [27].

The noise variance σ^2 of the said light source can be calculated as:

$$\sigma^2 = \int_{-\infty}^{\infty} (\mathrm{PSD}) df - \mu^2 , \tag{5.6}$$

where μ is the mean of the signal calculated as the DC value of the measured power signal. Based on equation (5.6), the variance of the Tungsten light bulb under test in this experiment is 0.82 mW over its significant bandwidth [27].

Gas Discharge Lamps

Secondly, the power signal of a gas discharge lamp (the energy saving light bulb manufactured by Philips Tornado® producing warm white light) is measured. Figure 5-5 displays the time-domain waveform while Figure 5-6 and Figure 5-7 show the PSD of the same power signal after applying the FFT up to 1 kHz and 100 kHz, respectively. It can be seen from the figures that the measured power signal in the time domain consists of a distorted sinusoid with a peak-to-peak variation of 7.09 µW. The frequency domain graph shows 50 Hz and 100 Hz harmonics because of the variations in the mains power. The DC shift of the periodic signal of 28.7 µW is represented by a peak at 0 Hz in the PSD graph. The high frequency switching of the electronic ballast used to drive the light bulb results in high frequency peaks detected on the power spectral density as seen

in Figure 5-7 between 20 kHz and 40 kHz. The variance of the power signal is calculated to be 115.7 µW according to equation (5.6) [27].

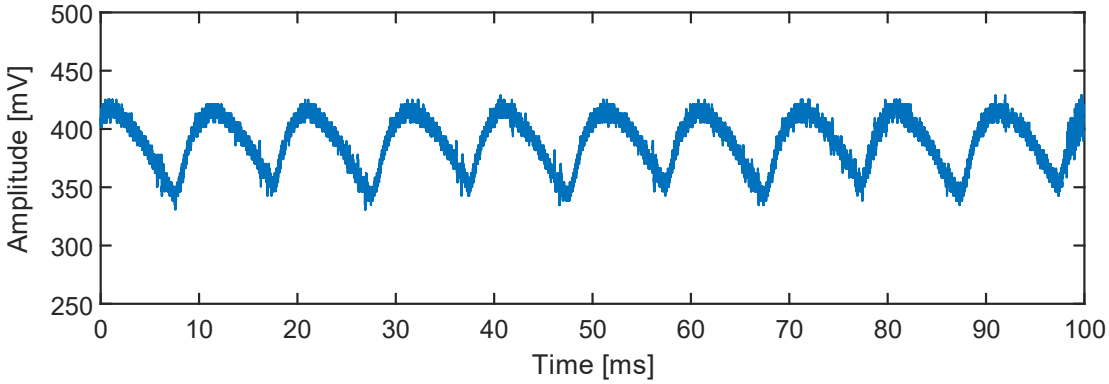

Figure 5-5: Energy saving light bulb power in the time domain [27]

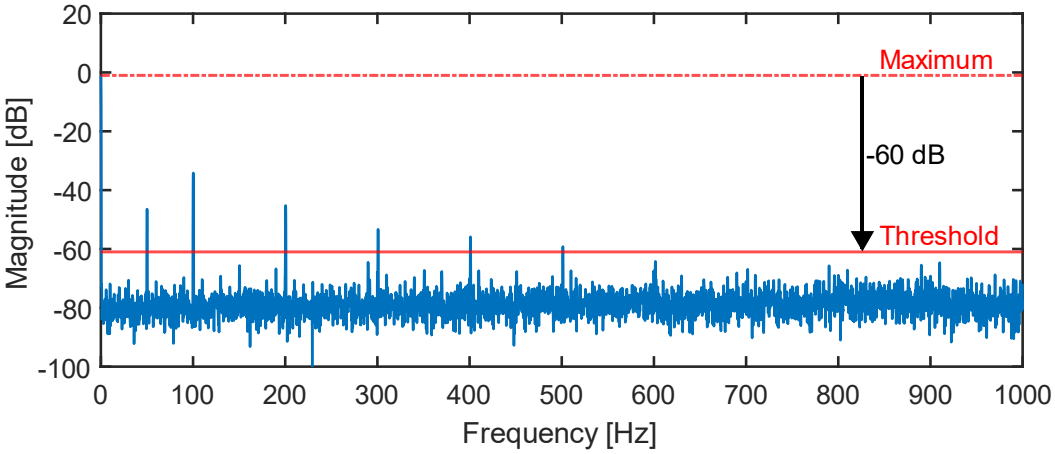

Figure 5-6: Energy saving light bulb power spectral density up to 1 kHz

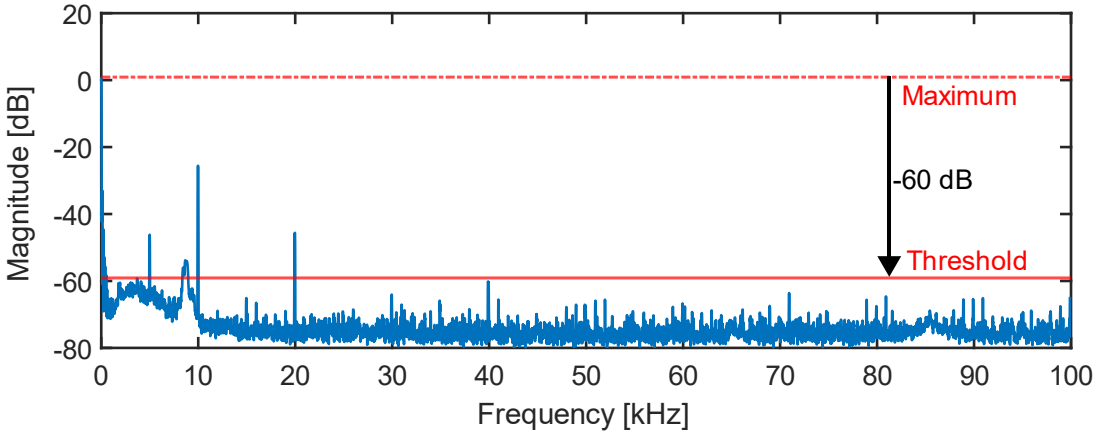

Figure 5-7: Energy saving lightbulb power spectral density up to 100 kHz

Non-dimmable semiconductor lights

Thirdly, to measure the interference of semiconductor light sources, a 3-way LED (Venus ® 6500 K colour temperature, 9 W) is tested. The three brightness levels from minimum to maximum produce 15%, 40% and 100% of the maximum brightness levels, respectively. At lowest light intensity, the LED power signal resembles that of a full-wave-rectified sine wave with period of 20 ms and only 2.25 µW peak-to-peak variation as seen in Figure 5-8. This full-wave-rectified waveform is due to the AC-to-DC conversion of the LED driver circuit. This effect is also obvious in the frequency domain of the same signal depicted in Figure 5-9 in which the significant peaks can be seen only at 50 Hz and 100 Hz. The variance of the signal is calculated to be 98.1 µW. Increasing the light intensity to the medium and maximum brightness levels keeps the frequency spectrum and waveform similar to the lowest intensity case but the amplitudes of the time and frequency domain parameters change [27].

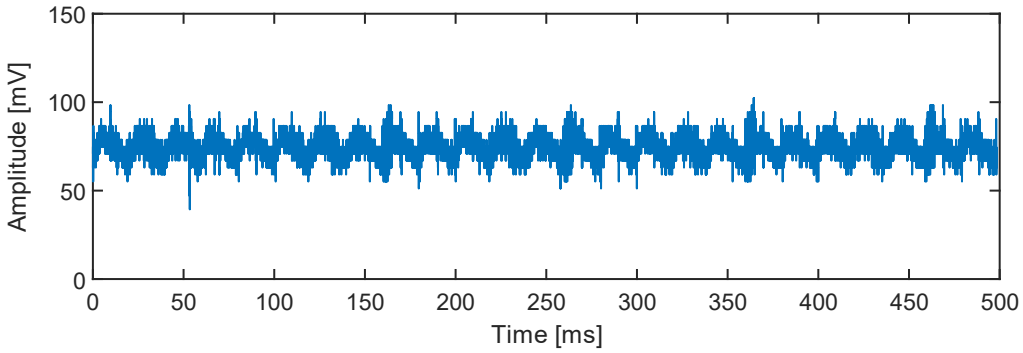

Figure 5-8: Time domain wave form of an undimmed LED at lowest intensity [27]

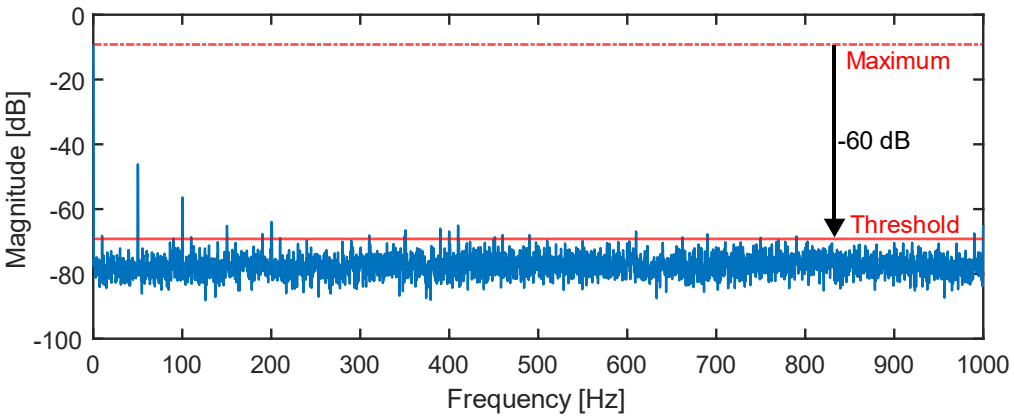

Figure 5-9: Power spectral density of an undimmed LED at lowest intensity

Dimmable semiconductor lights

To test the dimmable version of semiconductor light sources, an IKEA© dimmable transparent LED (8.6 W, 600 lm) is tested in combination with a standard off-the-shelf LED dimmer. The experiment is repeated at minimum and maximum intensity levels.

At maximum intensity, the peak-to-peak variations are measured to be 11.25 µW with a DC average of 32.8 µW and variance of 95.5 µW over a significant bandwidth of only 200 Hz. The measured spectrum is nearly flat thereafter. The time domain waveform corresponded to that of the undimmed 3-way LED light bulb as shown in Figure 5-10.

However, the dimmable version of the LED accounts for a much larger significant bandwidth of 1 kHz as a result of the high flickering rate of the PWM as shown in Figure 5-11 [27].

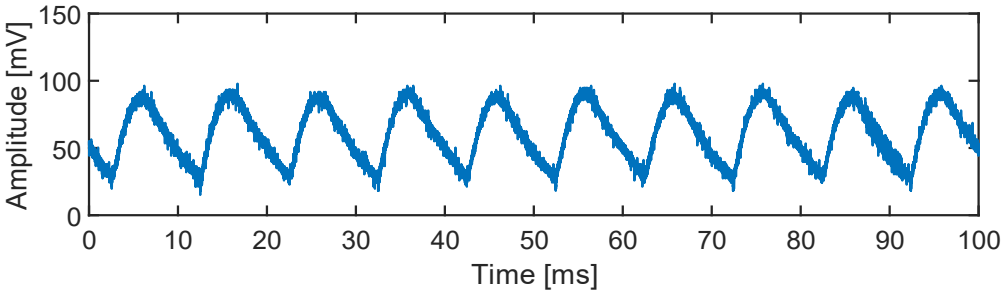

Figure 5-10: Time domain waveform of dimmable LED at lowest brightness

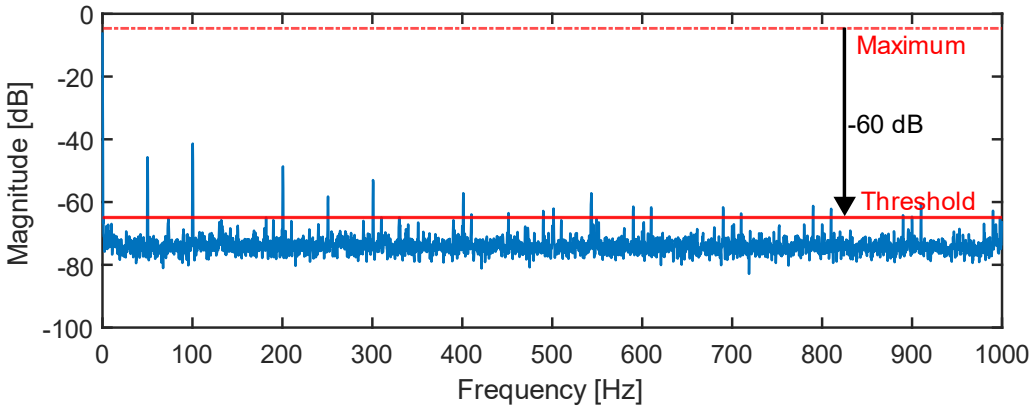

Figure 5-11: PSD of a dimmable LED light bulb at minimum brightness

Comparison of measured power signals

Figure 5-12 and Figure 5-13 compare all tested light sources in terms of their DC power level, noise variance, significant bandwidth as well as the number of peaks detected in the PSD graph within that bandwidth.

The significant bandwidth and number of significant harmonics in that bandwidth of the tested ambient light sources are compared in Figure 5-12. The figure depicts that the non-dimmable semiconductor light source produces the highest number of harmonics and has the widest noise spectrum. On the contrary, the thermal light source has the lowest number of harmonics and the lowest bandwidth. The gas discharging lamp has a low noise spectrum of just 500 Hz but its high frequency peaks at 10 kHz, 20 kHz and 40 kHz need to be taken in consideration if it is geographically located near a VLC system. To conclude, the dimmed semiconductor sources cause the widest noise bandwidth while the thermal light sources produce the least interference on the indoor VLC system [27].

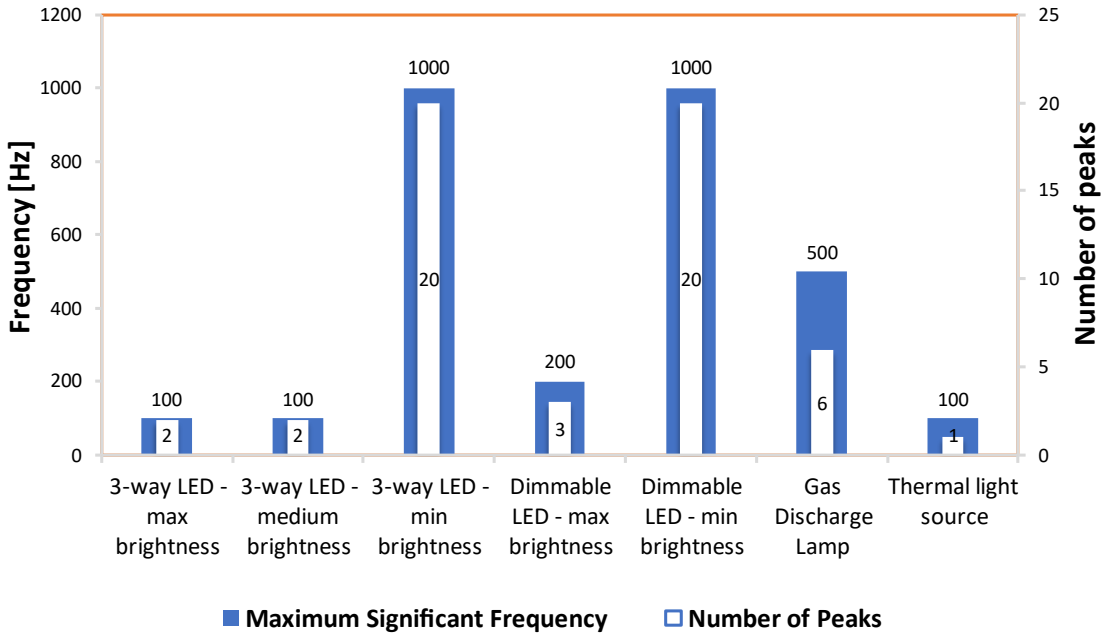

Figure 5-12: Comparison of the tested ambient light sources regarding their significant bandwidth and number of peaks [27]

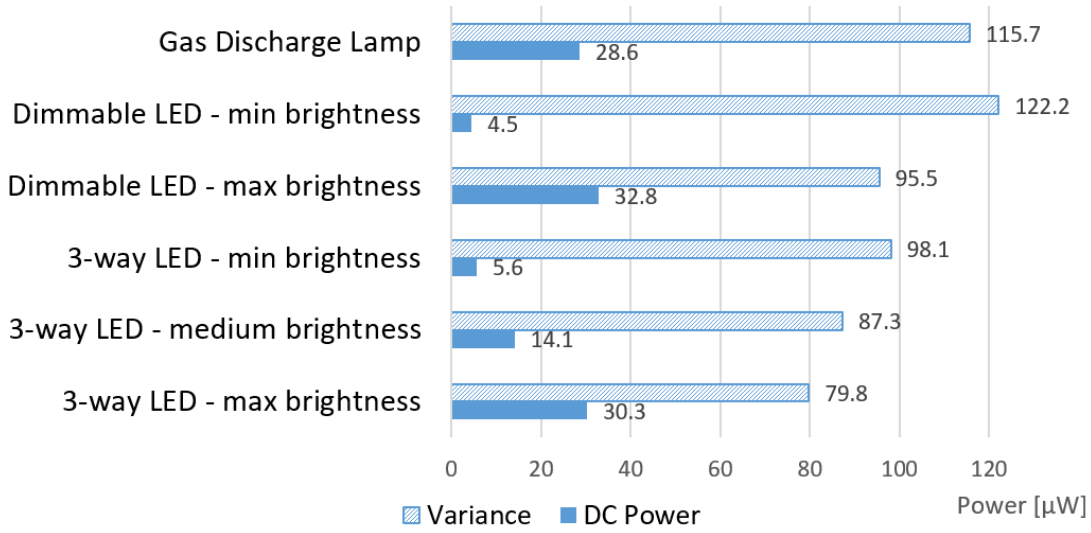

Figure 5-13: Comparison of tested ambient light sources regarding their variance and DC power [27]

The incandescent light bulb has the highest DC power, almost 10 times larger than the average power dissipated by all the other light sources. However, its significant bandwidth is only limited to 100 Hz with the least number of harmonics, which makes it easy to eliminate its effect using a filter with cut-off frequency above 100 Hz. This 100 Hz are mainly due to the switching circuit. The DC power from the other light sources is compared in Figure 5-13. It shows that they do not vary much in their emitted light power, measured at 1 m distance from the respective source. The figure shows the dimmable LED at minimum brightness has the highest variance and the lowest DC power.

The following section employs those measurements to propose an interference mathematical model for each of the tested ambient light sources.

5.4. Interference Mathematical Model

Based on the measurements, an interference model is derived to represent the power penalty of each light source on the VLC spectrum. It is important to mention here that the interference mathematical model presented in this section refers only to the specific light sources that have been tested in this chapter and cannot be generalised to other contemporary light sources that are made by other manufacturers or that employ different lighting technologies.

The optical power $P_o(t)$ received by the photodetector of a VLC system due to the interfering ambient light sources consists of a DC background power P_B and a time-varying interference power component $P_{\text{interf}}(t)$ due to the power fluctuations as indicated by the following equation [17], [115]:

$$P_o(t) = P_B + P_{\text{interf}}(t)\,. \tag{5.7}$$

The effect of this power on the receiver end is threefold: Firstly, it generates a background shot noise component $P_{B\_\text{shot\_noise}}$ due to the constant DC background power P_B. Secondly, $P_{\text{interf}}(t)$ is itself an interference component detected by the photodetector of the VLC system. Thirdly, this time-variant power component produces a time-varying interference shot noise $P_{\text{interf\_shot\_noise}}(t)$. Hence, the overall noise power $P_{\text{noise}}(t)$ detected by the photodetector can be written as [59]:

$$P_{\text{noise}}(t) = P_{B\_\text{shot\_noise}} + P_{\text{interf}}(t) + P_{\text{interf\_shot\_noise}}(t). \tag{5.8}$$

$P_{\mathrm{B\_shot\_noise}}$ (which is equivalent to its variance) can be written in terms of the responsivity $R(\lambda)$ and bandwidth BW_{3dB} of the photodetector according to equations (5.3) and **Error! Reference source not found.** as follows [111]:

$$P_{B\_\mathrm{shot\_noise}} = 2e \times R(\lambda) \times P_B \times BW_{3dB} \,. \tag{5.9}$$

The same applies to the interference shot noise power, assuming there is a closed-form formula that can represent it. Hence, the Fourier series - which is used to represent any deterministic and periodic signals as a sum of sin and cos components of different amplitudes, phases and frequencies - is employed to represent the power signals of each of the light sources. The power signal of the light sources can hence be written as follows:

$$P_{\mathrm{interf}}(t) = a_0 + \sum_{i=1}^{i_{\max}} (a_i \cos(2\pi(100i - 50)t) + b_i \cos(2\pi(100i)t)) \,, \tag{5.10}$$

where a_0 is the average DC value of the power, a_i is the magnitude of the i^{th} 50 Hz harmonic, b_i is the magnitude of the i^{th} 100 Hz harmonic and $i_{\max}$ is the number of the last significant harmonic in the frequency spectrum for each light source. The values of a_0, a_i, b_i and $i_{\max}$ are empirically determined from the measured power signals. They are summarised in Table 5-1 for the interference sources under test.

To validate the resulting mathematical interference model, the derived Tungsten light bulb mathematical model is compared with that of the Tungsten filament lamp published in [63]. Similar to the results presented in this chapter, the tested 60 W Tungsten filament lamp in [63] has a significant bandwidth of just 100 Hz due to its driving circuit. Higher modulation harmonics are insignificant and present only white noise that can be filtered out [63]. This matches the results for

the measured power of the Tungsten light bulb under test in this chapter and validates therefore the methodology used to determine the mathematical interference model for contemporary light sources.

For the interference sources driven by an electronic ballast, such as fluorescent lamps, the mathematical model should be modified to take the high frequency components due to the ballast driver into consideration. In this case, the interference optical power consists of two components:

$$P_{\text{interf}}(t) = P_{\text{interf\_low}}(t) + P_{\text{interf\_high}}(t)\,, \tag{5.11}$$

where $P_{\text{interf\_low}}(t)$ is the low frequency component and $P_{\text{interf\_high}}(t)$ is the high frequency component. Each of those terms is separately converted to its Fourier series form. While the low-frequency component has periodic components over the bandwidth of the interference spectrum, the high-frequency components are at random frequencies and have random amplitudes according to the manufacturing process of the light source [67].

Table 5-1: Parameter values for the Fourier Series of light sources under test [27]

Light Source	i	a_i (µW)	b_i (µW)	P_B
Thermal light source	1	0	4.1	1004.25
Gas discharge lamp	1	0.001648	0.028697	28.6
	2	0	0.0022	
	3	0	0.000336	
	4	0	0.000173	
	5	0	8.55E-05	
3-way LED – maximum	1	0.000281	0.004322	30.3
3-way LED – medium	1	0.000166	0.000148	14.06
3-way LED – minimum	1	0.001709	0.000145	5.58
	2	1.15E-05	2.32E-05	
	3	0	3.7E-06	
	4	1.19E-05	6.28E-06	
	5	8.09E-06	0	
	6	0	3.97E-06	
	7	4.17E-06	0	
	8	4.25E-06	0	
	9	3.76E-06	0	
	10	3.63E-06	4.55E-06	
Dimmable LED – maximum brightness	1	0.001702	0.204405	32.8
	2	0	0.001878	
Dimmable LED – minimum brightness	1	0.001876	0.005158	4.5
	2	1.03E-05	0.000911	
	3	9.67E-05	0.000328	
	4	9.43E-06	0.000119	
	5	1.93E-05	3.44E-05	
	6	8.24E-06	1.01E-05	
	7	0	3.14E-06	
	8	6.9E-06	2.09E-06	
	9	0	1.89E-06	
	10	3.5E-06	8.91E-06	

Table 5-2: Parameter values for high frequency component of the fluorescent light bulb [27]

i	c_i	f_i
1	8.91E-05	3.7 kHz
2	0.001804	5 kHz
3	0.000183	8.4 kHz
4	0.000191	8.5 kHz
5	0.00031	8.65 kHz
6	0.000296	8.8 kHz
7	0.207072	10 kHz
8	0.002056	20 kHz

The high frequency component of the interference power is hence written as:

$$P_{\text{interf\_high}}(t) = \sum_{i=1}^{\infty} c_i \cos(2\pi f_i t), \tag{5.12}$$

where c_i is the amplitude and f_i is the frequency of each peak in the spectrum, respectively. Those values are given in the Table 5-2 for the tested fluorescent light source [27].

The tree diagram in Figure 5-14 on the next page summarises the effect of each of the tested ambient light sources on the VLC channel. The green nodes are the ambient light sources tested while the red ones highlight the spectrum of their respective interference.

Figure 5-14: Tree diagram of the contemporary ambient light sources and their interference spectrum bandwidth

5.5. Conclusion

Two major factors affecting the performance of a VLC link are noise and interference. The noise in a VLC system is either thermal due to the electrons movement in the detection device or shot noise due to the fluctuations of the photon numbers incident on the photodetector surface. Interference on the other hand is due to ambient light sources that are geographically located near the VLC system and are not part of it. Those ambient light sources are either natural and considered constant in time, such as the sun, or artificial light sources that emit time-varying power. Modern and contemporary light sources are either thermal, gas discharge or semiconductor-based light sources. In this chapter, the interference power of each type is measured, and a mathematical model is developed to represent their interference power on the VLC system at a constant distance of 1 m.

Now that the noise and interference on the VLC system have been investigated in this chapter, the next chapter considers characterising the LED as transmitter and receiver of the LED-to-LED communication system.

Chapter 6

Performance Analysis of the Proposed Low-complexity LED-to-LED Communication System

6.1. Introduction

Based on the findings about the LED as emitter and photodetector and the proposed design of the transmitter and receiver circuits, this chapter practically characterises an LED-to-LED communication link employing off-the-shelf RGB LEDs. The implemented link offers reduced cost and complexity by being stripped of all complicated circuitry, optics and processing-hungry techniques. By depending only on off-the-shelf components, the overall cost is kept as low as $2.60 per communicating device (at the time of this writing). The practical results show that the link can reach up to 200 kbps data rates with OOK modulation at distances up to 7 cm when an optimised matched filter is employed at the output.

6.2. Experimental Setup

As discussed in the previous chapter, the red sub-LED has the smallest energy gap, the largest photodetection bandwidth and the highest responsivity to the visible light spectrum. It is therefore best optimised for the use as a photodetector [33], [34]. On the other hand, the green sub-LED is best suited for transmitting a signal because it offers the high brightness and intensity at the same forward bias [34]. Hence, these sub-LEDs are employed for transmitting and receiving, respectively.

The block diagram of the experimental setup is shown in Figure 6-1.The green sub-LED on the emitter side is driven by the current-mirror LED driver designed in chapter 4, that operates at 5 V [66]. The LED is biased at 19 mA, which keeps the energy consumption at a minimum and allows fast on-off switching of the transmitter LED. An arbitrary waveform generator is programmed to feed the LED driver with an on-off-keying (OOK) modulated cyclic and independent pseudorandom binary sequence (PRBS) of length 2^{20}-1 bits [34].

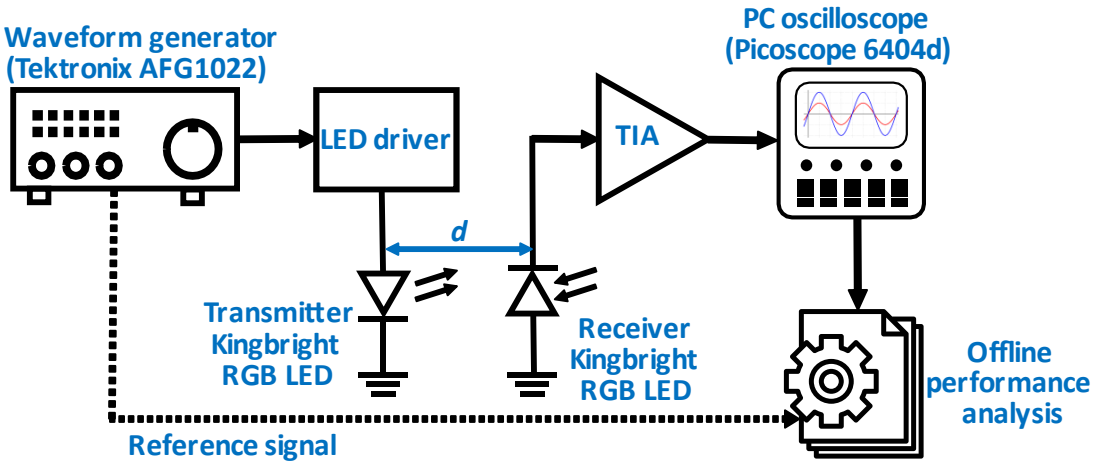

Figure 6-1: Block diagram for experimental testing of proposed LED-to-LED link parameters [34]

The sequence is generated using linear feedback shift registers applying the monic polynomial [117]:

$$\mathrm{PRBS20} = x^{20} + x^3 + 1\,. \tag{6.1}$$

To ensure that the PRBS bits are statistically independent, the autocorrelation function of the sequence has been calculated. It shows a maximum correlation is achieved at position $x = 0$ and zero correlation elsewhere. The PRBS sequence is sent at 10 kbps, 50 kbps, 100 kbps and 200 kbps.

The modulated light propagates along the free-space channel to the receiver. The channel length d is varied to evaluate the effect of the propagation distance on the link performance. At the receiver end an identical RGB LED (to the transmitter) is connected to the TIA receiver circuit (shown in Figure 6-2 as per the design in chapter 4). For comparison purposes, the receiving LED is replaced with a PIN photodiode (BPW34 Vishay Semiconductors) [118] under the same measurement conditions [34].

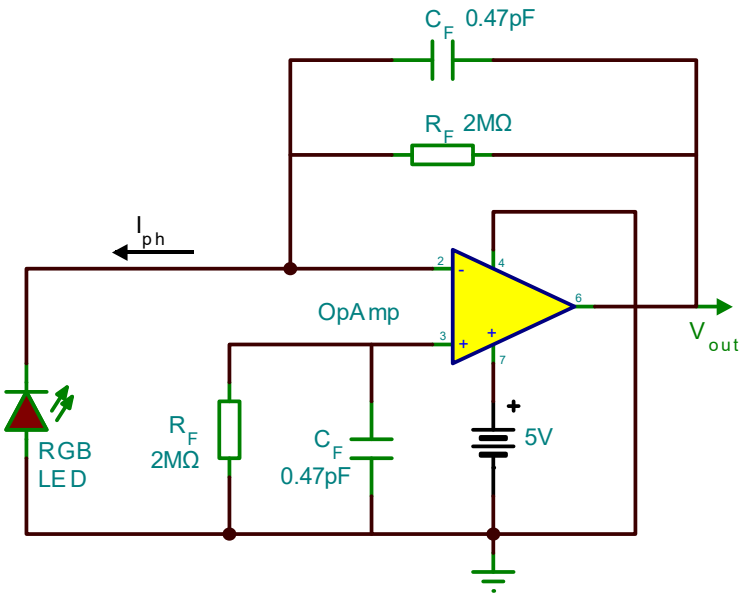

Figure 6-2: TIA circuit in photovoltaic mode employed as receiver [34]

As discussed in the chapter 3, reverse biasing the LED has only a negligible effect on improving its bandwidth and sensitivity [34], [97]. Unlike the PIN photodiodes - which depend on the presence of a large reverse bias to function - an LED can operate at no bias and even at a small forward bias. Hence, the photovoltaic mode is chosen for the detection circuit in conjunction with the LED photodetector. The output of the TIA, the eye diagram of the received signal and the reference signal from the waveform generator are displayed on an oscilloscope (Picoscope 6404D) and saved for offline processing.

Care has been taken to choose components which are cheap and available off-the-shelf. The price for the RGB LED, the transistor for the LED driver, the OpAmp and the accompanying resistors and capacitors add up to only $2.60. Moreover, the system design uses only a single 5 V power supply and consumes only a maximum of 110 mW. The low price and power consumption are attractive features for IoT device manufacturers and mass producers.

The pictures in Figure 6-3 show the LEDs arrangement in the experimental setup for testing the system performance.

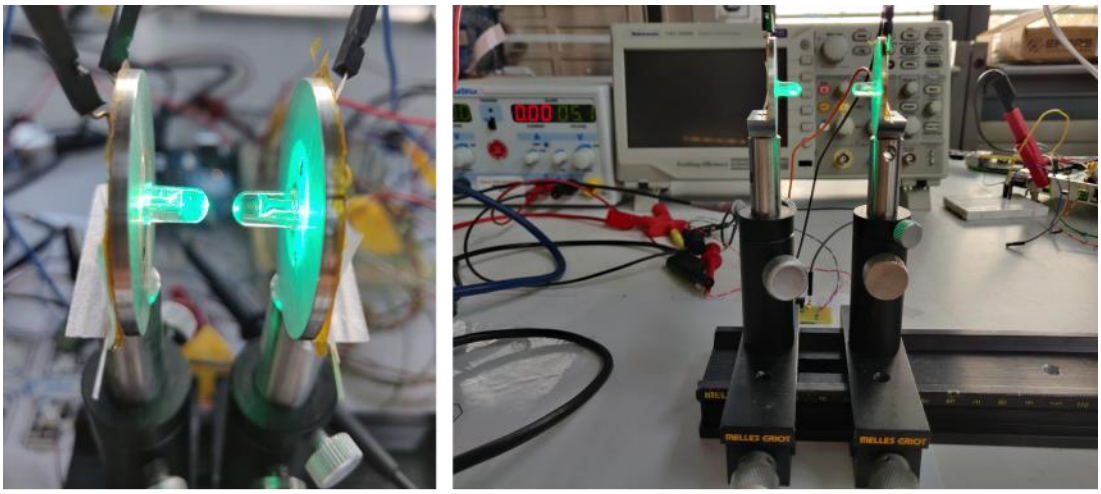

Figure 6-3: Pictures of the practical setup for testing the LED-to-LED communications system

The experiments take place in a lab with typical ambient light to simulate real life conditions. The present ambient light sources are placed on the ceiling and their emitted light beams were perpendicular to the transmission direction of the LED-to-LED system under test. Since the LED photodetector has a low responsivity, sensitivity and a small acceptance cone, the detection is not affected by the presence of the light sources present in the lab. Their effect is therefore neglected. To evaluate the performance of the system without the interference effect from the neighbour sub-LEDs, only the transmitter sub-LED is switched on during transmission while the others are turned off. The presented results are the average of a series of measurements to eliminate any outliers due to human or equipment error [34].

6.3. BER Measurement

The BER is measured using two methods:

The error bits are deduced from the generated PRBS20 bits to calculate the BER as per the following relation:

$$\mathrm{BER} = \frac{\text{error bits}}{\text{total number of bits}}. \tag{6.2}$$

In order to verify the practically measured BER results, the BER is also calculated via the quality factor (Q-factor) obtained from the captured eye diagram. The Q-factor determines the quality of the signal with respect to the signal-to-noise ratio (SNR) and can be calculated from the parameters of the eye diagram as follows [119], [120]:

$$Q = \frac{|\mu_1 - \mu_0|}{\sigma_1 + \sigma_0}, \tag{6.3}$$

where μ_1 and μ_0 are the mean voltages and σ_1 and σ_0 are the standard deviation values of the '1' and '0' rails due to the AWGN, respectively. This formula is a good measure for the system margins if the modulation scheme is OOK, if the added noise has a Gaussian (Normal) distribution and when the inter-symbol interference is negligible with respect to the noise [121]. These conditions apply to the proposed LED-to-LED communication link.

Hence, the BER can be calculated using the following relation [120], [121]:

$$\mathrm{BER}(V_{th}) = \frac{1}{2}\left[\mathrm{erfc}\left(\frac{|\mu_1 - V_{th}|}{\sigma_1}\right) + \mathrm{erfc}\left(\frac{|V_{th} - \mu_0|}{\sigma_0}\right)\right], \qquad (6.4)$$

where V_{th} is the threshold voltage and determines where the decision is made. In this scenario it is taken as the centre rail between the '0' and '1' voltage rails. For all considered data rates and distances between 0 and 10 cm at 0.5 cm steps, the probability density function (PDF) for the one and zero rails, respectively, is drawn.

The histograms for 0 and 10 cm at 10 kbps are depicted in Figure 6-4 (a) and (b), respectively. The red Gaussian curve is derived from the histogram data as the equivalent normal distribution of the noises in both rails. The R2 value measuring the closeness of the normal distribution fit to the real data is calculated for each of the four drawn curves. It is found to be 0.993 and 0.959 for the '0' and '1' rails in the back-to-back configuration in Figure 6-4 (a) and 0.976 and 0.982 for the '0' and '1' rails in the 10 cm setup in Figure 6-4 (b), respectively. The parameters for calculating the Q-factor and BER are extracted from the Gaussian distribution function and are displayed on their respective graphs. For the back-to-back case in Figure 6-4 (a) the two rails of the signal are distinct and far away from each other, allowing a right decision to be taken with V_{th} at the center. This agrees with the wide eye opening in the same figure. On the contrary, this distinction vanishes in the signal constellation at 10 cm distance in Figure 6-4 (b) where the normal distribution functions of the '0' and '1' rails are overlapping. In agreement therewith, the eye is closed, which corresponds to a higher probability of error [34].

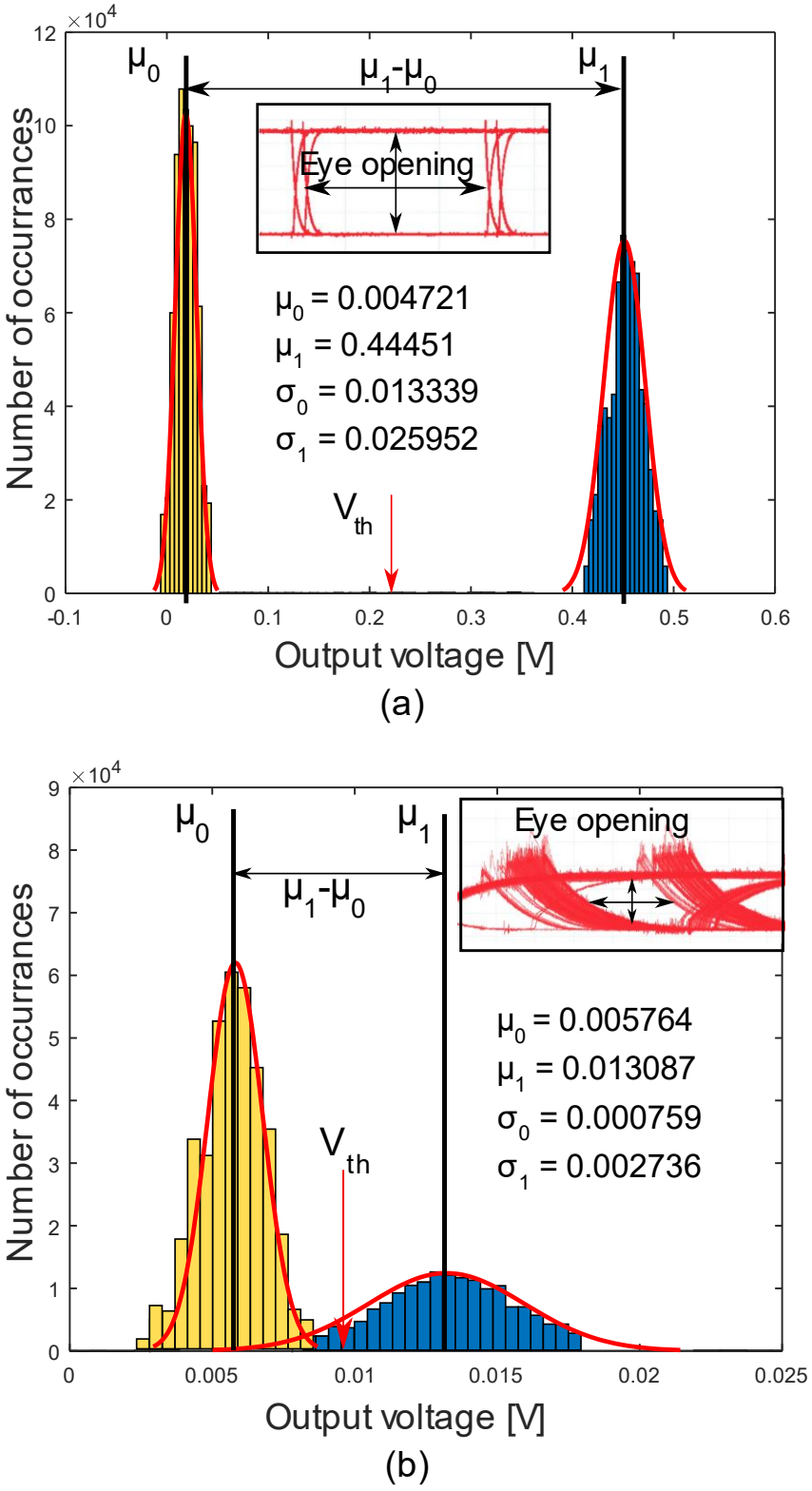

Figure 6-4: Eye diagram (inset) and signal constellation at 10 kbps data rate (a) in back-to-back configuration and (b) at 10 cm distance [34]

The comparison between the measured BER results employing equation (6.2) and the calculated BER from equation (6.4) at 10, 50, 100 and 200 kbps are shown in Figure 6-5. The graph verifies that both approaches have similar responses. The measured and calculated BER show a maximum average deviation of only 9% from each other for all data rates. This validates the practical approach [34].

As expected, the BER rises with longer transmission distance and higher data rate. Error-free data reception can be achieved at a maximum distance of 1 cm at 200 kbps, 1.5 cm at 100 kbps, 2 cm at 50 kbps and it reaches 3 cm at 10 kbps. The BER stays below the accepted 10^{-3} range [31] up to 7 cm for 10 and 50 kbps, up to 4 cm for 100 kbps and up to 3 cm for 200 kbps. This shows that the sensitivity of the LED as photodetector is low even after only a very short distance [34].

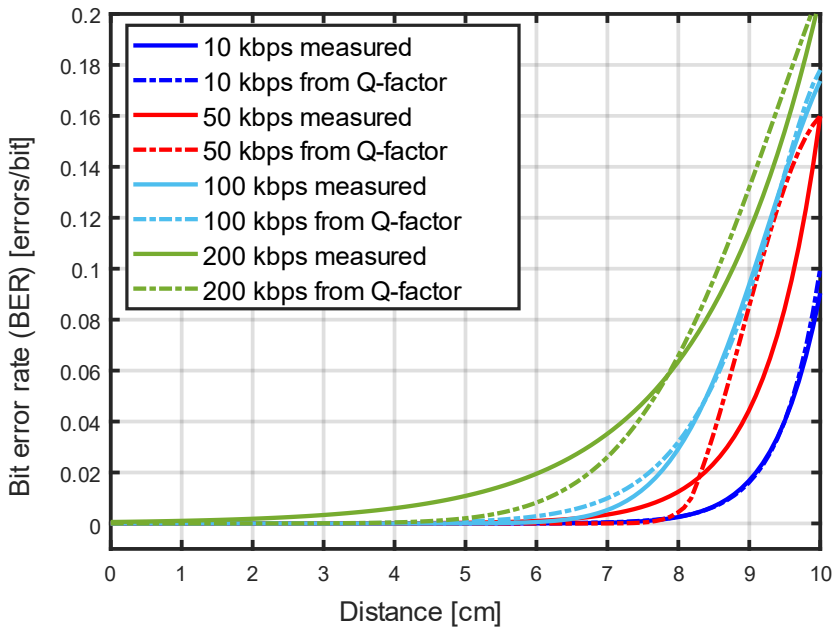

Figure 6-5: BER measured (solid line) and calculated from Q-factor (dashed line) for all tested data rates [34]

6.4. Signal-to-Noise Ratio Analysis

The signal-to-noise ratio (SNR) can be determined from the BER of the non-return-to-zero on-off-keying (NRZ OOK) modulation as follows [122]:

$$\mathrm{BER} = \frac{1}{2}\mathrm{erfc}\left(\frac{1}{2\sqrt{2}}\sqrt{\mathrm{SNR}}\right), \tag{6.5}$$

where erfc is the complementary error function. The graph in Figure 6-6 compares the BER and the SNR for the LED-to-LED communication link at different distances for data rates of 10, 50, 100 and 200 kbps. As expected, the SNR decays exponentially along the distance and at higher speeds [34].

This is mainly due to the fact that an RGB LED has a much smaller active area for light emission and detection per sub-LED compared to a regular single-colour LED.

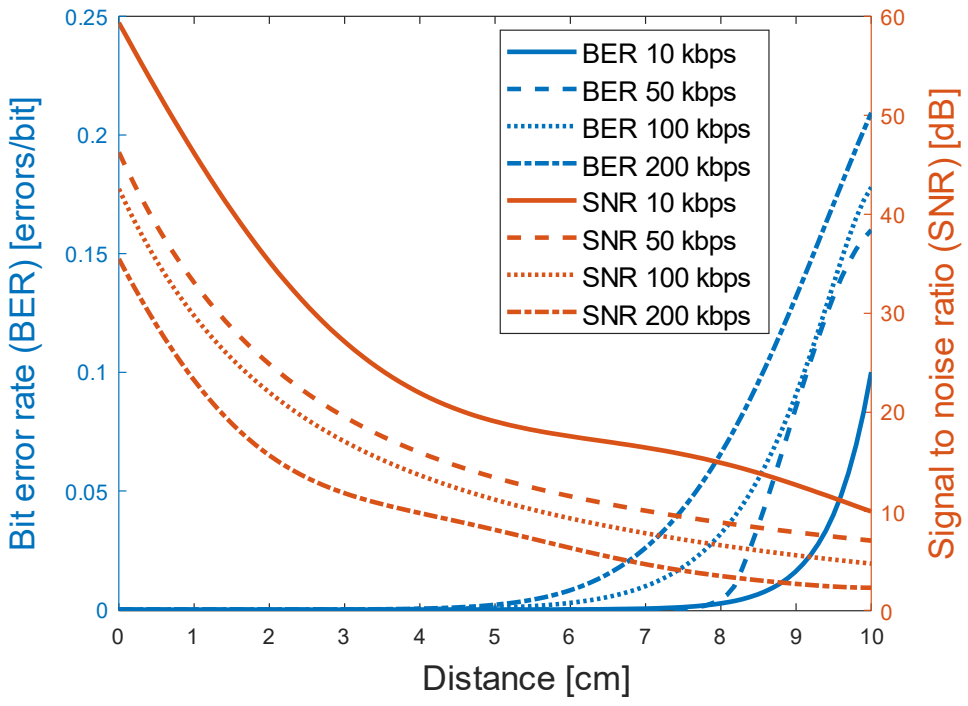

Figure 6-6: BER and SNR for the tested data rates at varying distances

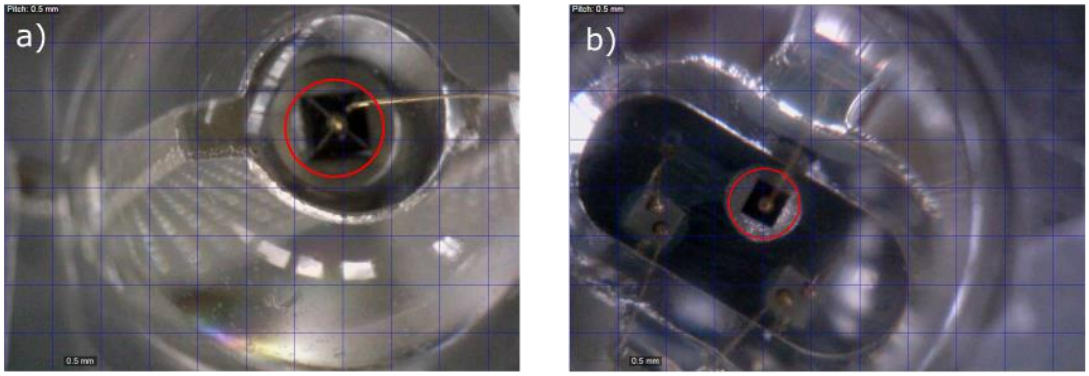

Figure 6-7: Images of the active areas of (a) single colour red LED and (b) red sub-LED from an RGB LED when placed under the microscope under the same scale [34]

This is apparent after placing both LEDs under a USB microscope in our laboratories and comparing their active areas as shown in the magnified images in Figure 6-7. To make the decision, how large the active area is, the LEDs are fed with only 1 mA of current using a Laser Driver instrument (Arroyo Instruments 4302). The active areas are considered to be the dimly illuminated areas seen under the microscope. These are circled in red respectively in Figure 6-7. Comparing both LEDs relative to the 0.5 mm x 0.5 mm grid in both images under the same magnification factor, the active area of the single-colour LED is 1.99 times larger than that of the sub-LED of the RGB LED. This translates roughly to being able to capture only 50% of the incident light compared to the single-colour LED. Therefore, it is recommended to use appropriate lenses to concentrate the incident light power on the active area of the LED photodetector in order to enhance the performance of the RGB LED-based LED-to-LED communication system. Moreover, it can be concluded that the small data rates achieved by this small-area LED photodetector can be interpolated to match the higher data rates achieved in Stepniak's research [33] [34].

6.5. Optimisation of LED-to-LED system performance

The performance of the tested LED-to-LED link lags due to the high noise caused by the LED photodetector. This noise has been characterised and found to be additive white Gaussian noise in the previous chapter. This AWGN generated by the LED photodetector requires a maximum likelihood receiver to mitigate its effect and improve the BER of the LED-to-LED communication link. The matched filter technique is a special type of maximum likelihood receivers which is known to maximise the signal to noise ratio of a received signal suffering from white Gaussian noise [38]. Hence, an optimised matched filter is proposed that improves the system performance and achieves error-free transmission over 7 cm distance at 10 kbps and 4 cm distance at 200 kbps [34].

6.5.1. Derivation of Matched Filter Technique

The block diagram in Figure 6-8 demonstrates a typical digital communication system. The additive white gaussian noise $n(t)$ is added to the original signal $s(t)$. The combined signal is passed through a filter $h(t)$, whose outcome $y(t)$ is sampled every bit duration T_b. The sampled signal $y(T_b)$ is compared to a threshold value V_{th} in a comparator, which makes the decision to produce a logic bit '0' or '1'.

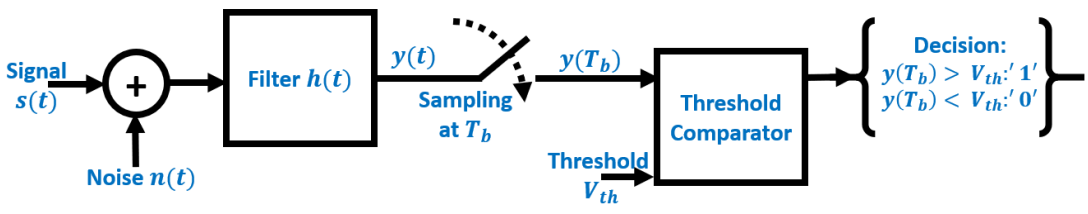

Figure 6-8 : Block diagram of a typical digital communication link [34]

In order to minimise the BER of the system, the SNR needs to be maximised at the comparator stage. The main purpose of using a filter here is to maximise the signal to noise ratio of the system. At the input point of the threshold comparator block, the AWGN power N_p can be derived in terms of the its power spectral density PSD, which is equal to $\frac{N_0}{2}$. The following equation represents this relation [122]:

$$N_p = \int_{-\infty}^{\infty} \mathrm{PSD}\, df = \frac{N_0}{2} \int_{-\infty}^{\infty} |H(f)|^2\, df\,, \tag{6.6}$$

where $H(f)$ is the transfer function of the filter.

Similarly, the following equation displays the power of the signal S_p at the input of the threshold comparator block:

$$S_p = |y(T_b)|^2 = \left| \int_{-\infty}^{\infty} S(f)H(f)e^{-j2\pi f T_b} \right|^2. \tag{6.7}$$

Dividing the signal power by the noise power to get the signal to noise ratio:

$$\mathrm{SNR} = \frac{S_p}{N_p} = \frac{\left| \int_{-\infty}^{\infty} S(f)H(f)e^{-j2\pi f T_b} df \right|^2}{\frac{N_0}{2} \int_{-\infty}^{\infty} |H(f)|^2\, df}. \tag{6.8}$$

This SNR value should be maximised. So, Schwarz inequality is employed, which states that for any two functions $f_1(t)$ and $f_2(t)$, the following relation is true:

$$\left| \int_{-\infty}^{\infty} f_1(t) f_2(t) dt \right|^2 \leq \int_{-\infty}^{\infty} |f_1(t)|^2 dt \cdot \int_{-\infty}^{\infty} |f_2(t)|^2 dt\,. \tag{6.9}$$

This Schwarz inequality holds only when the functions f_1 and f_2 are conjugates of each other, such that:

$$f_1(t) = {f_2}^*(t)\,. \tag{6.10}$$

Applying Schwarz inequality to the SNR equation and considering f_1 to be $H(f)$ and f_2 to be $S(f)e^{-j2\pi fT_b}$, the following equation for the SNR is derived:

$$\frac{S_p}{N_p} \leq \frac{\int_{-\infty}^{\infty}|H(f)|^2 df \cdot \int_{-\infty}^{\infty}\left|S(f)e^{j2\pi fT_b}\right|^2 df}{\frac{N_0}{2}\int_{-\infty}^{\infty}|H(f)|^2\, df}, \tag{6.11}$$

$$\frac{S_p}{N_p} \leq \frac{2}{N_0}\int_{-\infty}^{\infty}|S(f)|^2 df\,, \tag{6.12}$$

where $\int_{-\infty}^{\infty}|S(f)|^2 df$ is the energy of the bit signal and can be therefore written as E_s. Hence, the signal to noise ratio can be expressed as:

$$\frac{S_p}{N_p} \leq \frac{2}{N_0}\,E_s\,. \tag{6.13}$$

According to Schwartz inequality, to maximise the signal to noise ratio the function of $H(f)$ must be equal to the conjugate of $S(f)e^{-j2\pi fT_b}$. Hence:

$$h(t) = \; s^*(T_b - t)\,. \tag{6.14}$$

This means that the filter transfer function should have the exact shape and size of the logic '1' bit. In the case of the proposed experiment, this translates to a square-shaped signal of magnitude 4.5 V and duration T_b. Because the filter transfer function and the input signal are identical to each other, this filter is called a matched filter.

In case of a logic '1' bit being transmitted as $s(t)$, the output of the matched filter is a triangle of base width $2T_b$, with a peak at T_b of magnitude E_s. Hence, the maximum output is achieved when the sampling is done at T_b intervals. This corresponds to the peak of the triangular wave [34].

6.5.2. Measurement of System Performance with Matched Filter

Figure 6-9 shows the block diagram of the system after the matched filter is employed. At the receiver side, the matched filter is placed at the output of the TIA, where the generated photocurrent along with the noise generated by the LED photodetector are amplified. The output of the matched filter is then stored to be analysed. The system performance in terms of BER, SNR and maximum error-free transmission distance is compared with and without matched filter to determine its improvement [34].

The matched filter is created by first filtering the received signal to reduce the noise using a Butterworth bandpass filter, which is known to have a maximally flat response in the pass band. The filtered signal is then convolved with the step function of width T_b resembling logical bit '1' [34].

The result of this convolution consists of sawtooth and rectangular shaped signals, from which the logical levels '1' and '0' can be derived after sampling at a rate of T_b and comparing with a threshold that is equal to the mean of the convolved signal.

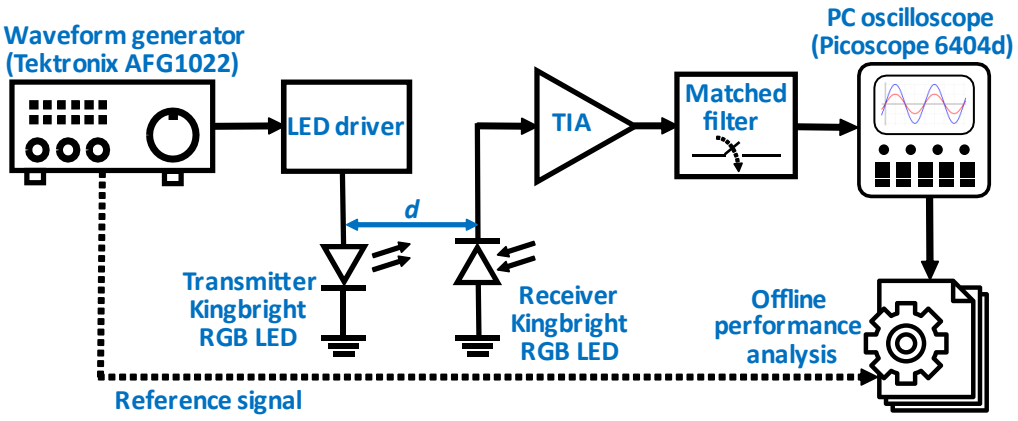

Figure 6-9: Block diagram of experimental setup with inclusion of a matched filter at the receiver side [34]

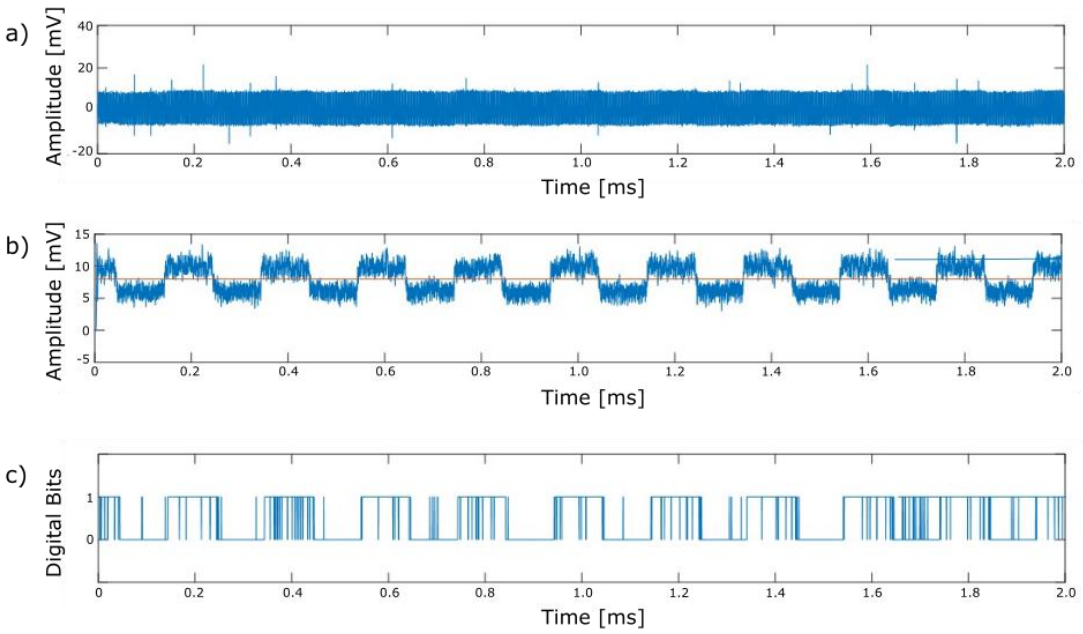

Figure 6-10: Output of the matched filter stages

Figure 6-10 shows an example of the stages in the matched filter post processing technique taken at data rate 10 kbps at a distance of 7 cm. Figure 6-10 (a) shows the received noisy signal when a square wave is sent from the transmitter LED. The graph shows that due to the high noise component, the '0' and '1' bit are not recognisable. Figure 6-10 (b) is the outcome of the Butterworth bandpass filter along with the threshold level used by the comparator (marked as a red line). Figure 6-10 (c) shows the output of the comparator without the use of matched filter. It can be seen from this graph that due to the low SNR the system is prone to errors if the matched filter is omitted [34].

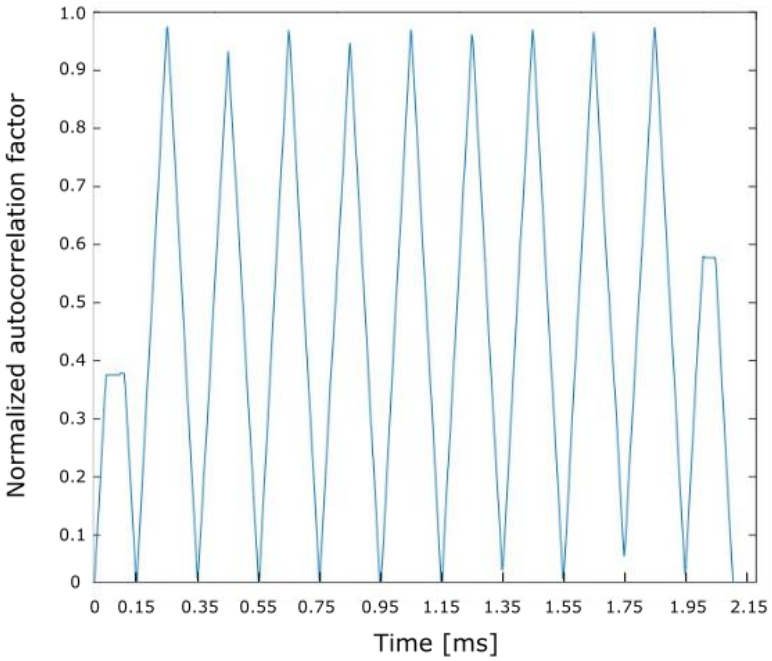

Figure 6-11: Output triangular waves from the matched filter with peaks at every T_b for correct sampling

Figure 6-11 displays the outcome of the matched filter after the convolution with the expected signal for bit '1'. As expected with a square wave input, the output consists of a triangular wave of 2 T_b period with minimum and maximum peaks at T_b intervals, where the sampling and comparing occurs, allowing therefore an error-free decision making.

By employing the matched filter as post processing technique, the BER at every speed and distance is decreased. The error-free distance between transmitter and receiver is thereby increased. Figure 6-12 compares the BER at 10, 50, 100 and 200 kbps with and without matched filter. At all data rates, applying the matched filter technique reduces the BER by 40% to 90%. For example, the BER at 5 cm distance is reduced from 0.0036 to 0.00034 (to less than 10%) when transmitted at data rate of 200 kbps upon applying the matched filter in the post processing phase. The most significant improvement of the matched filter technique is measured at the 200 kbps, with an improvement averaging 60% for all distances. Similarly, the matched filter technique increases the maximum error-free transmission distance for all data rates [34].

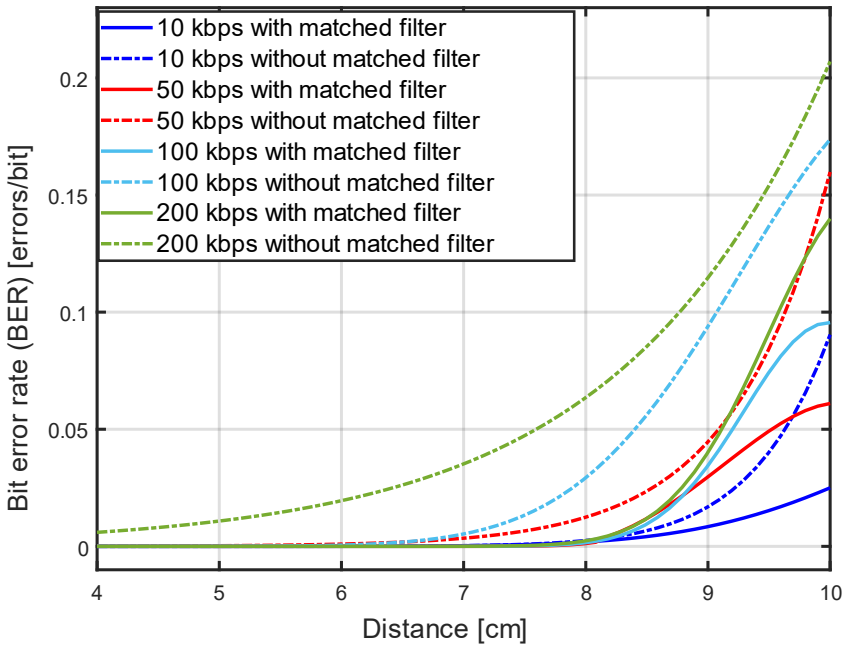

Figure 6-12: Comparison of BER at varying distances and data rates with and without matched filter [34]

Figure 6-13 compares the maximum error-free transmission distances for 10, 50, 100 and 200 kbps with and without matched filter as well as with those achieved when employing a regular PIN photodiode as photodetector. The bar chart demonstrates that applying the matched filter technique increases the error-free transmission distances for the 10 kbps transmission data rate case from around 3 cm to almost 7 cm. This matches the performance of the LED photodetector to that of a PIN photodiode. Similarly, the error-free distance is extended from 2 cm to 5 cm at 50-kbps, from 1.5 cm to 4.5 cm at 100 kbps and from 1 cm to 4 cm at 200 kbps. At 100 and 200 kbps the LED-to-LED link with matched filter exceeds the error-free transmission distance achieved by the LED-to-PIN photodiode link [34].

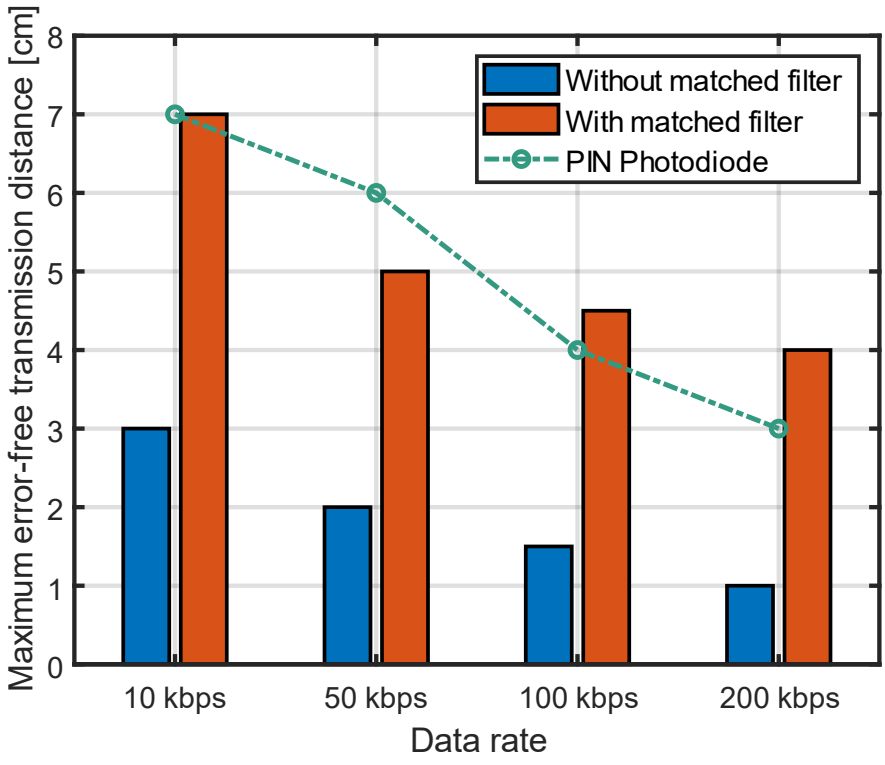

Figure 6-13: Comparison of achieved error-free distances with and without matched filter [34]

6.6. Conclusion

In this chapter the proposed low-complexity LED-to-LED link performance is characterised to determine the limitations of such a system. Employing only low-cost and off-the-shelf components, a communication link of up to 4 cm distance is implemented using the green sub-LED of an RGB LED driven by a current-mirror LED driver as emitter and the red sub-LED connected to a TIA as receiver.

The BER and SNR of the link are measured when an NRZ OOK PRBS is transmitted over varying distances up to 10 cm and with data rates up to 200 kbps. The results of the experiments reveal that successful communication with a BER under 10^{-3} can be achieved at data rates up to 10 kbps at a distance up to 4 cm. The error-free distance drops to 2 cm for 200 kbps. Due to the smaller active area of the RGB LED compared to a single-colour red LED, the LED-to-LED link does not match the performance of the more complicated designs proposed in literature [33].

To mitigate the effect of the AWGN produced by the receiver LED, an optimised matched filter is employed. This increases the system performance and matches its maximum error-free transmission distance to that of a regular PIN photodiode as detector. The results of the performed experiments prove that the BER is decreased by up to 90% at a transmission speed of 200 kbps over a distance of 5 cm.

Chapter 7

Design of a Bidirectional LED-to-LED Communication System

7.1. Introduction

One of the major objectives of this thesis is to implement a bidirectional LED-to-LED communication system that enables low-complexity small IoT devices to communicate along short distances. In order to create such a bidirectional system, a switching solution is designed in chapter 4 with the aim of switching between the transmission and detection modules (characterised in chapter 6). This enables the time-division-multiplexed bidirectional communication as well as prevents the nearby observer from detecting the flickering of the LED.

While separately characterizing the proposed switch solution in chapter 4, it was established that the switch has a distorting effect on the received signals in the “off” state due to its low attenuation factor and long fall time. In this chapter, a smart but simple algorithm is designed to regulate the timing of the transmitted

data to minimise the errors while causing only a small penalty for the overall achieved data rate. The bidirectional system is implemented and experimentally tested. It reaches an error-free data rate of up to 110 kbps in a back-to-back configuration with a switching frequency of 100 Hz and can still operate at distances up to 7 cm with switching frequencies up to 300 Hz at lower data rates.

This completes the bidirectional low-complexity LED-to-LED system that allows harnessing of the full potential of the LED to operate as a light emitter and light detector.

7.2. Design and Experimental Setup

The block diagram in Figure 7-1 depicts the experimental setup to test the performance of the bidirectional system. Two identical transceiver modules are practically implemented according to the circuit diagrams proposed in chapter 4 and tested in chapter 6. Both circuits contain a transmitter circuit (Tx), a receiver circuit (Rx), an RGB LED, an analogue switch connected to the LED and a simple microcontroller. The optimised matched filter is applied to the received signals on both ends of the channel. The identical transceiver modules are placed at a varying distance d from each other so that both LEDs are in line of sight. The uplink is marked in blue and defined as the transmission from module 1 to module 2 while the downlink is marked in green and is defined as the transmission in the opposite direction, as depicted in the figure.

For this experiment, the control signal is provided from an external trigger source to ensure that both circuits are synchronised. The control signal from the external source is fed to module 1 without change, but it must be inverted at the input of module 2. This ensures that one circuit is receiving while the other is transmitting. While feeding a control signal from an external source to both modules is not a valid option for the real-life wireless communication between IoT devices, it is sufficient for testing the circuit. In a real-life scenario, the synchronisation between the transmitting and receiving devices can be implemented using special algorithms and software such as in [91]. Then the control signal can be output from the simple processor of the IoT device itself.

The transmitted signals of both modules, the receiver output of module 2 and the control signal are measured on an oscilloscope and stored for offline analysis.

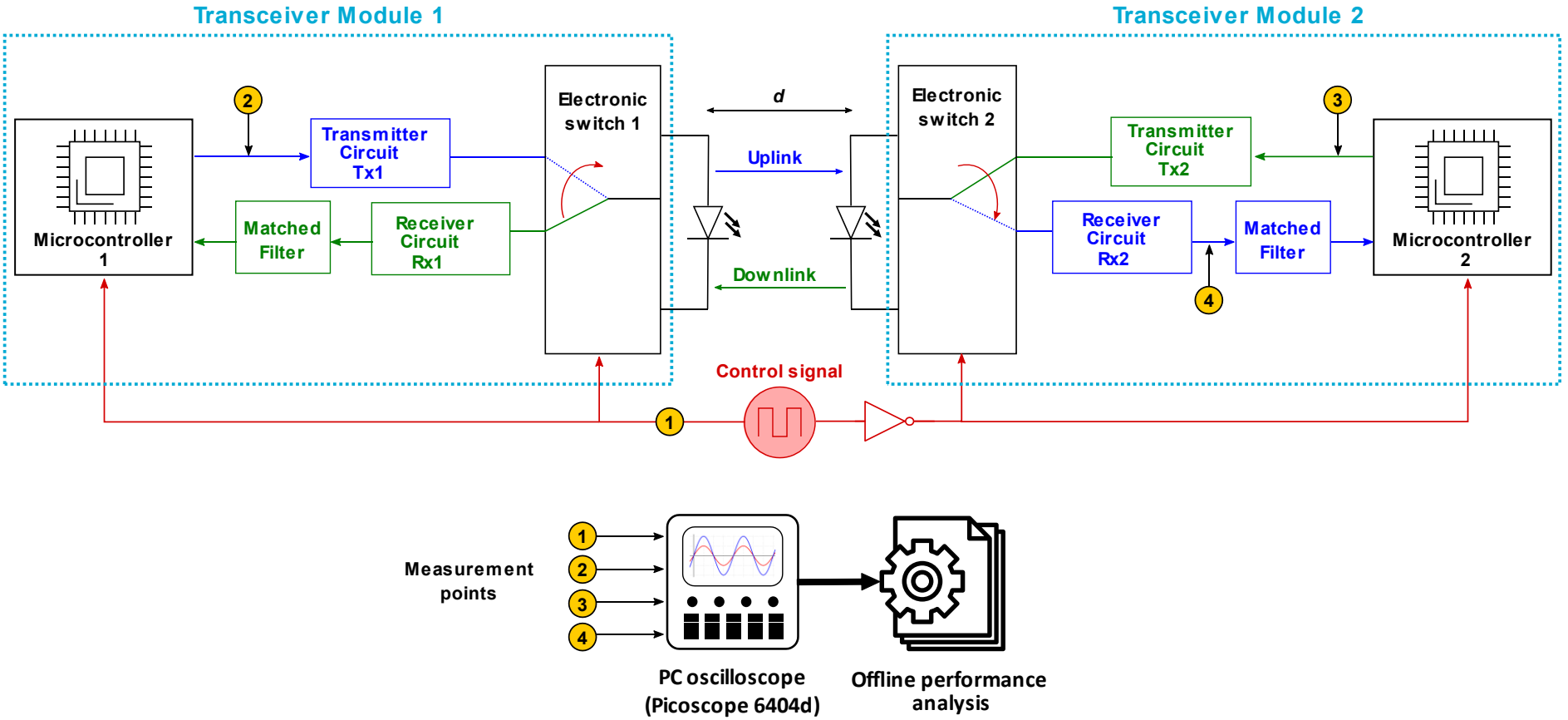

Figure 7-1:The proposed LED-to-LED communication system and the experimental setup to characterize it

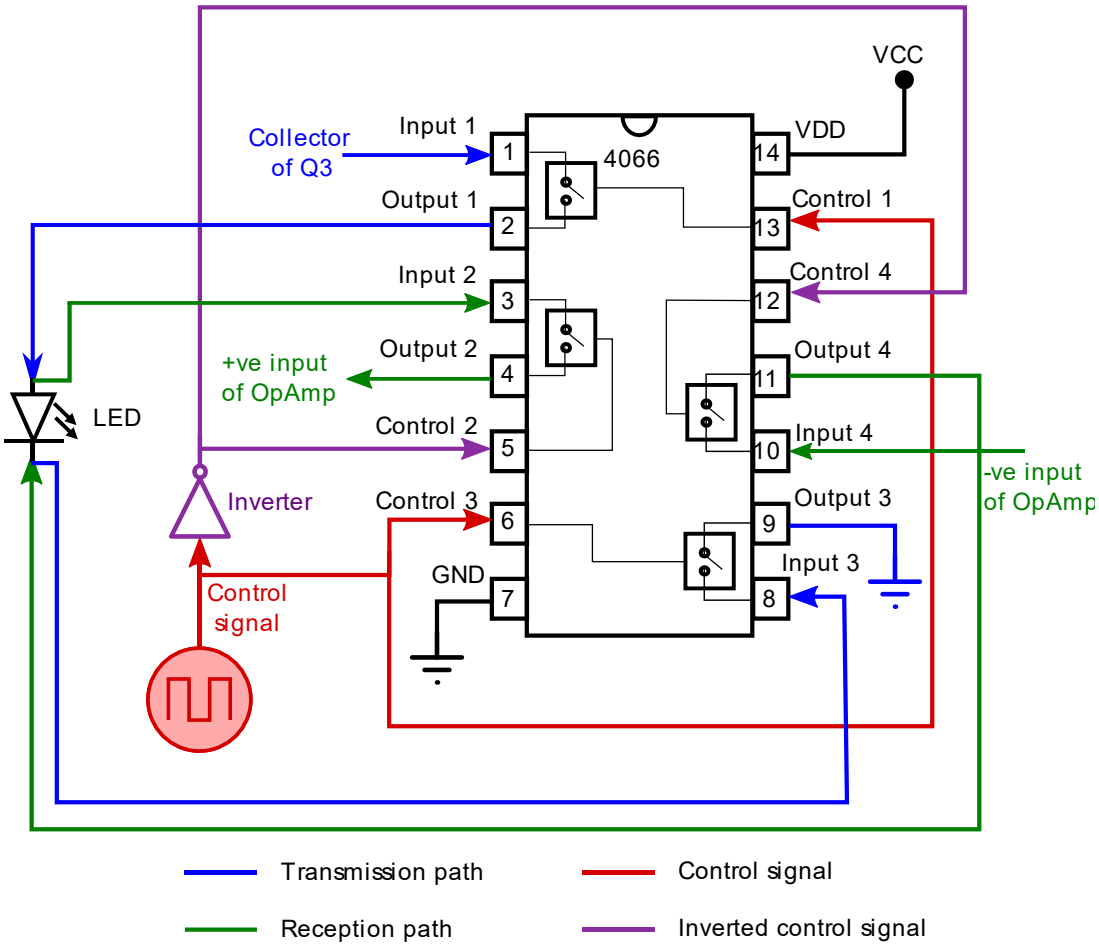

Figure 7-2: Block diagram for switching between transmitter and detector mode

The block diagram for connecting the LED pins in each module is shown in Figure 7-2. Outputs 1 and 2 are connected to the anode while outputs 3 and 4 are connected to the cathode of the LED. The inverter negates the control signal to ensure that only 2 output ports are active at a time, enabling only one path: transmission or reception. The arrows in Figure 7-2 show the direction of the signals in each path.

The measurements performed to characterise the switching IC (in chapter 4) reveal that there are drawbacks from employing the analogue switch for toggling between transmission and detection mode. These can be summarised as follows:

- The attenuation factor of the switching IC in the “off” state is not ideal, allowing up to 5% of the AC input signal as well as some of its average DC value to be transferred to the output port, as depicted in Figure 4-25. This signal might interfere with the detected signal and cause a high BER.
- The switching IC has a long fall time t_f when switching from on to off. This fall time causes baseline wandering of the attenuated transmitted signal during the detection period as seen in Figure 4-26.

To see the effects of these shortcomings on the proposed LED-to-LED link, two experiments were performed: The first is to show the effect of the bad attenuation of the transmitted signal on the received signal in the same module and the second, is to show the effect of the fall time on the received signal from the opposite module. The aim of these experiments is twofold: first they aim to evaluate the severity of the switching circuit shortcomings on the proposed system and second, to help apply an appropriate algorithm to mitigate those effects.

7.2.1. Effect of Low Attenuation in the “off”-State

To show the effect of the attenuated transmitted signal on the detector of the same module during the detection period, both Tx1 and Tx2 are turned on and set to transmit square waves of frequency 10 kHz while Rx2 is receiving as can be seen in Figure 7-3. The captured waveforms at the 4 measurement points are shown in the same figure. It can be seen from the figure that the detected waveform at Rx2 is majorly distorted due to the interference by its own transmitter signal Tx2. Instead of a clean square-wave shaped signal corresponding to the transmitted signals from Tx1, the receiver detects unexpected peaks and drops at the signal transitions of Tx2.

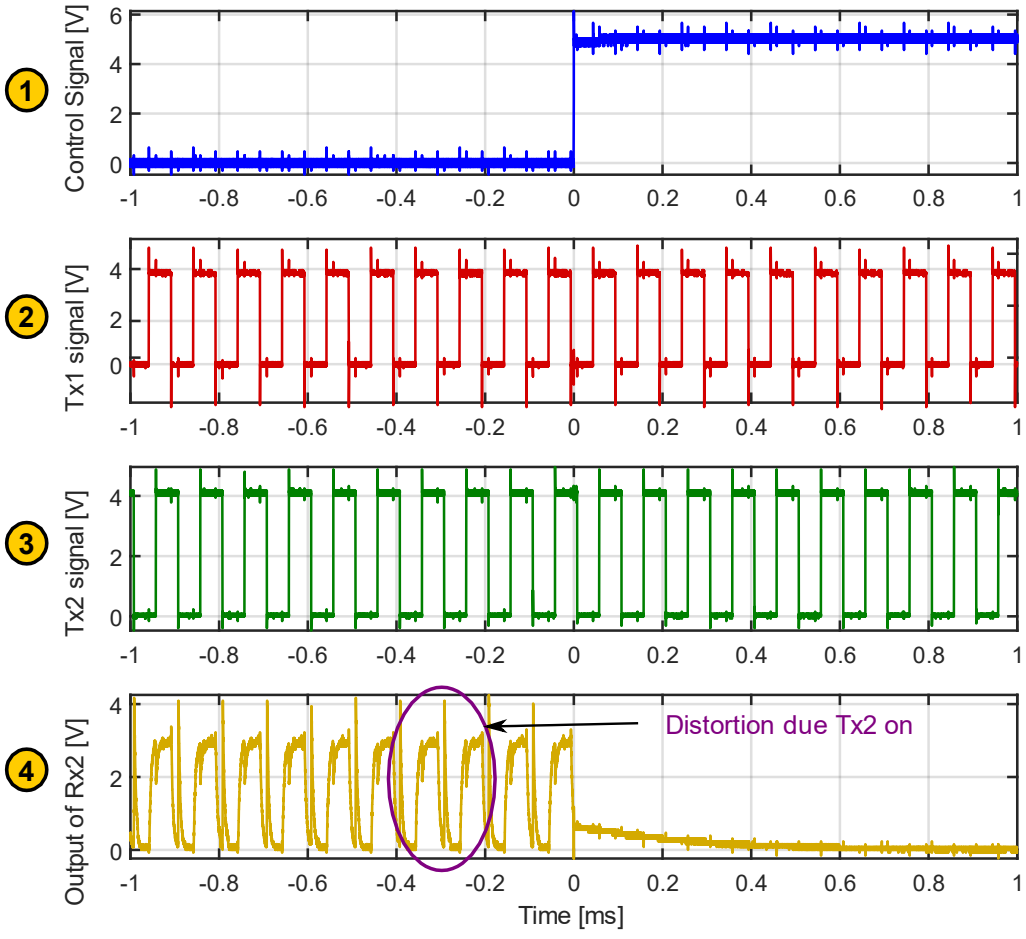

Figure 7-3: Captured waveforms showing the effect of the own transmitted signal on the detected signal when transmission is not turned off during detection

From this experiment, the following conclusion can be drawn: to avoid distortion of the received signal, the transmission of the detecting module must be completely stopped during the detection period. If the signal of Tx2 was zero, it would not interfere with the expected received signal at Rx2.

Hence, upon starting the detection period, the processor of the device should temporarily stop transmission. This means that Tx2 should be deactivated in the uplink and Tx1 should be deactivated in the downlink periods.

7.2.2. Effect of the Long Fall Time of the Switching IC

To evaluate the effect of the long fall time of the switching IC on the LED-to-LED link, Tx1 is kept on all the time and set to transmit a square wave. On the contrary, Tx2 is switched off. The control signal switches from low to high, indicating the end of the detection period of Rx2 as seen in Figure 7-4. From the detected signal of Rx2 on the figure, the distortion (circled in purple) due to the fall time of the suppressed received signal can be seen. It can be concluded that the long fall time of the switch cannot be ignored for the proposed LED-to-LED link. To mitigate this drawback of the switch, both transmission and detection of both circuits must stop completely for a period equivalent to the fall time of the switch following each transition of the control signal.

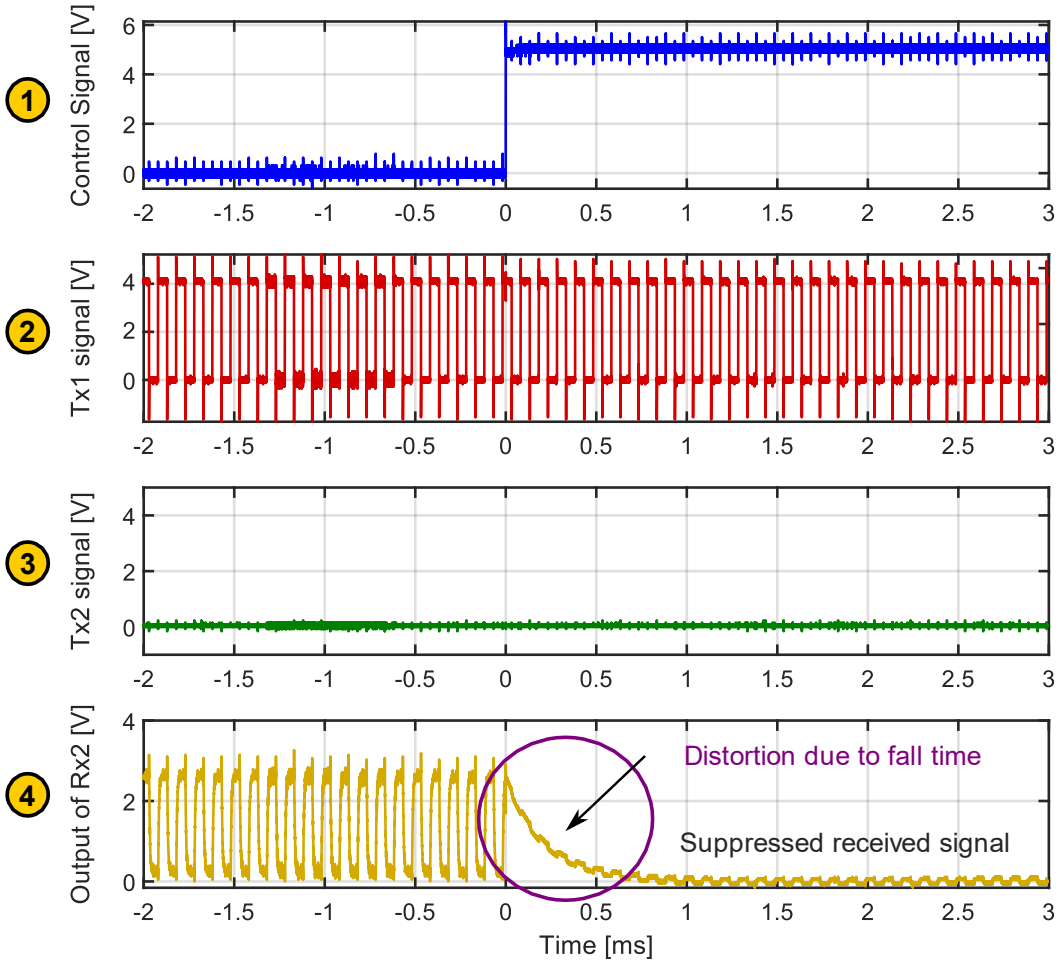

Figure 7-4: Captured waveforms showing the effect of switch long fall time

7.2.3. Timing Algorithm

To avoid transmission errors and achieve the minimum possible BER, both modules must be in synchronization and a timing algorithm should be applied to control the transmission and detection phases. The timing diagram in Figure 7-5 visually describes the effect of such an algorithm.

Firstly, it has been concluded from the experiments that the transmitter of each module should be switched off during the detection phase of the same module. This can be seen in Figure 7-5 on Tx1 and Tx2 curves during the downlink and uplink phases, respectively. Secondly, to mitigate the effect of the fall time, both transmitters should first start transmitting after a delay period equivalent to the fall time of the switch IC. This delay is marked on the Tx1 and Tx2 graphs in the timing diagram.

Similarly, the detectors should be deactivated during the transmission phase of their respective modules, i.e. Rx1 should be deactivated during uplink while Rx2 should be deactivated during downlink. Unfortunately, it is impossible to stop the LED from detecting the signal during transmission time or to deactivate the receiver circuit without cutting the power or overcomplicating the circuit. So, instead of deactivating the detector circuits during transmission, the processor is programmed to ignore any detected signals during the transmission phase. Hence, the decoding stops temporarily. The ignored bits are marked in red on the diagram in Figure 7-5 and.

Lastly, at the begin of the photodetection phase, the decoding is also delayed for a period of t_f to be in sync with the opposite transmitter. The delay of transmission and detection with respect to the transition of the control signal allows the voltage of the “off” state to reach a stable level before data transmission starts.

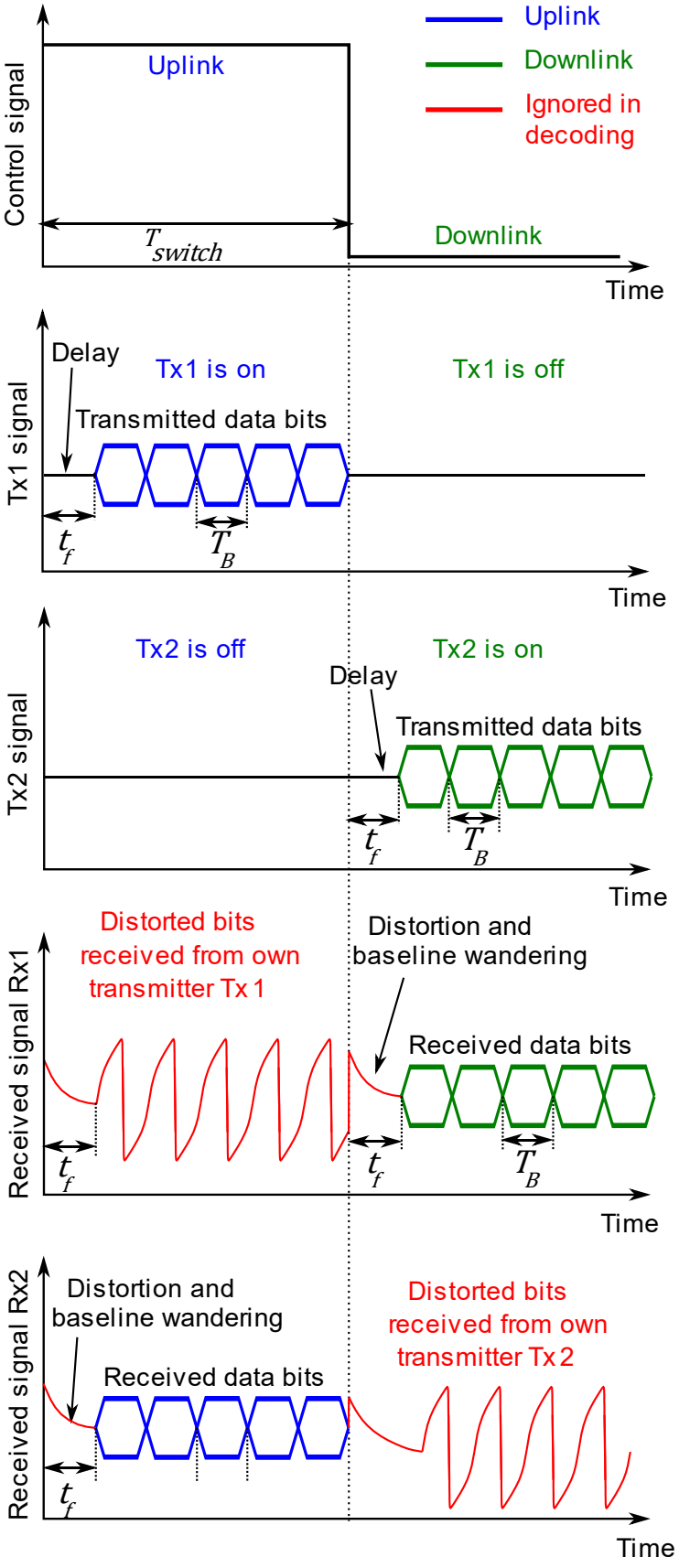

Figure 7-5: Timing diagram for uplink and downlink in response to the control signal

It has been established in chapter 4 that the worst-case scenario for the fall time of this switch is around 0.5 ms. While this fall time is expected to be shorter for smaller load resistances, the practical setup is designed to accommodate this worst-case scenario.

The flow chart in Figure 7-6 visualises the employed algorithm for successful transmission and detection in the bidirectional LED-to-LED system.

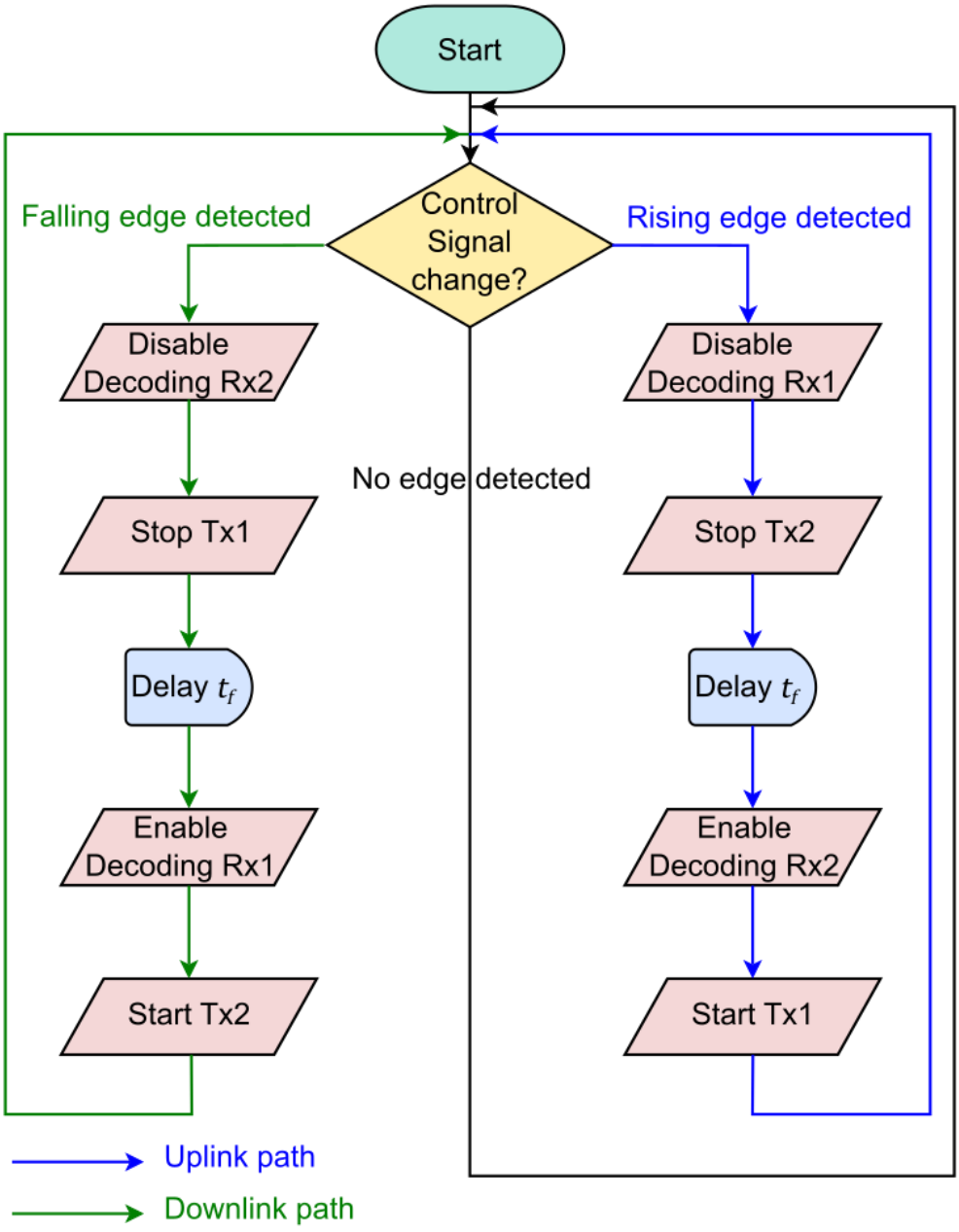

Figure 7-6: Flow chart visualizing the algorithm employed to achieve minimum bit error rate for the bidirectional system

The experiments characterising the switching IC in chapter 4 reveal that switching speeds up to 710 Hz are possible. The mathematical derivation of the overall system data rate in response to the switching frequency indicates that the data rate penalty increases with increasing switching frequency f_{switch}, as asserted in equation (4.25).

To keep that penalty at a minimum value while still avoiding flickering, switching frequencies of 100 to 300 Hz only were tested for the implementation of the bidirectional system. At these speeds, the on-off switching is fast enough to prevent flickering from being detected by a nearby human observer while still allowing for enough time to send large enough chunks of data at once. Substituting in equation (4.25) with the fall time t_f of 0.5 ms and switching frequencies f_{switch} 100 Hz and 300 Hz, respectively, the expected bandwidth penalty is between 5% (for $f_{\mathrm{switch}} = 100$ Hz) and 15% (for $f_{\mathrm{switch}} = 300$ Hz).

7.3. System Performance with Switching

7.3.1. One-directional Link (Constant Control Signal)

To characterise the effect of the switch on the system without the effect of the switching speed, the performance of the system is measured first with the control signal set to “high” and $f_{\text{switch}} = 0$. This permanently enables the uplink channel, making module 1 the transmitter and module 2 the receiver. The BER at varying distances and the maximum error-free transmission distance are evaluated as indicators for the system performance.

Figure 7-7 compares the BER of the LED-to-LED uplink at different data rates and distances in both cases: with and without the switch. It can be observed from the graph that the BER with switch is higher compared to the case without switch for all data rates and for transmission distances longer than 8 cm. The difference in BER between the two scenarios is larger for longer distances. This increase of

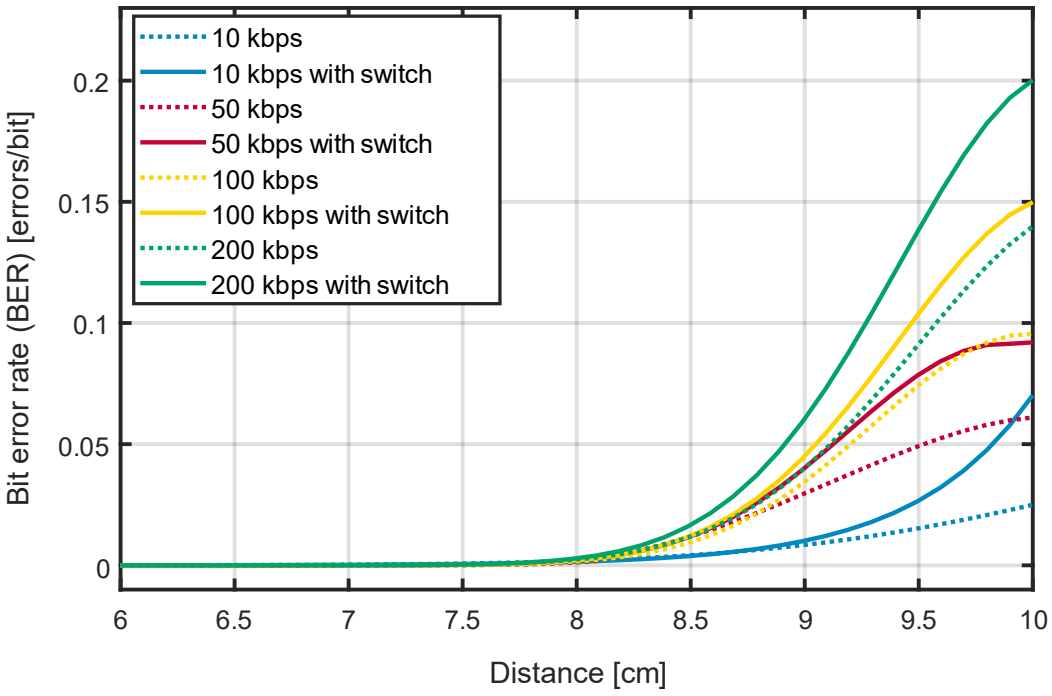

Figure 7-7: Comparison of the BER with and without the switch IC at varying distances and transmission data rates

the BER is due to the slight attenuation of the signal passing from the input to the output port of the switch. Although the attenuation is only 0.08 dB and plays no significant role in the short distances up to 7 cm, this attenuation is large enough to suppress the photocurrent produced by the LED at the receiving end below the threshold level for detection at longer distances. At 200 kbps, the BER is already 20% for a transmission distance of 10 cm.

Accordingly, the maximum error-free transmission distance is impacted by the switching circuit. Figure 7-8 depicts the penalty in the error-free transmission distance of the one-directional link due to the presence of the switch IC. From the figure, the error-free transmission distance is lower in the presence of the switch for all data rates. Instead of reaching 7 cm without the switch, only 5 cm error-free range could be achieved with the switch at 10 kbps. At higher speeds of 100 kbps and 200 kbps, the presence of the switch IC causes a 50% penalty in the link's transmission range.

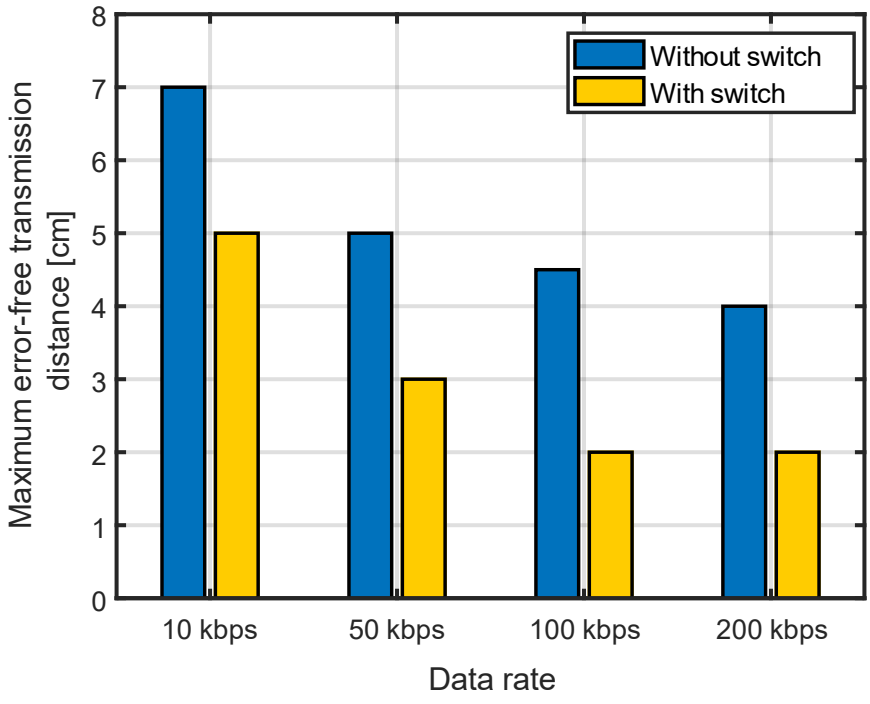

Figure 7-8: Comparison between maximum error-free transmission distances with and without switch at different data rates

7.3.2. Bidirectional System (Toggling Control Signal):

For achieving a bidirectional system, the control signal is toggled from high to low at a frequency f_{switch}, alternating thereby the uplink and downlink. This is expected to further reduce the data rate of the overall system according to equation (4.25).

Figure 7-9 shows an example of the captured signals on the oscilloscope at the 4 measuring points (focused on the falling edge of the control signal) when the modules are 1 cm apart. For the sake of demonstration, the transmitted signals from both circuits are square waves in this example. To calculate the BER however, a PRBS is transmitted. In the demonstrated example, the transmission data rate is 20 kbps and the switching frequency is 100 Hz. This translates to a

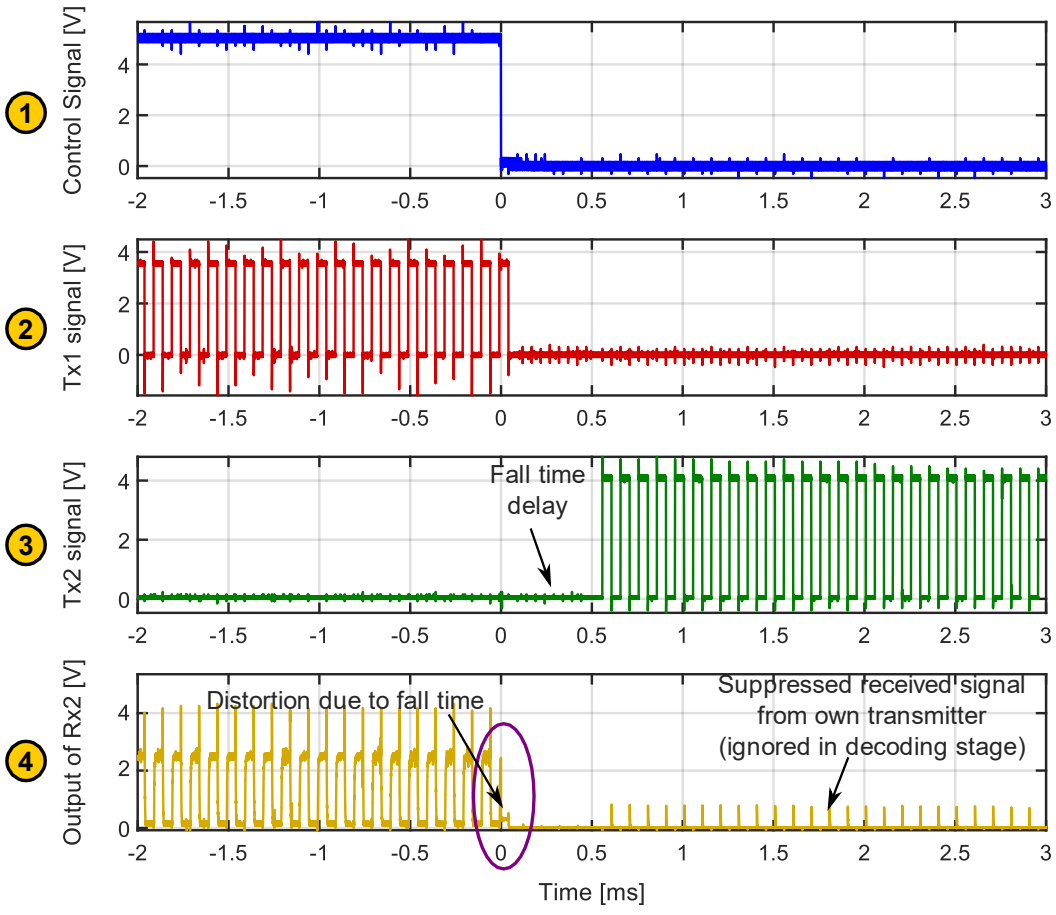

Figure 7-9: An example of the captured waveforms at the 4 measurement points

maximum overall data rate of the system equivalent to 19 kbps according to equation (4.25).

It can be seen from the figure that Rx2 can successfully detect the square wave signals from Tx1 during the uplink phase. Upon the transition of the control signal from high to low, Tx1 is stopped and Rx2 deactivated the decoding as indicated by the timing algorithm. This prevented the little distortion during the fall time from causing erroneous bits at the decoder.

Tx2 starts transmission after the delay time of the switch as indicated by the timing algorithm. During the transmission of Tx2, Rx2 is still detecting a suppressed version of its own transmitter. However, these bits are ignored in decoding due to the deactivation of the decoder.

To measure the effect of the switching frequency on the performance of the system, the maximum error-free overall data rate is determined at varying distances and switching frequencies. For this experiment, the overall data rate is calculated as the total number of complete bits transmitted by both LEDs (combined) per second.

The bar chart in Figure 7-10 compares the maximum error-free overall data rate at different distances and switching speeds. From the figure, the data rate decreases linearly with increasing switching speed at all distances. As expected, the back-to-back configuration (at 0 cm between transmitter and receiver) offers the highest error-free data rate due to the minimal power loss along the channel. In this scenario, the overall system data rate reaches 110 kbps at 100 Hz switching frequency, which drops to 95.8 kbps at $f_{\text{switch}} = 300$ Hz.

The maximum achievable error-free data rate drops quickly with increasing transmission distance, reaching only 1.9 kbps at 7 cm with 300 Hz switching frequency. Due to the rapid optical power loss along the channel (described by the inverse square law of light), only a fraction of the optical power reaches the receiving LED. The photocurrent produced by that LED is lowered further when it flows through the switching IC due to its internal attenuation factor of 0.08 dB. Hence, at the detection stage, the SNR is high, causing the rise of the BER.

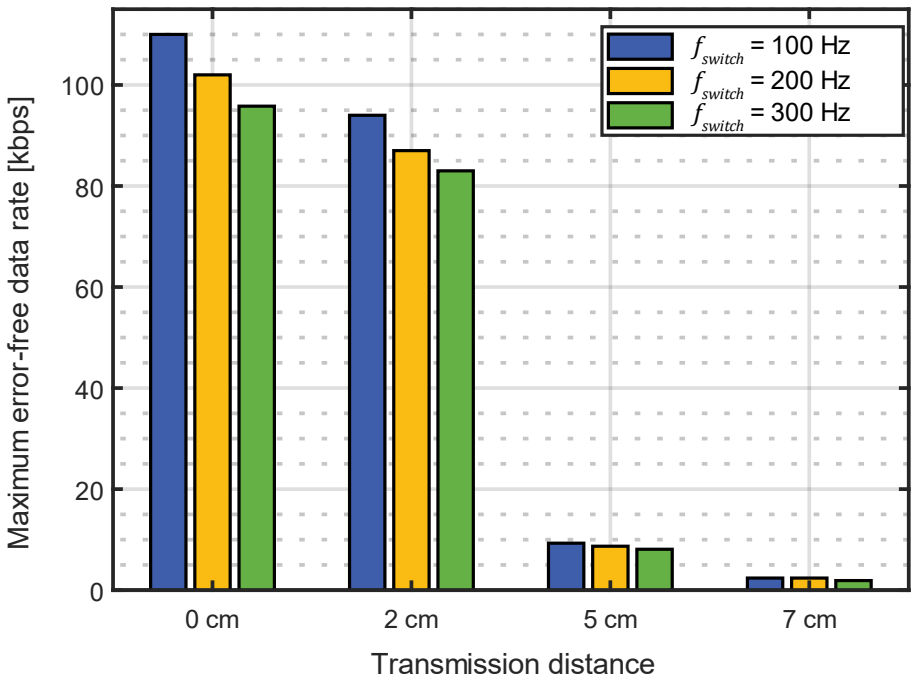

Figure 7-10: Maximum error-free overall data rate at different switching speeds and distances

7.4. Conclusion

In this chapter, the complete bidirectional LED-to-LED communication system is implemented and experimentally characterised. The system consists of two identical transceiver modules each connected to a simple microcontroller, as traditionally used in IoT devices. Each module is equipped with an analogue switch to operate the transmitter and receiver in a time-division multiplexing way. The control signal from an external oscillator is fed to both circuits to guarantee synchronisation and initiate the corresponding transmission and detection phases.

The switching IC has shortcomings in terms of attenuation and a long fall time, which were experimentally evaluated on the LED-to-LED link. Based on the experimental results, a timing algorithm is applied to delay the transmission and decoding with respect to the control signal. This avoids the distortion caused by the long fall time. In addition, transmission is stopped during the respective detection phase for each module to avoid interfering with the detected signal.

Thanks to the timing algorithm, an overall data rate up to 110 kbps can be achieved for the bidirectional system in a back-to-back configuration with a switching frequency of 100 Hz. At this frequency, the flickering of the LEDs on both sides of the channel is not noticeable and the LEDs appear as “always on” to an observer in the proximity. Due to the low sensitivity of the LED and the attenuation factor of the analogue switch, an error-free distance of only up to 7 cm can be achieved at an overall data rate of 1.9 kbps with 300 Hz switching frequency.

Chapter 8

Conclusion and Future Work

8.1. Conclusion

In today's world of interconnected devices and sensors, where communication is taken for granted and depended on for everyday tasks, it is of great importance to find out-of-box solutions to provide such connectivity at low-cost and with high potential for commercial deployment without overstressing the already crowded RF spectrum. Therefore, the main aim of this thesis is to design, implement and characterise a low-complexity bidirectional LED-to-LED communication system to act as a communication module between simple IoT devices along a short line-of-sight channel. The motivation behind this work is to create a viable alternative to the RF technologies for communication between simple IoT devices and to harness the full potential of the LED, which can act not only as a transmitter but also as photodetector, similar to the antenna in radio frequency.

In order to meet the objectives of this thesis, it was first imperative to review the fundamentals of VLC and its state-of-the-art as well as to discuss its potential in

serving IoT as a communication technology. Besides, it was important to review the concepts of interconnectivity between IoT devices and their communication requirements in order to design a system that truly serves those requests. Hence, those aspects were covered in chapter 2.

To fully harness the potential of the LED as a transmitter and as a photodetector, it was also important to review the fundamentals of light production and photodetection in chapter 3. Based on these theoretical findings about the construction of the LED and its functionality as transmitter and photodetector, practical experiments were designed to evaluate its performance in real life. It has been found that the RGB LED transmitter emits optical power that is proportional to the amount of forward current. Moreover, it was found that out of all three sub-LEDs, the green sub-LED provides the highest brightness and output optical power and is hence most suitable as transmitter. In chapter 6, the LED was also empirically characterised as photodetector. The responsivity, bandwidth, angle of reception, response to light power as well as its produced noise as photodetector were evaluated through different experiments. On the evidence of the results, the red sub-LED is most suitable as a photodetector. Not only does it show the highest responsivity to both the green and blue light, it also has the highest photodetection bandwidth. Interestingly, the results showed that the LED is capable of detecting light signals not only at zero or reverse bias, but also when slightly forward biased (dimly lit). The red sub-LED shows a maximum responsivity towards green light of 0.256 mA/W with bandwidth 4.9 MHz at maximum reversed biased and 0.202 mA/W with bandwidth 2.4 MHz at zero bias. It could be deduced from those results that the LED's performance as photodetector is not majorly affected by the applied biasing voltage and could therefore be employed in combination with a photovoltaic TIA detector circuit. The

angle of detection of the red LED is only 18°, much lower than the 90° that a regular PIN photodiode promises. This makes it a more directive receiver and opens the possibility of employing it in localisation applications.

After covering the fundamentals of VLC and LEDs, chapter 4 proposed the required circuitry to build a transmitter, receiver and switching module. Based on the requirements of IoT devices for low-complexity and low data rate communication, the system design in chapter 4 focused on keeping the circuit design simple and feasible for commercial deployment. Since the communication system performance is as weak as its weakest module, it was imperative to characterise each of the system components separately using both simulation and practical experiments, removing any obstacles or weak links in the process. Employing only low-complexity circuits and components, a current-mirror based LED driver was designed and characterised in chapter 4 that can deliver 19 mA of forward current to the LED while modulating it at a bandwidth up to 420 kHz. Similarly, a transimpedance amplifier circuit was designed with a transimpedance gain of 2 V/μA to accommodate the expected low sensitivity and responsivity of the LED photodetector while still providing a bandwidth of 334 kHz. The overall back-to-back communication link was characterised to guarantee the compatibility of these circuits. The evaluation revealed that the link can successfully operate with a bandwidth up to 129 kHz with a very low power consumption and overall price. Chapter 4 covered a major objective of this thesis, namely the design and characterisation of a feasible driver and receiver circuits for an LED.

Since a one-directional LED-to-LED communication link is interesting but not enough to harness the full capabilities of the LED, a switching mechanism between transmission and detection mode had to be proposed to provide a

bidirectional communication system. This agrees with the objectives of this thesis, mentioned in chapter 1. Hence, chapter 4 also proposes an analogue switching solution to change the LED mode from transmission to detection in response to a control signal. The main target of said switching solution is not only to provide a bidirectional channel if needed, but also to remove any flickering that might be noticed by a nearby human observer due to the LED being turned off during detection. Hence, the switching had to happen at frequencies starting from 100 Hz without majorly penalising the overall system bandwidth or bit error rate. Therefore, the proposed switching IC was experimentally characterised to reveal its performance and shortcomings. The experiments revealed that the analogue switch can provide very good, loss-free transmission of the signals in its “on” state. However, the system performance would suffer majorly in the “off” state and during the transition due to its mediocre attenuation factor and long fall time of up to 0.5 ms. These shortcomings can be mitigated through the smart design of a timing algorithm to avoid sending and receiving during the problematic periods. An expression for the penalty in the overall system data rate in terms of the switching frequency was derived.

The performance of a VLC system suffers majorly due to the noise generated by the photodetector as well as the interference due to other ambient light sources found in the proximity of the VLC channel. Therefore, it was one of the objectives of this thesis to cover the fundamentals of those noise sources and to identify the contemporary interfering ambient light sources. To carry out that objective, chapter 5 reviewed the contemporary ambient light sources such as thermal, gas discharge and semiconductor based light bulbs and empirically characterised their effects on the VLC channel. From the measurements of the variation, magnitude and spectrum of the output power of such sources, a mathematical

expression for the interference power was derived to model the effect of those sources separately at a 1 m distance. Hence, the noise and interference affecting the VLC channel due to modern ambient light sources could thereby be anticipated.

The designs of the transmitter and receiver circuits from chapter 4 as well as the results of the LED performance analysis in chapter 3 were used in designing and evaluating an LED-to-LED link, presented in chapter 6. For this one-directional link, the red sub-LED was employed as photodetector and the green sub-LED as light emitter, as per the results-based recommendation of chapter 3. The link was characterised in terms of the maximum error-free transmission distance, the BER and the SNR. The experimental results revealed that even while using OOK, the simplest modulation technique for VLC, successful data transmission is possible at data rates up to 200 kbps over a distance up to 4 cm with BER < 10^{-3} and the distance rises to 7 cm with transmission speed of 10 kbps.

Employing an optimised matched filter technique increases the system performance and matches its maximum error-free transmission distance to that of a regular PIN photodiode as detector. The results prove that using that technique, the BER could be decreased by up to 90% at a transmission speed of 200 kbps over a distance of 5 cm. Although the achieved data rates are considered low in comparison to other VLC systems, it is sufficient for most small IoT devices that require sending only status flags and small chunks of information between them. Moreover, an investigation of the RGB LED under the microscope proves that the system performance lags due to the much smaller active area of the RGB LED compared to a single-coloured red LED. This low sensitivity of the LED as photodetector is a blessing in disguise. It prevents the LED photodetector

from sensing any interference signal from the ambient light sources that interfere at a 90° angle from the ceiling.

In chapter 7, the implemented system was complemented by the proposed analogue switch and its performance was analysed and compared to the one-directional link. The presented results show that a bidirectional communication system is possible with switching frequencies up to 300 Hz, preventing thereby any flickering effect. Increasing the switching frequency comes at a price – the overall system bandwidth is thereby reduced by a factor equal to the product of the switching frequency and the fall time of the switch. This penalty in bandwidth is due to a timing control algorithm that aims to circumvent the shortcomings of the switch and to decrease the BER. The algorithm stops transmission and detection during the fall time after each switch transition as well as stops transmission of the LED during the detection period. This way, the interference due to the own transmitter during detection is prevented. The practical investigation of the overall system revealed that a time-division-multiplexed LED-to-LED system is feasible at error-free data rates up to 110 kbps in a back-to-back configuration. Increasing the distance to 7 cm, this error-free overall system data rate drops to below 10 kbps for all tested switching frequencies.

8.2. Future Work

From the findings of this thesis, some future works could be identified in relation to the proposed system. The system performance of the system could be enhanced in two different ways: either by extending its range to cover a longer transmission distance or by improving the achieved data rates. In most cases however, this enhancement comes at the cost of increasing the complexity. Listed below are the recommendations for possible future works in relation to this study.

8.2.1. Extending the system transmission range

Multiple Input, Multiple Output (MIMO)

Throughout this thesis, the system was evaluated using only a single sub-LED at each side of the communication channel. Due to the low optical power of a single sub-LED and the low sensitivity and responsivity of the LED as photodetector, the maximum error-free transmission distances were limited, as the experimental results in chapters 7 and 8 revealed. By extending the number of transmitting and receiving LEDs, this range could be extended thanks to the higher output power and the combined photocurrent. Aside from extending the range of the system, MIMO could also be employed to maximise the system throughput and extend the data rate if employed in a wavelength-division multiplexing manner. The experiments in chapter 6 revealed two interesting facts that can promote such a MIMO solution: Firstly, the LED is a wavelength-selective photodetector – which means that it detects some light colours better than others. Secondly, although the red sub-LED is most suitable for detection and green for transmission, another viable combination is blue-to-green. These findings open up the possibility of creating two parallel channels employing only one RGB LED at each end of the system. It must be taken into consideration, however, that the

complexity, number of components and cost of the system will increase using a MIMO technique.

Employing a specially designed LED

To keep the cost at a minimum, this thesis employed only off-the-shelf RGB LEDs that are not in any way optimised for light detection. It is a valid hypothesis, that a specially designed and doped LED that is optimised for both high brightness light emission as well as high responsivity in photodetection could improve the system performance and increase the limited transmission range on the cost of increasing the price. The design and manufacturing of such an LED requires deep know-how in material science and semiconductor manufacturing and was therefore out of the scope of this thesis.

8.2.2. Extending the system data rate

Employing more sophisticated modulation techniques

To maintain the low complexity of the design and hardware requirements, this thesis considered only employing NRZ OOK modulation. While this modulation technique is easy to implement and requires little processing power, it does not provide the highest data throughput or achieve the maximum system capacity. On the cost of increasing the system complexity and processing power, a more sophisticated modulation technique such as orthogonal frequency division multiplexing (OFDM) can be employed to increase the data rate and system throughput without changing the circuitry for transmission and detection. Similarly, a Manchester line encoding technique could be employed to reduce the BER, improve synchronisation and decrease the flicker, especially when a long stream of consecutive zeros or consecutive ones is transmitted at any point.

8.2.3. Further enhancements that maintain the low complexity

Effect of Interference in a line-of-sight configuration

The presented experimental results proved that the interfering ambient light sources had no effect on the LED-to-LED communication channel when they are perpendicular to the LED-to-LED channel and placed at distances larger than 1 m on the ceiling. This is mainly due to the low sensitivity of the LED photodetector as well as its small cone of acceptance of only 18°. Although it is a less common scenario in real life, the transmitter or receiver LED embedded on an IoT device could be directly facing the ceiling and therewith the interfering ambient light source. In this scenario, the interfering ambient light source would be emitting its light power parallel to the LED-to-LED channel and can therefore not be blocked by the small acceptance cone. It would therefore be interesting to know the impact of such interference on the LED-to-LED system performance and potentially involve optical and electronics filters to mitigate it.

Synchronisation between transmitter and detector in bidirectional system

For characterising the complete bidirectional system in this thesis, synchronisation between the modules on both ends of the channel was guaranteed using an external trigger source that feeds in a control signal to both modules. This however is not possible between wirelessly connected devices in real life. Instead, synchronisation between both modules should be achieved by actively listening to the channel before starting the transmission phase and sending only data when the channel is clear. Synchronisation must thereby be achieved via a software solution programmed on both IoT devices processors.

References

[1] M. Katz and D. O'Brien, "Exploiting novel concepts for visible light communications: from light-based IoT to living surfaces," *Optik (Stuttg).*, vol. 195, p. 163176, 2019.

[2] P. Kumar and U. C. Pati, "IoT based monitoring and control of appliances for smart home," in *2016 IEEE International Conference on Recent Trends in Electronics, Information & Communication Technology (RTEICT)*, 2016, pp. 1145–1150.

[3] P. Gokhale, O. Bhat, and S. Bhat, "Introduction to IOT," vol. 5, pp. 41–44, Jan. 2018.

[4] I. A. Alimi *et al.*, *Enabling VLC and WiFi Network Technologies and Architectures Toward 5G*. Chichester, UK: Chichester, UK: John Wiley & Sons, Ltd, 2019.

[5] N. Shahin, R. Ali, and Y. Kim, "Hybrid Slotted-CSMA/CA-TDMA for Efficient Massive Registration of IoT Devices," *IEEE Access*, vol. 6, pp. 18366–18382, 2018.

[6] T. Lv, Y. Ma, J. Zeng, and P. T. Mathiopoulos, "Millimeter-Wave NOMA Transmission in Cellular M2M Communications for Internet of Things," *IEEE Internet Things J.*, vol. 5, no. 3, pp. 1989–2000, 2018.

[7] L. Columbus, "Roundup Of Internet Of Things Forecasts And Market Estimates," *Forbes.com*, 2016. .

[8] L. Columbus, "The Top 20 IoT Startups To Watch In 2020," *Forbes.com*, 2020. [Online]. Available: https://www.forbes.com/sites/louiscolumbus/2020/05/25/the-top-20-iot-

startups-to-watch-in-2020/#7dd946fb7697. [Accessed: 26-Jun-2020].

[9] S. Singh and R. M. Sharma, “Handbook of Research on the IoT, Cloud Computing, and Wireless Network Optimization (2 Volumes).” IGI Global, Hershey, PA, USA, pp. 1–563, 2019.

[10] K. Nahrstedt, “Keynote: Internet of mobile things: Challenges and opportunities,” in *2014 23rd International Conference on Parallel Architecture and Compilation Techniques (PACT)*, 2014, p. 1.

[11] “Standard for Harmonization of Internet of Things (IoT) Devices and Systems, P1451-99,” 2016.

[12] A. Yavari, D. Georgakopoulos, P. R. Stoddart, and M. Shafiei, “Internet of Things-based Hydrocarbon Sensing for Real-time Environmental Monitoring,” in *2019 IEEE 5th World Forum on Internet of Things (WF-IoT)*, 2019, pp. 729–732.

[13] V. Pinrod *et al.*, “Zero Power, Tunable Resonant Microphone with Nanowatt Classifier for Wake-Up Sensing,” in *2018 IEEE SENSORS*, 2018, pp. 1–4.

[14] K. Yelmarthi, A. Abdelgawad, and A. Khattab, “An architectural framework for low-power IoT applications,” in *2016 28th International Conference on Microelectronics (ICM)*, 2016, pp. 373–376.

[15] M. Ali *et al.*, “Devices to Devices (Ds2Ds) Communication: Towards Energy Efficient IoT,” in *2018 IEEE Global Communications Conference (GLOBECOM)*, 2018, pp. 1–6.

[16] S. Wu, H. Wang, and C.-H. Youn, “Visible light communications for 5G wireless networking systems: from fixed to mobile communications,” *Ieee Netw.*, vol. 28, no. 6, pp. 41–45, 2014.

[17] M. Uysal, C. Capsoni, Z. Ghassemlooy, A. Boucouvalas, and E. Udvary, *Optical Wireless Communications: An Emerging Technology*. Springer International Publishing, 2016.

[18] H. K. Al-Musawi *et al.*, “Adaptation of Mode Filtering Technique in 4G-LTE Hybrid RoMMF-FSO for Last-Mile Access Network,” *J. Light. Technol.*, vol. 35, no. 17, pp. 3758–3764, 2017.

[19] J. Rodriguez, “The Wireless Spectrum Crunch,” in *Fundamentals of 5G Mobile Networks*, Wiley, 2014, pp. 165–189.

[20] P. Kuppusamy, S. Muthuraj, and S. Gopinath, “Survey and challenges of Li-Fi with comparison of Wi-Fi,” in *2016 International Conference on Wireless Communications, Signal Processing and Networking (WiSPNET)*, 2016, pp. 896–899.

[21] S. Dimitrov and H. Haas, *Principles of LED Light Communications: Towards Networked Li-Fi*. Cambridge University Press, 2015.

[22] C. Johansen, J. D. Boice Jr., J. K. McLaughlin, and J. H. Olsen, “Cellular Telephones and Cancer—a Nationwide Cohort Study in Denmark,” *JNCI J. Natl. Cancer Inst.*, vol. 93, no. 3, pp. 203–207, Feb. 2001.

[23] S. U. Rehman, S. Ullah, P. H. J. Chong, S. Yongchareon, and D. Komosny, “Visible Light Communication: A System Perspective-Overview and Challenges,” *Sensors (Basel).*, vol. 19, no. 5, p. 1153, Mar. 2019.

[24] “Forget LTE and Wi-Fi; ‘Li-Fi’ Will Be 100 Times Faster | Bidness | Technology | By Martin Blanc.” [Online]. Available: http://www.bidnessetc.com/58322-forget-lte-and-wifi-lifi-will-be-100-times-faster/. [Accessed: 13-Mar-2016].

[25] H. Haas, “LiFi: Conceptions, misconceptions and opportunities,” in *Photonics Conference (IPC), 2016 IEEE*, 2016, pp. 680–681.

[26] K. Kadam and M. R. Dhage, “Visible Light Communication for IoT,” in *2016 2nd International Conference on Applied and Theoretical Computing and Communication Technology (iCATccT)*, 2016, pp. 275–278.

[27] M. Galal, W. P. Ng, A. A. El Aziz, and R. Binns, “Characterisation and Interference Model of Contemporary Artificial Light Sources Noise on a VLC channel,” in *2018 11th International Symposium on Communication Systems, Networks & Digital Signal Processing (CSNDSP)*, 2018, pp. 1–6.

[28] S. Kasap and P. Capper, *Springer Handbook of Electronic and Photonic Materials*, 1st ed. 20. New York, NY : Springer US : Imprint: Springer, 2007.

[29] P. Dietz, W. Yerazunis, and D. Leigh, “Very low-cost sensing and communication using bidirectional LEDs,” in *UbiComp 2003: Ubiquitous Computing*, 2003, pp. 175–191.

[30] S. Schmid, G. Corbellini, S. Mangold, and T. R. Gross, “LED-to-LED Visible Light Communication Networks,” *MobiHoc*, pp. 1–9, 2013.

[31] G. Stepniak, M. Kowalczyk, L. Maksymiuk, and J. Siuzdak, “Transmission Beyond 100 Mbit/s Using LED Both as a Transmitter and Receiver,” *IEEE Photonics Technol. Lett.*, vol. 27, no. 19, pp. 2067–2070, 2015.

[32] H. Chun, S. Rajbhandari, G. Faulkner, D. Tsonev, H. Haas, and D. O’Brien, “Demonstration of a Bi-directional visible light communication with an overall sum-rate of 110 Mb/s using LEDs as emitter and detector,” in *2014 IEEE Photonics Conference*, 2014, pp. 132–133.

[33] M. Kowalczyk and J. Siuzdak, “Photo-reception properties of common

LEDs," *Opto-Electronics Rev.*, vol. 25, no. 3, pp. 222–228, 2017.

[34] M. Galal, W. P. Ng, R. Binns, and A. Abd El Aziz, "Characterization of RGB LEDs as Emitter and Photodetector for LED-to-LED Communication," in *12th IEEE/IET International Symposium on Communication Systems, Networks and Digital Signal Processing- CSNDSP*, 2020.

[35] M. Galal, W. P. Ng, R. Binns, and A. Abd El Aziz, "Experimental Characterization of RGB LED Transceiver in Low-complexity LED-to-LED Link," *Sensors (Basel).*, no. 20, p. 5754, 2020.

[36] Z. Wang, Q. Wang, W. Huang, and Z. Xu, *Visible light communications: modulation and signal processing*. John Wiley & Sons, 2017.

[37] W. O. Popoola, "Impact of VLC on Light Emission Quality of White LEDs," *J. Light. Technol.*, vol. 34, no. 10, pp. 2526–2532, 2016.

[38] Z. Ghassemlooy, L. N. Alves, S. Zvanovec, and M.-A. Khalighi, *Visible light communications: theory and applications*. Taylor & Francis Group, 2017.

[39] J. M. Dilhac, "The telegraph of claude chappe-an optical telecommunication network for the xviiith century," *Inst. Natl. des Sci. Appliquées Toulouse*, 2001.

[40] A. G. Bell, "Selenium and the Photophone1," *Nature*, vol. 22, no. 569, pp. 500–503, 1880.

[41] F. R. Gfeller and U. Bapst, "Wireless in-house data communication via diffuse infrared radiation," *Proc. IEEE*, vol. 67, no. 11, pp. 1474–1486, 1979.

[42] Y. Tanaka, T. Komine, S. Haruyama, and M. Nakagawa, "Indoor visible light data transmission system utilizing white LED lights," *IEICE Trans.*

Commun., vol. 86, no. 8, pp. 2440–2454, 2003.

[43] Z. Wang, Q. Wang, W. Huang, and Z. Xu, “Introduction to Visible Light Communications,” in *Visible Light Communications: Modulation and Signal Processing*, IEEE, 2018, pp. 1–16.

[44] H. Le Minh *et al.*, “100-Mb/s NRZ Visible Light Communications Using a Postequalized White LED,” *IEEE Photonics Technol. Lett.*, vol. 21, no. 15, pp. 1063–1065, 2009.

[45] J. Vucic, C. Kottke, S. Nerreter, A. Buttner, K.-. Langer, and J. W. Walewski, “White Light Wireless Transmission at 200${+}$ Mb/s Net Data Rate by Use of Discrete-Multitone Modulation,” *IEEE Photonics Technol. Lett.*, vol. 21, no. 20, pp. 1511–1513, 2009.

[46] A. M. Khalid, G. Cossu, R. Corsini, P. Choudhury, and E. Ciaramella, “1-Gb/s Transmission Over a Phosphorescent White LED by Using Rate-Adaptive Discrete Multitone Modulation,” *IEEE Photonics J.*, vol. 4, no. 5, pp. 1465–1473, 2012.

[47] D. O’Brien, “High speed optical wireless demonstrators in the OMEGA project: Summary and conclusions,” in *Proceedings of the 2013 18th European Conference on Network and Optical Communications & 2013 8th Conference on Optical Cabling and Infrastructure (NOC-OC&I)*, 2013, pp. 159–162.

[48] “IEEE Standard for Local and metropolitan area networks--Part 15.7: Short-Range Optical Wireless Communications,” *IEEE Std 802.15.7-2018 (Revision of IEEE Std 802.15.7-2011)*. pp. 1–407, 2019.

[49] G. Cossu, A. Wajahat, R. Corsini, and E. Ciaramella, “5.6 Gbit/s downlink

and 1.5 Gbit/s uplink optical wireless transmission at indoor distances (≥ 1.5 m),” in *Optical Communication (ECOC), 2014 European Conference on*, 2014, pp. 1–3.

[50] IEEE 802.11, “Status of IEEE 802.11 Light Communication TG,” 2020. [Online]. Available: http://www.ieee802.org/11/Reports/tgbb_update.htm. [Accessed: 15-Jul-2020].

[51] N. Serafimovsk, “PureLiFi and Lucibel Introduce First Fully Industrialized LiFi Luminaire–PureLiFi™,” *PureLiFi, Novemb.*, vol. 25, 2015.

[52] A. Galisteo, D. Juara, Q. Wang, and D. Giustiniano, “OpenVLC1.2: Achieving higher throughput in low-end visible light communication networks,” in *2018 14th Annual Conference on Wireless On-demand Network Systems and Services (WONS)*, 2018, pp. 117–120.

[53] L. U. Khan, “Visible light communication: Applications, architecture, standardization and research challenges,” *Digit. Commun. Networks*, vol. 3, no. 2, pp. 78–88, 2017.

[54] D. C. O’Brien, L. Zeng, H. Le-Minh, G. Faulkner, J. W. Walewski, and S. Randel, “Visible light communications: Challenges and possibilities,” in *2008 IEEE 19th International Symposium on Personal, Indoor and Mobile Radio Communications*, 2008, pp. 1–5.

[55] L. E. M. Matheus, A. B. Vieira, L. F. M. Vieira, M. A. M. Vieira, and O. Gnawali, “Visible Light Communication: Concepts, Applications and Challenges,” *IEEE Commun. Surv. Tutorials*, vol. 21, no. 4, pp. 3204–3237, 2019.

[56] S. Rajbhandari *et al.*, “High-Speed Integrated Visible Light Communication

System: Device Constraints and Design Considerations," *IEEE J. Sel. Areas Commun.*, vol. 33, no. 9, pp. 1750–1757, 2015.

[57] A. Bluschke, P. Rietzsch, and H. Willebrand, "High bitrate optical wireless communication for indoor & outdoor applications," in *Broadband Coverage in Germany; 10. ITG-Symposium*, 2016, pp. 1–6.

[58] M. Z. Chowdhury, M. T. Hossan, A. Islam, and Y. M. Jang, "A comparative survey of optical wireless technologies: Architectures and applications," *IEEE Access*, vol. 6, pp. 9819–9840, 2018.

[59] T. Tang, T. Shang, Q. Li, and P. H. Qian, "Shadowing Effects on Indoor Visible Light Communication Channel Modeling," in *2020 Information Communication Technologies Conference (ICTC)*, 2020, pp. 7–11.

[60] R. D. Roberts, "IEEE 802 . 15 . 7 Visible Light Communication : Modulation Schemes and Dimming Support," *IEEE Commun. Mag.*, no. March, pp. 72–82, 2012.

[61] K. Lee and H. Park, "Modulations for Visible Light Communications With Dimming Control," *IEEE Photonics Technol. Lett.*, vol. 23, no. 16, pp. 1136–1138, 2011.

[62] E. Cho *et al.*, "NRZ-OOK signaling with LED dimming for visible light communication link," in *2011 16th European Conference on Networks and Optical Communications*, 2011, pp. 32–35.

[63] A. C. Boucouvalas, "Ambient light noise and its effect on receiver design for indoor wireless optical links," in *Proceedings of ICC/SUPERCOMM '96 - International Conference on Communications*, vol. 3, pp. 1472–1476.

[64] M. Galal, W. P. Ng, A. A. E. Aziz, and R. Binns, "Characterisation and

Interference Model of Contemporary Artificial Light Sources Noise on a VLC channel," in *2018 11th International Symposium on Communication Systems, Networks and Digital Signal Processing, CSNDSP 2018*, 2018.

[65] S. Shao *et al.*, "Design and analysis of a visible-light-communication enhanced WiFi system," *IEEE/OSA J. Opt. Commun. Netw.*, vol. 7, no. 10, pp. 960–973, 2015.

[66] A. Burton, E. Bentley, H. Le Minh, Z. Ghassemlooy, N. Aslam, and S. Liaw, "Experimental demonstration of a 10BASE-T Ethernet visible light communications system using white phosphor light-emitting diodes," *IET Circuits, Devices Syst.*, vol. 8, no. 4, pp. 322–330, 2014.

[67] Z. Ghassemlooy, S. Rajbhandari, and W. Popoola, *Optical wireless communications: system and channel modelling with MATLAB*. Boca Raton, Fla: CRC Press, 2013.

[68] R. F. Wiser, "Photodiode operable in photoconductive mode and photovoltaic mode." Google Patents, 14-Jun-2016.

[69] K. Siddiqi, A. D. Raza, and S. S. Muhammad, "Visible light communication for V2V intelligent transport system," in *2016 International Conference on Broadband Communications for Next Generation Networks and Multimedia Applications (CoBCom)*, 2016, pp. 1–4.

[70] Q. Xiang, Y. Li, W. Huang, W. Ye, and J. Shen, "Deep Learning assisted Visible Light Communication based Intelligent Transport System," in *2019 18th International Conference on Optical Communications and Networks (ICOCN)*, 2019, pp. 1–3.

[71] N. WANG, Y. QIAO, W. WANG, S. TANG, and J. SHEN, "Visible Light

Communication based Intelligent Traffic Light System: Designing and Implementation," in *2018 Asia Communications and Photonics Conference (ACP)*, 2018, pp. 1–3.

[72] Z. Minglun, Y. Xueguang, and H. Yongqing, "A 10.7 km visible light communications experiment," in *2016 Eighth International Conference on Ubiquitous and Future Networks (ICUFN)*, 2016, pp. 231–234.

[73] E. W. Lam and T. D. C. Little, "Visible Light Positioning for Location-Based Services in Industry 4.0," in *2019 16th International Symposium on Wireless Communication Systems (ISWCS)*, 2019, pp. 345–350.

[74] W. Guan *et al.*, "A novel three-dimensional indoor positioning algorithm design based on visible light communication," *Opt. Commun.*, vol. 392, pp. 282–293, 2017.

[75] A. Chizari, M. V. Jamali, S. Abdollahramezani, J. A. Salehi, and A. Dargahi, "Visible light for communication, indoor positioning, and dimmable illumination: A system design based on overlapping pulse position modulation," *Opt. J. Light Electron Opt.*, vol. 151, pp. 110–122, 2017.

[76] Robert Bosch GmbH, "Bosch Internet of Things," 2020. [Online]. Available: www.bosch.com/internet-of-things/. [Accessed: 17-Jul-2020].

[77] A. Mdhaffar, T. Chaari, K. Larbi, M. Jmaiel, and B. Freisleben, "IoT-based health monitoring via LoRaWAN," in *IEEE EUROCON 2017-17th International Conference on Smart Technologies*, 2017, pp. 519–524.

[78] T. M. Bojan, U. R. Kumar, and V. M. Bojan, "An internet of things based intelligent transportation system," in *2014 IEEE International Conference on Vehicular Electronics and Safety*, 2014, pp. 174–179.

[79] Reuters, “Amazon launches business selling automated checkout to retailers,” 2020. [Online]. Available: https://www.reuters.com/article/us-amazon-com-store-technology/amazon-launches-business-selling-automated-checkout-to-retailers-idUSKBN20W0OD. [Accessed: 17-Jul-2020].

[80] S. Rallapalli, A. Ganesan, K. Chintalapudi, V. N. Padmanabhan, and L. Qiu, “Enabling Physical Analytics in Retail Stores Using Smart Glasses,” in *Proceedings of the 20th Annual International Conference on Mobile Computing and Networking*, 2014, pp. 115–126.

[81] M. Rouse, “Smart Home,” 2019. [Online]. Available: https://whatis.techtarget.com/de/definition/Smart-Home. [Accessed: 24-Jul-2020].

[82] J. Bradley, J. Barbier, and D. Handler, “Embracing the Internet of everything to capture your share of $14.4 trillion,” *White Pap. Cisco*, vol. 318, 2013.

[83] F. Vannieuwenborg, S. Verbrugge, and D. Colle, “Choosing IoT-connectivity? A guiding methodology based on functional characteristics and economic considerations,” *Trans. Emerg. Telecommun. Technol.*, vol. 29, no. 5, p. e3308, 2018.

[84] R. A. Kjellby, T. E. Johnsrud, S. E. Loetveit, L. R. Cenkeramaddi, M. Hamid, and B. Beferull-Lozano, “Self-powered iot device for indoor applications,” in *2018 31st International Conference on VLSI Design and 2018 17th International Conference on Embedded Systems (VLSID)*, 2018, pp. 455–456.

[85] K. Warmerdam, A. Pandharipande, and D. Caicedo, “Connectivity in IoT

indoor lighting systems with visible light communications," in *2015 IEEE Online Conference on Green Communications (OnlineGreenComm)*, 2015, pp. 47–52.

[86] M. Haus, A. Y. Ding, and J. Ott, "LocalVLC: Augmenting Smart IoT Services with Practical Visible Light Communication," in *2019 IEEE 20th International Symposium on "A World of Wireless, Mobile and Multimedia Networks" (WoWMoM)*, 2019, pp. 1–9.

[87] M. Novak, A. Dobesch, and O. Wilfert, "On human to database interface based on visible light communication," in *2018 Global LIFI Congress (GLC)*, 2018, pp. 1–4.

[88] C. Kim, S. Choi, and S. Koh, "IDMP-VLC: IoT device management protocol in visible light communication networks," in *2017 19th International Conference on Advanced Communication Technology (ICACT)*, 2017, pp. 578–583.

[89] D. Giustiniano, N. O. Tippenhauer, and S. Mangold, "Low-complexity Visible Light Networking with LED-to-LED communication," in *2012 IFIP Wireless Days*, 2012, pp. 1–8.

[90] G. Corbellini, K. Aksit, S. Schmid, S. Mangold, and T. R. Gross, "Connecting networks of toys and smartphones with visible light communication," *IEEE Commun. Mag.*, vol. 52, no. 7, pp. 72–78, 2014.

[91] S. Schmid, G. Corbellini, S. Mangold, and T. R. Gross, "Continuous synchronization for LED-to-LED visible light communication networks," in *2014 3rd International Workshop in Optical Wireless Communications (IWOW)*, 2014, pp. 45–49.

[92] S. O. Kasap and R. K. Sinha, *Optoelectronics and Photonics: Principles and Practices*. Pearson, 2012.

[93] N. O. Tippenhauer, D. Giustiniano, and S. Mangold, “Toys communicating with LEDs: Enabling toy cars interaction,” in *2012 IEEE Consumer Communications and Networking Conference (CCNC)*, 2012, pp. 48–49.

[94] R. Stojanovic, “An optical sensing approach based on light emitting diodes,” *J. Phys. Conf. Ser.*, vol. 76, no. 1, p. 12054, 2007.

[95] S. Schmid, D. Schwyn, K. Aks, G. Corbellini, T. R. Gross, and S. Mangold, “From Sound to Sight : Using Audio Processing to enable Visible Light Communication,” *5th IEEE Work. Opt. Wirel. Commun.*, no. Section III, 2014.

[96] E. Miyazaki, S. Itami, and T. Araki, “Using a light-emitting diode as a high-speed, wavelength selective photodetector,” *Rev. Sci. Instrum.*, vol. 69, no. 11, pp. 3751–3754, 1998.

[97] M. Kowalczyk and J. Siuzdak, “Influence of reverse bias on the LEDs properties used as photo-detectors in VLC systems,” in *Proc.SPIE*, 2015, vol. 9662.

[98] M. Kowalczyk and J. Siuzdak, “VLC link with LEDs used as both transmitters and photo-detectors,” *Ubiquitous and Future Networks (ICUFN), 2015 Seventh International Conference on*. pp. 893–897, 2015.

[99] A. G. Zabalo, “Visible Light Communication Networks for IoT and its Applications,” Universidad Carlos III de Madrid, 2020.

[100] S. Li, B. Huang, and Z. Xu, “Experimental MIMO VLC systems using tricolor LED transmitters and receivers,” in *2017 IEEE Globecom Workshops (GC*

Wkshps), 2017, pp. 1–6.

[101] THOR Labs, “Rise Time , Frequency Response , and 3 dB Bandwidth.” pp. 1–26, 2019.

[102] F. Vera, R. Rivera, and M. Ortíz, “A simple experiment to measure the inverse square law of light in daylight conditions,” *Eur. J. Phys.*, vol. 35, no. 1, p. 15015, 2013.

[103] J. E. FARRELL, “An analytical method for predicting perceived flicker,” *Behav. Inf. Technol.*, vol. 5, no. 4, pp. 349–358, Oct. 1986.

[104] P. A. Haigh and Z. Ghassemlooy, “Visible Light Communications Using Organic Light Emitting Diodes,” no. August, pp. 148–154, 2013.

[105] A. Burton, *Smart white LED based lighting and communications*. .

[106] C. Mittermayer and A. Steininger, “On the determination of dynamic errors for rise time measurement with an oscilloscope,” *IEEE Trans. Instrum. Meas.*, vol. 48, no. 6, pp. 1103–1107, 1999.

[107] S. Fuada, A. P. Putra, Y. Aska, and T. Adiono, “Trans-impedance amplifier (HA) design for Visible Light Communication (VLC) using commercially available OP-AMP,” in *2016 3rd International Conference on Information Technology, Computer, and Electrical Engineering (ICITACEE)*, 2016, pp. 31–36.

[108] H. W. Bode, “Network analysis and feedback amplifier design,” 1945.

[109] M. Pachchigar, “Design considerations for a transimpedance amplifier,” *Natl. Semicond. Appl. Note*, vol. 1803, 2008.

[110] H. Han, M. Zhang, P. Luo, W. Xu, D. Han, and M. Wu, “Real-time bi-

directional visible light communication system," in *2016 15th International Conference on Optical Communications and Networks (ICOCN)*, 2016, pp. 1–3.

[111] L. T. Dung, S. Jo, and B. An, "Demonstration of Low-Complexity LED-to-LED Two-Way Visible Light Communication System," in *2016 International Symposium on Computer, Consumer and Control (IS3C)*, 2016, pp. 216–219.

[112] Z. Ghassemlooy, W. Popoola, and S. Rajbhandari, *Optical wireless communications: system and channel modelling with Matlab®*. CRC press, 2012.

[113] B. Hussain, X. Li, F. Che, C. Patrick Yue, and L. Wu, "Visible Light Communication System Design and Link Budget Analysis," *J. Light. Technol.*, vol. 33, no. 24, pp. 5201–5209, 2015.

[114] A. J. C. Moreira, R. T. Valadas, and A. M. de Oliveira Duarte, "Optical interference produced by artificial light," *Wirel. Networks*, vol. 3, no. 2, pp. 131–140, 1997.

[115] A. J. C. Moreira, R. T. Valadas, and A. M. de Oliveira Duarte, "Characterisation and modelling of artificial light interference in optical wireless communication systems," in *Proceedings of 6th International Symposium on Personal, Indoor and Mobile Radio Communications*, vol. 1, pp. 326–331.

[116] Zumtobel Lighting GmbH, *The Lighting Handbook*, 5th ed. Dornbirn - Austria: Zumtobel, 2017.

[117] S. Lesecq and A. Barraud, "A PRBS with exactly zero correlation and its

application," in *2008 16th Mediterranean Conference on Control and Automation*, 2008, pp. 724–728.

[118] V. Semiconductors, "Vishay Semiconductors Silicon PIN Photodiode , RoHS Compliant TEST CONDITION SYMBOL Silicon PIN Photodiode , RoHS Compliant SYMBOL," pp. 386–390, 2002.

[119] W. Freude *et al.*, "Quality metrics for optical signals: Eye diagram, Q-factor, OSNR, EVM and BER," in *2012 14th International Conference on Transparent Optical Networks (ICTON)*, 2012, pp. 1–4.

[120] W. Grupp, "Optical performance monitoring in optical transport networks." pp. 385–421, 2010.

[121] D. A. Fishman and B. S. Jackson, "Transmitter and Receiver Design for Amplified Lightwave Systems," in *Optical Fiber Telecommunications IIIB*, 1997, pp. 69–114.

[122] S. S. Haykin, *Communication systems*, 5th ed., I. Hoboken, N.J. : Chichester: Hoboken, N.J. : Wiley , 2010.

[123] G. Keiser, *Optical fiber communications*. McGraw-Hill Science/Engineering/Math, 2000.